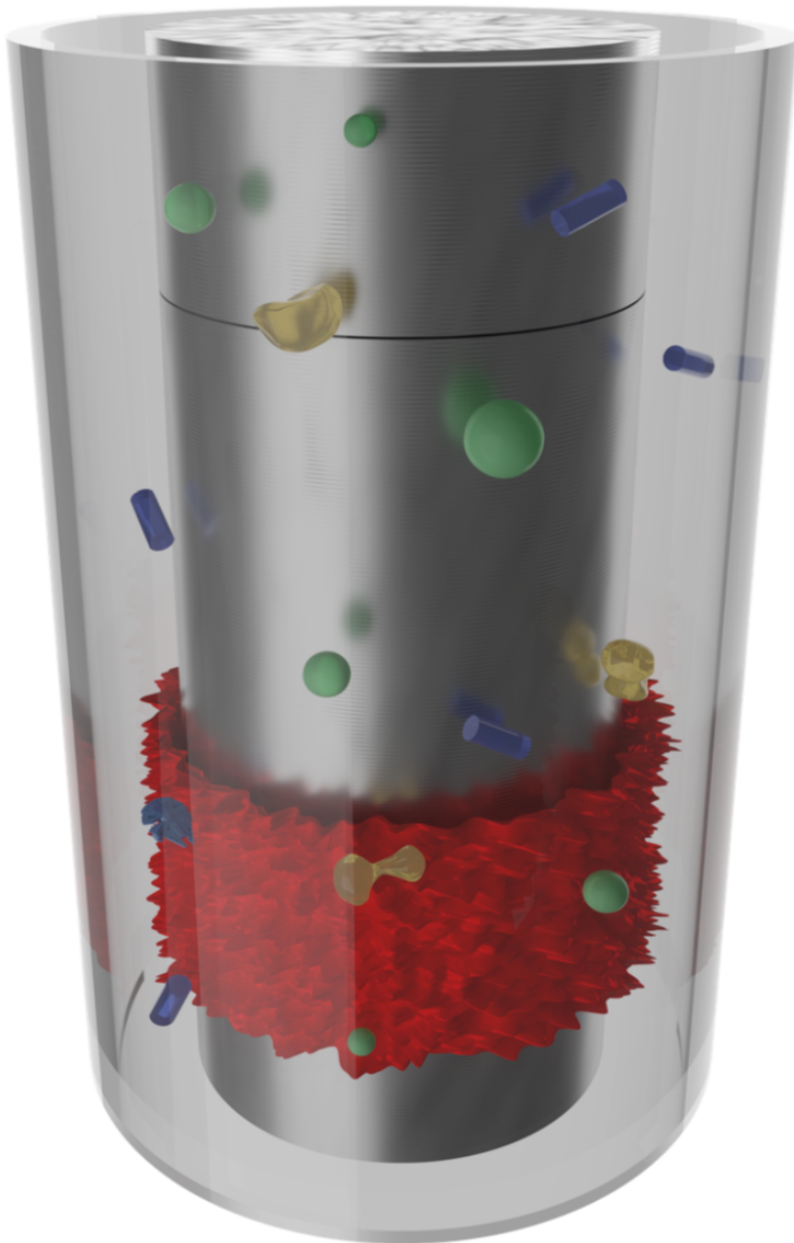


# Multiphase wall-bounded turbulence



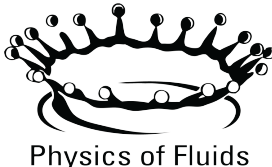
Dennis Bakhuis

# Multiphase wall-bounded turbulence

Dennis Bakhuis

**Graduation committee:**

Prof. dr. J. L. Herek (chairman)	UT, Enschede
Prof. dr. C. Sun (supervisor)	Tsinghua, Beijing; UT, Enschede
Prof. dr. ret. nat. D. Lohse (supervisor)	UT, Enschede
Asst. prof. dr. S. G. Huisman (co-supervisor)	UT, Enschede
Prof. dr. ir. T. J. C. van Terwisga	TU, Delft
Prof. dr. ir. A. W. Vreman	TU/e, Eindhoven
Prof. dr. J. G. M. Kuerten	TU/e, Eindhoven; UT, Enschede
Prof. dr. W. L. Vos	UT, Enschede



**UNIVERSITY  
OF TWENTE.**

The work in this thesis was carried out at the Physics of Fluids group of the Faculty of Science and Technology of the University of Twente. This thesis was financially supported by the Netherlands Organisation for Scientific Research (NWO) under VIDI grant No. 13477.

Dutch title:

*Meerfasen wandbegrenste turbulentie*

Publisher:

Dennis Bakhuis, Physics of Fluids, University of Twente,  
P.O. Box 217, 7500 AE Enschede, The Netherlands

Cover design:

A render of the Taylor-Couette setup with the inclusions and roughness used in this thesis, created with the Blender 3D creation suite. The roughness is based on the confocal scan. The height of the roughness and size of the inclusions are exaggerated for visualization.

Copyright © 2019. All rights reserved.

No part of this work may be reproduced or transmitted for commercial purposes, in any form or by any means, electronic or mechanical, including photocopying and recording, or by any information storage or retrieval system, except as expressly permitted by the publisher.

ISBN: 978-90-365-4679-9

DOI: 10.3990/1.9789036546799

# MULTIPHASE WALL-BOUNDED TURBULENCE

## DISSERTATION

to obtain  
the degree of doctor at the University of Twente,  
on the authority of the rector magnificus,  
Prof. dr. T. T. M. Palstra,  
on account of the decision of the graduation committee,  
to be publicly defended  
on Thursday the 31st of January 2019 at 16:45

by

Dennis Bakhuis  
Born on the 25th of July 1982  
in Celle, Germany

This dissertation has been approved by the supervisors:

Prof. dr. Chao. Sun  
Prof. dr. ret. nat. Detlef Lohse

and the co-supervisor:

Asst. prof. dr. Sander G. Huisman

# Contents

<b>Introduction</b>	<b>1</b>
Turbulent flows . . . . .	1
Multiphase flows . . . . .	3
Drag reduction . . . . .	4
Taylor-Couette flow and Rayleigh-Bénard convection . . . . .	5
Outline of the thesis . . . . .	7
<b>1 Finite-sized rigid spheres in turbulent Taylor-Couette flow</b>	<b>9</b>
1.1 Introduction . . . . .	10
1.2 Experimental setup . . . . .	13
1.3 Results . . . . .	16
1.4 Conclusions and outlook . . . . .	26
<b>2 Statistics of rigid fibers in strongly sheared turbulence</b>	<b>29</b>
2.1 Introduction . . . . .	30
2.2 Experiments and results . . . . .	32
2.3 Summary . . . . .	38
<b>3 Dramatic change in drag by catastrophic phase inversion</b>	<b>39</b>
3.1 Introduction . . . . .	40
3.2 Experiments and results . . . . .	41
3.3 Summary . . . . .	49
<b>4 Mixed boundary conditions in Rayleigh-Bénard convection</b>	<b>51</b>
4.1 Introduction . . . . .	52
4.2 Numerical method . . . . .	55
4.3 Results . . . . .	59
4.4 Summary and conclusions . . . . .	72

<b>5 Controlling the secondary flows in turbulent Taylor–Couette flow</b>	<b>75</b>
5.1 Introduction . . . . .	76
5.2 Methods . . . . .	80
5.3 Results . . . . .	87
5.4 Conclusions and outlook . . . . .	97
<b>Conclusions</b>	<b>99</b>
<b>Bibliography</b>	<b>103</b>
<b>Summary</b>	<b>123</b>
<b>Summary (Dutch)</b>	<b>125</b>
<b>Acknowledgements</b>	<b>127</b>
<b>Scientific output</b>	<b>133</b>

# Introduction

## Turbulent flows

Everybody has most probably heard of the word turbulence. It has its origin from the Latin word *turba* and refers to the disorderly motion of a crowd. In the middle ages it was frequently used as a synonym for “trouble”. Nowadays, this “trouble” is still acknowledged not only by engineers and scientists, but also by tourists on a flight, as an aircraft will literally shake when it enters a zone of turbulence. In general, the word turbulence is used to indicate irregularities, fluctuations, and sometimes even chaos. While this can apply to many topics like politics in times of conflict of a government (political turbulence), in this dissertation we imply the fluid dynamical meaning of the word turbulence. While most scientists agree on what a turbulent flow is, they find it difficult to define an exact definition for the problem. It is therefore generally defined by typical characteristics such as randomness, non-linearity, enhanced diffusivity, vorticity, and dissipation [1]. To determine the level of turbulence, the so-called Reynolds number is used which is defined as the ratio of inertial to viscous forces. For macroscopic flows that are generally encountered in everyday life, the Reynolds number is much larger than unity, and therefore these flows are almost always turbulent. Many of these flows are hidden as these flows, such as for example air, are not visible to the human eye. Simply moving your hand through the air will create an incalculably complex motions of fluid. However, when paying a bit of attention, we can see the turbulence mixes the milk in our coffee, see the difference in density when hot air is rising above the street on sunny day, or by observing the flame from a candle. While not directly visible, turbulence is also seen in our Sun, in the clouds of Jupiter, and even in our arteries. One of the major difficulties in describing turbulence resides in the many characteristic length and time scales of the flow. Energy enters the system in large swirls or eddies, which “feed” their energy to smaller eddies. This already fascinated Leonardo da

Vinci, who, as one of the first, studied turbulent flows in the early 1500s (see figure 1). In this figure, Leonardo illustrates the many different length scales which are merely visible on the interface of the fluid surface.

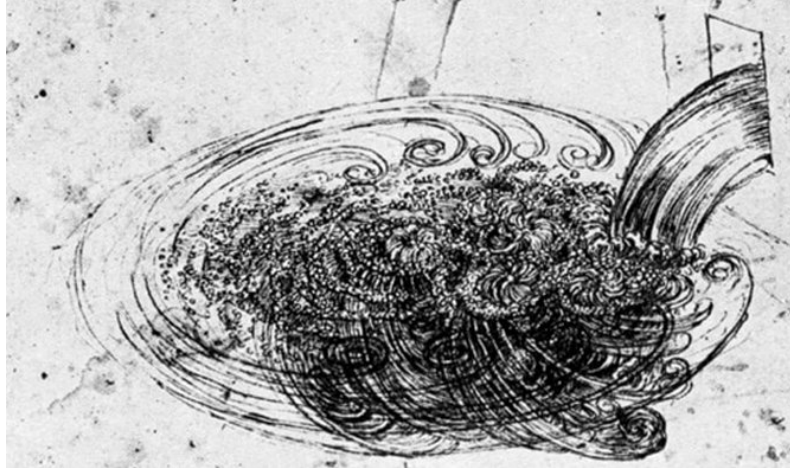


Figure 1: In the years between 1508 and 1513, Leonardo da Vinci illustrated the flow patterns produced by a water jet entering a larger vessel. The illustration depicts various sizes of eddies, typical for turbulent flows. *Source: Leonardo da Vinci (RL 12660, Windsor, Royal Library)*

When applying Newton's second law of motion,  $F = ma$ , to a fluid with regular material properties, *i.e.* a Newtonian fluid such as water, the governing equations of a turbulent flow can be deducted. While these, so-called Navier-Stokes equations (NS) are known for a relatively long time, it is yet one of the unsolved problems in physics. The problem lies in the non-linear nature of these equations and they can only be solved analytically for a couple of special cases. Therefore, to increase the understanding of turbulent flows we are still highly dependent on simulations and particularly laboratory experiments.

## Multiphase flows

Most flows occurring in nature or industrial applications do not consist of a single phase, but contain inclusions like particles, other (immiscible) fluids, or a gaseous phase. Examples of such flows are the transportation of pollen in the air, the transport of sediment in rivers, or the production of emulsions in the food industry. These bubbles, droplets, or particles are influenced by the underlying complex turbulent flow structures, and in response, the flow is itself also influenced by the inclusions. These interactions are far from trivial and complicate the problem of turbulence even further. The various physical mechanisms that occur in multiphase flows, such as particle collisions, bubble break-up, and droplet merging, lack a unifying view when it comes to theoretical descriptions. Experimentally, it is possible to measure global properties, such as torque very accurately. However, to get a better understanding of the underlying physics, also local quantities, such as droplet size are required. In experiments, it is difficult to get these local quantities as the different inclusions generally block the optical pathway for optical measurement techniques. This limits the non-invasive optical techniques to measure only very close to the boundary of the system. A way to overcome this is using a probe to measure inside the flow, however this probe will have an effect on the flow and thereby, introduce a bias to the measurements itself. With the increase in computing power, simulations on turbulent flows become more and more accessible and the gap between experiments and simulation is closing. One challenge for turbulent simulations in general is that all length scales in the system need to be resolved, from the largest energy input scales to the smallest dissipation scales. Currently, a few to multiple thousands of particles can be simulated in numerous flow geometries, including simulations of deformable droplets[2]. The major benefit for using simulations is that all flow variables, including the local quantities, are available. Unfortunately, adding inclusions will increase the complexity of these simulations tremendously, and therefore, limiting the Reynolds numbers possible to be simulated. Another difficulty lays in simulating dynamic processes such as coalescence and breakup of droplets as these can currently only be modelled. These severe limitations of the numerical tools can become very restrictive in simulating large scale systems that are relevant in industrial applications and fundamental research.

## Roughness and drag reduction

In the last fifty years, the field of turbulent drag reduction has received a serious amount of attention, especially from the maritime industry. With a projected consumption of 500 million tonnes per year of heavy fuel oil in 2020 [3], reducing this amount only with a few percent would already result in tremendous financial savings. As these types of fuel contain much higher sulphur levels than diesel, also the environment would greatly benefit from these drag reductions. Drag on maritime vessels is categorized in three components: pressure drag, residual drag, and skin friction. The pressure drag component is directly connected to the submerged geometry of the ship. Residual drag originates from the generation of bow and stern waves as seen in figure 2. To reduce these types of waves and thereby, reducing the energetic losses, a so-called *bulbous bow* is added just below the front waterline of large vessels. These are designed such that the waves generated by the bulb and bow cancel each other out. Skin friction drag is in general the largest component of drag which can account for up to 90 % of the total drag experienced by the vessel [4]. It is caused by the viscous drag in the



Figure 2: Boat sailing the Lyse fjord in Norway. The small vessel generates waves on the water surface, thereby, losing energy in the form of residual drag. *Photograph: Edmont (Wikipedia.org)*

boundary layer of the ship's hull for example highly dependent on the surface morphology of the wetted area. Not only do, for example, oysters, bacteria,

and biofilms increase the degree of roughness of the ship's hull, but when the Reynolds number (*i.e.* velocity of the ship) is sufficiently large, even a seemingly smooth surface becomes hydrodynamically rough. One way to cut down these frictional losses is to introduce an air layer on the ship's hull [5]. This layer acts as a lubrication layer between the water and the hull, reducing the wetted area. One of the first laboratory experiments created micro bubbles using electrolysis below a scale model [6] and found reductions of up to 30 %. Now, almost fifty years later, the underlying physics of the drag reduction are still not well understood and the key parameters are still not known. It is difficult to isolate parameters such as size, deformability, and shape, which can all be important for the process. While currently there are commercial products available, full scale experiments show an almost unpredictable rate of success. There are as many reports on reduction in drag, as there are cases reporting a drag increase [7]. It is not always clear if these studies report *net* drag reduction, *i.e.* take into account the additional energy required to inject air. All these uncertainties result in that the current, rather expensive technology is yet not applied to current maritime vessels.

## Taylor-Couette flow and Rayleigh-Bénard convection

Taylor-Couette flow (TC) and Rayleigh-Bénard convection (RB) are canonical systems in physics of fluids, and have already been called the “twins of turbulence research” [8]. This is because both systems are mathematically well-defined and they have exact energy balances between global energy input and dissipation.

In a Taylor-Couette geometry, the fluid is confined between two independently rotating concentric cylinders. These types of flows got a tremendous amount of attention in the past two decades [9]. A schematic of a typical setup is shown in figure 3a. The inner and outer cylinders have radii  $r_i$  and  $r_o$ , respectively, and both cylinders can rotate independently with angular velocities  $\omega_i$  and  $\omega_o$ . The gap size between the two cylinders is  $d = r_o - r_i$  and the total height of the cylinder is  $L$ . These measures can be combined to get the geometric parameters of the system: the aspect ratio  $\Gamma = L/d$  and the radius ratio  $\eta = r_i/r_o$ . The complete control parameters of this system consists of these geometric parameter, together with two Reynolds number,  $\text{Re}_{i,o} = \omega_{i,o} r_{i,o} d / \nu$ , where the subscripts denote the inner

or outer cylinder quantities and  $\nu$  is the kinematic viscosity. The primary response of the system is the torque  $\tau$  required to maintain the cylinders at constant speed. Typically, this torque is non-dimensionalized to the dimensionless torque  $G = \tau/(2\pi L\rho\nu^2)$  or the friction coefficient  $C_f = \tau/(L\rho\nu^2(\text{Re}_i - \eta\text{Re}_o)^2)$ , where  $\rho$  is the density of the fluid. In simulations, the local flow properties are accessible as the complete flow structure is known, however, the Reynolds numbers is still relatively limited, especially for multiphase flows. Therefore, to study these local flow properties we still heavily rely on laboratory measurements. Examples of such measurements are laser Doppler anemometry (LDA) and particle image velocimetry (PIV), which are both non-intrusive measurements but require optical access to the measurement area (see figure 3a).

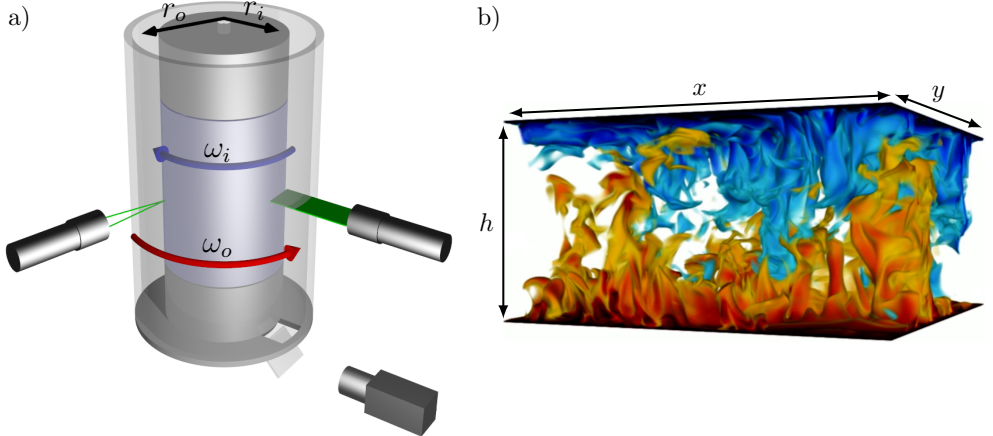


Figure 3: a) A schematic of a Taylor-Couette apparatus. The flow is confined between two concentric cylinders that can rotate independently. Torque is measured at the middle segmented cylinder (highlighted in diagram). The transparent outer cylinder makes it possible to access the flow using non-intrusive measurement techniques like LDA and PIV. b) Instantaneous temperature field from direct numerical simulations of a Rayleigh-Bénard convection cell. Only hot (red) and cold (blue) fluid is visualized to identify the plume structures. (*DNS snapshot courtesy of Erwin P. van der Poel*).

For Rayleigh-Bénard convection, the flow is heated from below and cooled from the top[10]. A typical instantaneous temperature snapshot from direct numerical simulations (DNS) is shown in figure 3b (courtesy Erwin P. van der Poel). The top and bottom plates are separated by a distance  $h$  and have a temperature difference  $\Delta$ . The driving parameter of the system is the Rayleigh number  $\text{Ra} = \beta g \Delta h^3 / (\kappa \nu)$ , where  $\beta$  is the

thermal expansion coefficient,  $g$  the acceleration due to gravity, and  $\kappa$  the thermal diffusivity. A three-dimensional system has two aspect ratios,  $\Gamma_x = x/h$  and  $\Gamma_y = y/h$ , for each horizontal dimension. In simulations it is common to express the fluid in form of a Prandtl number  $\text{Pr} = \nu/\kappa$ . The response of the system, after setting the control parameters  $\Gamma_x$ ,  $\Gamma_y$ ,  $\text{Pr}$ , and  $\text{Ra}$ , is the heat transport which is quantified by the Nusselt number  $\text{Nu} = J/J_c$ , where  $J$  is the heat flux from the bottom to the top plate and  $J_c$  is the pure conductive component.

TC flow and RB convection are mathematically very similar [11] and have conserved quantities: angular velocity flux in TC and heat flux in RB. Using this analogy, the quantities in TC can be rewritten in terms that resemble RB [12]. The driving and response of TC can be expressed as the Taylor number and a “ $\omega$ -Nusselt number” for TC:

$$\text{Ta} = \frac{1}{4} \left( \frac{1+\eta}{2\sqrt{\eta}} \right)^4 (r_o - r_i)^2 (r_i + r_o)^2 (\omega_i - \omega_o)^2 / \nu^2 \quad (1)$$

$$\text{Nu}_\omega = \frac{J_\omega}{J_{\omega,\text{lam}}} \quad (2)$$

here,  $J_\omega$  is the angular velocity flux from the inner to the outer cylinder and  $J_{\omega,\text{lam}}$  is the laminar flow contribution. By using these terms, the transport quantity scales as a function of the driving parameter with a certain scaling exponent  $\gamma$ , analogous to RB.

## Outline of the thesis

This thesis can be divided in two main topics: turbulent flows with inclusions and the interaction of patterned roughness on large flow structures. A flow holding inclusions can increase or decrease the skin friction at the boundary, *e.g.* a ship’s hull or the wall of a pipeline. The inclusions itself have many parameters like size, shape, and deformability. We however, are lacking the understanding how these parameters influence the skin friction. In chapter 1, by using solid neutrally buoyant spherical particles we disentangle three of these effects: size, deformability, and particle volume fraction. The drag of a rotating inner cylinder is measured while varying the size and the amount of these particles, and afterwards thoroughly compared to results from bubbly drag reduction. In chapter 2 the shape of the particle is changed to an

elongated cylinder and therefore, the orientation of a particle becomes important. Using high-speed imaging, we track the translation and orientation of the particles and investigate any collective effects. Chapter 3 presents the work on meta-stable emulsions in a turbulent flow. By applying intense shear, an immiscible fluid is suspended into another and therefore, creating deformable inclusions if the droplets are large. Exploiting the scaling of the momentum transfer in the ultimate regime of Taylor–Couette flow, it is possible to calculate an effective viscosity for the mixture. We answer how the morphology of the emulsion and the droplet size connects to the measured friction of the system. In chapter 4, using direct numerical simulations, we investigated the effect of non-homogeneous driving of a Rayleigh–Bénard cell. The top or both plates were divided in a stripe or checkerboard pattern, which consisted of alternating insulating or conducting temperature boundary conditions. While varying the periodic pattern using a wave number we have studied global quantities such as the effective heat transfer. Using a Fourier transform, it is possible to see the imprint of the pattern and study the penetration depth of such boundary conditions. In the same spirit as chapter 4, in chapter 5 we applied spanwise roughness to the driving cylinder of the Taylor–Couette setup, thereby, also having non-homogeneous driving of the flow. Using laser Doppler anemometry, it is possible to study the imprint of the pattern in the bulk flow. Using particle image velocimetry and torque measurements, we can investigate how the secondary flows, i.e. the turbulent Taylor vorices, are influenced by the spanwise roughness and how these are linked to the global transport. Finally, we conclude and summarize the work done in this thesis.

# 1

## Finite-sized rigid spheres in turbulent Taylor-Couette flow: Effect on the overall drag<sup>✉</sup>

---

We report on the modification of drag by neutrally buoyant spherical finite-sized particles in highly turbulent Taylor-Couette (TC) flow. These particles are used to disentangle the effects of size, deformability, and volume fraction on the drag, and are contrasted with the drag in bubbly TC flow. From global torque measurements we find that rigid spheres hardly decrease or increase the torque needed to drive the system. The size of the particles under investigation have a marginal effect on the drag, with smaller diameter particles showing only slightly lower drag. Increasing the particle volume fraction shows a net drag increase, however this increase is much smaller than can be explained by the increase in apparent viscosity due to the particles. The increase in drag for increasing particle volume fraction is corroborated by performing laser Doppler anemometry where we find that the turbulent velocity fluctuations also increase with increasing volume fraction. In contrast with rigid spheres, for bubbles the effective drag reduction also increases with increasing Reynolds number. Bubbles are also much more effective in reducing the overall drag.

---

<sup>✉</sup>Based on: **Dennis Bakhuis**, Ruben A. Verschoof, Varghese Mathai, Sander G. Huisman, Detlef Lohse, and Chao Sun *Finite-sized rigid spheres in turbulent Taylor-Couette flow: Effect on the overall drag*, J. Fluid Mech. **850**, 246–261 (2018).

## 1.1 Introduction

Flows in nature and industry are generally turbulent, and often these flows carry bubbles, drops, or particles of various shapes, sizes, and densities. Examples include sediment-laden rivers, gas-liquid reactors, volcanic eruptions, plankton in the oceans, pollutants in the atmosphere, and air bubbles in the ocean mixing layer [13]. Particle-laden flows may be characterized in terms of particle density  $\rho_p$ , particle diameter  $d_p$ , volume fraction  $\alpha$ , and Reynolds number  $Re$  of the flow. When  $d_p$  is small (compared to the dissipative length scale  $\eta_K$ ) and  $\alpha$  low ( $< 10^{-3}$ ), the system may be modelled using a point particle approximation with two-way coupling [14, 15, 16]. With recent advances in computing, fully resolved simulations of particle-laden flows have also become feasible. Uhlmann conducted one of the first numerical simulations of finite-sized rigid spheres in a vertical particle-laden channel flow [17]. They observed a modification of the mean velocity profile and turbulence modulation due to the presence of particles. A number of studies followed, which employed immersed boundary [18, 19], Physalis [20, 21], and front-tracking methods [22, 23, 24] to treat rigid particles and deformable bubbles, respectively, in channel and pipe flow geometries [25, 26, 17, 27, 28, 29, 30, 31]. Flows with dispersed particles, drops, and bubbles can, under the right conditions, reduce skin friction and result in significant energetic (and therefore financial) savings. In industrial settings this is already achieved using polymeric additives which disrupt the self-sustaining cycle of wall turbulence and dampen the quasi-streamwise vortices [32, 33]. Polymeric additives are impractical for maritime applications, and therefore gas bubbles are used with varying success rates [34, 7]. Local measurements in bubbly flows are non-trivial and the key parameters and their optimum values are still unknown. For example, it is impossible to fix the bubble size in experiments and therefore to isolate the effect of bubble size. Various studies hinted that drag reduction can also be achieved using spherical particles [35], also by using very large particles in a turbulent von Kármán flow [36]. In this latter study a tremendous decrease in turbulent kinetic energy (TKE) was observed. A similar, but less intense, decrease in TKE was also seen using a very low particle volume fraction[37]. By using solid particles it is possible to isolate the size effect on drag reduction and even though rigid particles are fundamentally different from bubbles, this can give additional insight into

the mechanism of bubbly drag reduction. The particle dynamics are highly influenced by the diameter of the particle[38]. This might or might not have a direct influence on the global drag of the system and has never been studied. Whether and when solid particles increase or decrease the drag in a flow is yet not fully understood and two lines of thought exist. On one side, it is hypothesized that solid particles *decrease* the overall drag as they damp turbulent fluctuations [35, 39]. On the other side, one could expect that solid particles *increase* drag as they shed vortices, which must be dissipated. In addition, they also increase the apparent viscosity. A common way to quantify this is the so called ‘Einstein relation’ [40]

$$\nu_\alpha = \nu \left( 1 + \frac{5}{2} \alpha \right), \quad (1.1)$$

where  $\nu$  is the viscosity of the continuous phase. This compensation is valid for the small  $\alpha$  values used in this chapter [41]. Direct measurements of drag in flows with solid particles are scarce, and the debate on under what condition they either enhance or decrease the friction has not yet been settled. Particles and bubbles may show collective effects (clustering) and experiments have revealed that this has significant influence on the flow properties [42, 43, 44, 45, 46, 47, 48, 49, 50, 51, 52, 53, 54, 55, 56]. In general, the Stokes number is used to predict this clustering behaviour, but for neutrally buoyant particles this is found to be insufficient [57, 58]. In addition, the position of the particles (or the particles clusters) is likely to have a large influence on the skin friction. It was shown in DNS at low Reynolds numbers, that the particle distribution is mainly governed by the bulk Reynolds number[59].

In order to study the effects of particles on turbulence it is convenient to use a closed setup where one can relate global and local quantities directly through rigorous mathematical relations. In this chapter the Taylor-Couette (TC) geometry [9]—the flow between two concentric rotating cylinders—is employed as this is a closed setup with global balances. The driving of the Taylor-Couette geometry can be described using the Reynolds number based on the inner cylinder (IC):  $Re_i = u_i d / \nu$ , where  $u_i = \omega_i r_i$  is the azimuthal velocity at the surface of the IC,  $\omega_i$  the angular velocity of the IC,  $d = r_o - r_i$  the gap between the cylinders,  $\nu$  the kinematic viscosity, and  $r_i(r_o)$  the radius of the inner(outer) cylinder. The geometry of Taylor-Couette flow is characterized by two parameters: the radius ratio  $\eta = r_i/r_o$  and the aspect ratio  $\Gamma = L/d$ , where  $L$  is the height of the cylinders. The response parameter of the system is the torque,  $\tau$ , required to maintain constant rotation speed of the inner cylinder. It was mathematically shown that in Taylor-Couette flow

the angular velocity flux defined as  $J^\omega = r^3 \left( \langle u_r \omega \rangle_{A,t} - \nu \frac{\partial}{\partial r} \langle \omega \rangle_{A,t} \right)$ , where the subscript  $A, t$  denotes averaging over a cylindrical surface and time, is a radially conserved quantity (Eckhardt, Grossmann, Lohse [12] (EGL)). One can, in analogy to Rayleigh-Bénard convection, normalize this flux and define a Nusselt number based on the flux of the angular velocity:

$$\text{Nu}_\omega = \frac{J^\omega}{J_{\text{lam}}^\omega} = \frac{\tau}{2\pi L \rho J_{\text{lam}}^\omega}, \quad (1.2)$$

where  $J_{\text{lam}}^\omega = 2\nu r_i^2 r_o^2 (\omega_i - \omega_o) / (r_o^2 - r_i^2)$  is the angular velocity flux for laminar, purely azimuthal flow and  $\omega_o$  is the angular velocity of the outer cylinder. In this spirit the driving is expressed in terms of the Taylor number:

$$\text{Ta} = \frac{1}{4} \sigma d^2 (r_i + r_o)^2 (\omega_i - \omega_o)^2 \nu^{-2}. \quad (1.3)$$

Here  $\sigma = \left( (1 + \eta) / (2\sqrt{\eta}) \right)^4 \approx 1.057$  is a geometric parameter (“geometric Prandtl number”), in analogy to the Prandtl number in Rayleigh-Bénard convection. In the presented work, where only the inner cylinder is rotated and the outer cylinder is kept stationary, we can relate Ta to the Reynolds number of the inner cylinder by

$$\text{Re}_i = \frac{r_i \omega_i d}{\nu} = \frac{8\eta^2}{(1 + \eta)^3} \sqrt{\text{Ta}}. \quad (1.4)$$

The scaling of the dimensionless angular velocity flux (torque) with the Taylor (Reynolds) number has been analysed extensively, see e.g. [60, 61, 62, 63, 64] and the review articles [65, 9], and the different regimes are well understood. In the current Taylor number regime it is known that  $\text{Nu}_\omega \propto \text{Ta}^{0.4}$ . Because this response is well known, it can be exploited to study the influence of immersed bubbles and particles [47, 48, 52, 53, 66] on the drag needed to sustain constant rotational velocity of the inner cylinder.

In this chapter we will use the TC geometry to study the effect of neutrally buoyant rigid spherical particles on the drag. We study the effects of varying the particle size  $d_p$ , the volume fraction  $\alpha$ , the density ratio  $\phi$ , and the flow Reynolds number  $\text{Re}$  on the global torque (drag) of the Taylor-Couette flow. The drag reduction is expressed as  $\text{DR} = (1 - \text{Nu}_\omega(\alpha)/\text{Nu}_\omega(\alpha = 0))$  and as we are interested in the net drag reduction, it is *not* compensated for increased viscosity effects using correction models, such as the Einstein relation.

The chapter is organized as follows. Section 1.2 presents the experimental setup. In section 1.3 we discuss the results. The findings are summarized and an outlook for future work is given in the last section.

## 1.2 Experimental setup

The experiments were conducted in the Twente Turbulent Taylor-Couette ( $T^3C$ ) facility [63]. A schematic of the setup is shown in figure 1.1. In this setup, the flow is confined between two concentric cylinders, which rotate independently. The top and bottom plates are attached to the outer cylinder. The radius of the inner cylinder (IC) is  $r_i = 0.200\text{ m}$  and the radius of the outer cylinder (OC) is  $r_o = 0.2794\text{ m}$ , resulting in a gap width of  $d = r_o - r_i = 0.0794\text{ m}$  and a radius ratio of  $\eta = r_i/r_o = 0.716$ . The IC has a total height of  $L = 0.927\text{ m}$  resulting in an aspect ratio of  $L/d = 11.7$ . The IC is segmented axially in three parts. To minimize the effect of the stationary end plates, the torque is measured only over the middle section of the IC with height  $L_{\text{mid}}/L = 0.58$ , away from the end plates. A hollow reaction torque sensor made by Honeywell is used to measure the torque which has an error of roughly 1% for the largest torques we measured. Between the middle section and the top and bottom section of the inner cylinder is a gap of 2mm.

The IC can be rotated up to  $f_i = \omega_i/(2\pi) = 20\text{ Hz}$ . In these experiments only the IC is rotated and the OC is kept at rest. The system holds a volume of  $V = 1111$  of working fluid, which is a solution of glycerol ( $\rho = 1260\text{ kg/m}^3$ ) and water. To tune the density of the working fluid, the amount of glycerol was varied between 0% and 40% resulting in particles being marginally heavy, neutrally buoyant, or marginally light. The system is thermally controlled by cooling the top and bottom plates of the setup. The temperature was kept at  $T = (20 \pm 1)\text{ }^\circ\text{C}$  for all the experiments, with a maximum spatial temperature difference of 0.2K within the setup, and we account for the density and viscosity changes of water and glycerol [67].

Rigid polystyrene spherical particles (*RGPballs S.r.l.*) were used in the experiments, these particles have a density close to that of water ( $940\text{--}1040\text{ kg/m}^3$ ). We chose particles with diameters  $d_p = 1.5, 4.0,$  and  $8.0\text{ mm}$ . To our disposal are: 2.221 of 1.5 mm diameter particles, 2.221 of 4 mm diameter particles, and 6.661 of 8 mm diameter particles, resulting in maximum volume fractions of 2%, 2%, and 6%, respectively. The particles are found to be nearly mono-disperse (99.9% of the particles are within  $\pm 0.1\text{ mm}$  of their target diameter). Due to the fabrication process, small air bubbles are sometimes entrapped within the particles. This results in a slight heterogeneous density distribution of the particles. After measuring

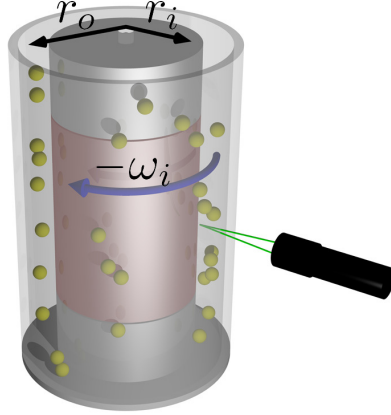


Figure 1.1: Schematic of the Taylor-Couette setup. Two concentric cylinders of radii  $r_{i,o}$  with a working fluid in between. Particles are not to scale. The inner cylinder rotates with angular velocity  $\omega_i$ , while the outer cylinder is kept at rest. We measure the torque on the middle section (highlighted). The laser Doppler anemometry (LDA) probe is positioned at mid height to measure the azimuthal velocity at mid gap.

the density distribution for each diameter, we calculated the average for all batches, which is  $\rho_p = (1036 \pm 5) \text{ kg/m}^3$ . By adding glycerol to water we match this value in order to have neutrally buoyant particles.

Using a laser Doppler anemometry (LDA) system (BSA F80, Dantec Dynamics) we captured the azimuthal velocity at mid-height and mid-gap of the system (see figure 1.1) and we performed a radial scan at mid-height. The flow was seeded with  $5 \mu\text{m}$  diameter polyamide particles (PSP-5, Dantec Dynamics). Because of the curved surface of the outer cylinder (OC), the beams of the LDA get refracted in a non-trivial manner, which was corrected for using a ray-tracing technique [68].

Obviously, LDA measurements in a multi-phase flow are more difficult to set up than for single phase flows, as the method relies on the reflection of light from tiny tracer particles passing through a measurement volume ( $0.07 \text{ mm} \times 0.07 \text{ mm} \times 0.3 \text{ mm}$ ). Once we add a second type of relatively large particles to the flow, this will affect the LDA measurements, mostly by blocking the optical path, resulting in lower acquisition rates. These large particles will also move through the measurement volume, but as these particles are at least 300 times larger than the tracers and thus much larger than the fringe pattern (fringe spacing  $d_f = 3.4 \mu\text{m}$ ), the reflected light is substantially different from a regular Doppler burst and does not result in a measured value. The minimal

signal-to-noise ratio for accepting a Doppler burst was set to 4. As a post-processing step the velocities were corrected for the velocity bias by using the transit time of the tracer particle.

## 1.3 Results

### 1.3.1 Effect of particle size

First we study the effect of changing the particle diameter on the torque of the system. In these experiments, we kept the particle volume fraction fixed at 2% and the density of the working fluid,  $\rho_f$ , at  $1036 \text{ kg/m}^3$ , for which the particles are neutrally buoyant. The results of these measurements are presented as  $\text{Nu}_\omega(\text{Ta})$  in figure 1.2a. Our curves are practically overlapping, suggesting that the difference in drag between the different particle sizes is only marginal. We compare these with the bubbly drag reduction data at similar conditions (hollow symbols) [66, 52, 47]. At low  $\text{Ta}$  the symbols overlap with our data. However, at larger  $\text{Ta}$ , the bubbly flow data shows much lower torque (drag) than the particle-laden cases. As we are in the ultimate regime of turbulence where  $\text{Nu}_\omega$  effectively scales as  $\text{Nu}_\omega \propto \text{Ta}^{0.4}$  [68, 64], we compensate the data with  $\text{Ta}^{0.40}$  in figure 1.2b to emphasize the differences between the datasets. For the single phase case, this yields a clear plateau. For the particle-laden cases, the lowest drag corresponds to the smallest particle size. The reduction is however quite small (< 3%). The compensated plots also reveal a sudden increase in drag at a critical Taylor number  $\text{Ta}^* = 0.8 \times 10^{12}$ . The jump is more distinct for the smaller particles, and might suggest a reorganisation of the flow [69]. Beyond  $\text{Ta}^*$ , the drag reduction is negligible for the larger particles (4 mm and 8 mm spheres). However, for the 1.5 mm particles, the drag reduction seems to increase, and was found to be very repeatable in experiments. Interestingly, the size of these particles is comparable to that of the air bubbles [52]. This might suggest that for smaller size particles at larger  $\text{Ta}$ , one could expect drag reduction. At the increased viscosity of the suspension, a maximum  $\text{Ta} \approx 3 \times 10^{12}$  could be reached in our experiments. We have performed an uncertainty analysis by repeating the measurements for the single phase, and for the cases with 8 mm and 1.5 mm particles multiple times and calculating the maximum deviation from the ensemble average. The left error bar indicates the maximum deviation for all measurements combined and is  $\approx 1\%$ . For  $\text{Ta} \geq 2 \times 10^{12}$ , we see an increase in uncertainty of 1.7% (shown by the right error bar in figure 1.2b), which is only caused by the 1.5 mm particles. These tiny particles can accumulate in

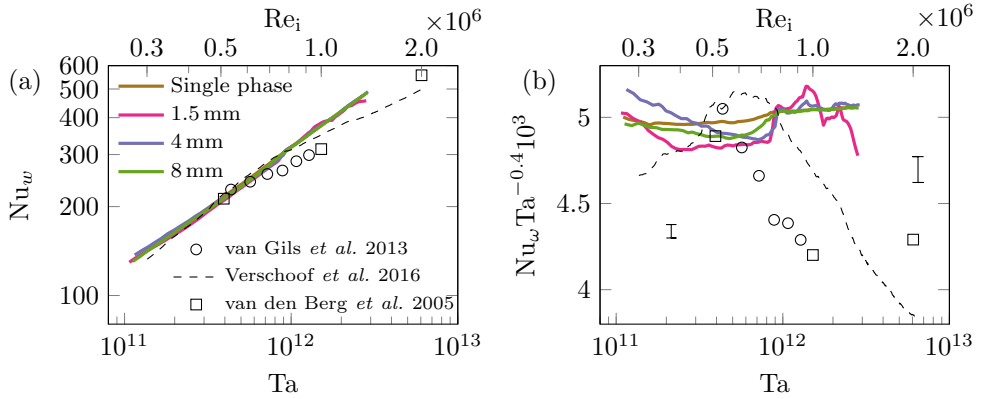


Figure 1.2: (a)  $\text{Nu}_\omega(\text{Ta})$  for 2 % particle volume fraction with particle diameters of 1.5 mm, 4.0 mm, and 8.0 mm, and for comparison the single phase case. Data from comparable bubbly drag reduction studies are plotted using black markers. (b) Same data, but now as compensated plot  $\text{Nu}_\omega/\text{Ta}^{0.40}$  as function of  $\text{Ta}$ . The error bar indicates the maximum deviation for repeated measurements from all measurements combined (coloured curves) which is less than 1 %. At  $\text{Ta} \geq 2 \times 10^{12}$ , the 1.5 mm particles show an increased uncertainty of 1.7 %, which is indicated by the right error bar.

the 2 mm gap between the cylinder segments and thereby increase the uncertainty. Above  $\text{Ta} \geq 2 \times 10^{12}$ , both, the 8 mm and 4 mm particles, show a maximum deviation below 0.25 %.

Below  $\text{Ta}^*$ , the drag reduction due to spherical particles appears to be similar to bubbly drag reduction [52]. However, in the lower  $\text{Ta}$  regime, the bubble distribution was highly non-uniform due to buoyancy of the bubbles [47, 52, 66]. Therefore, the volume fractions reported were only the global values, and the torque measurements were for the mid-sections of their setups. What is evident from the above comparisons is that in the high  $\text{Ta}$  regime, air bubbles drastically reduce the drag, reaching far beyond the drag modification by rigid spheres.

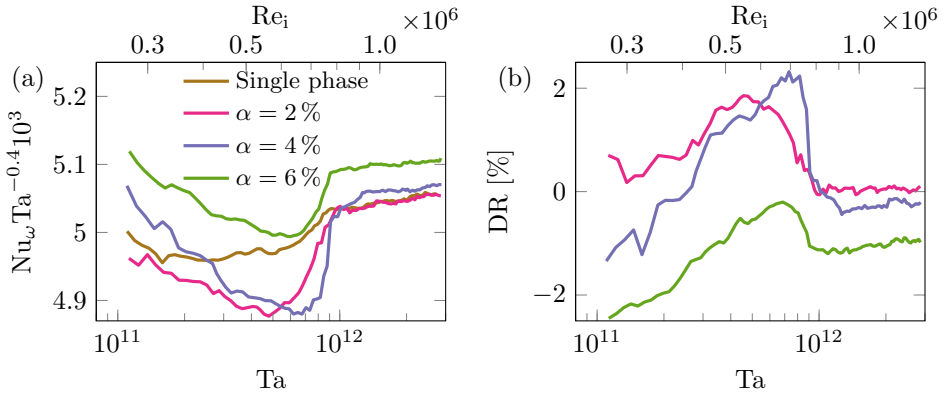


Figure 1.3: (a)  $Nu_\omega(Ta)$ , compensated by  $Ta^{0.4}$ , for 8mm particles with various particle volume fractions and for comparison the single phase case. (b) Drag reduction, defined as  $DR = (1 - Nu_\omega(\alpha)/Nu_\omega(\alpha = 0))$ , plotted against  $Ta$ .

### 1.3.2 Effect of particle volume fraction

The next step is to investigate the effect of the particle volume fraction on the torque. For the 8mm particles, we have the ability to increase the particle volume fraction up to 6 %. This was done in steps of 2 %, and the results are plotted in compensated form in figure 1.3a. The normalised torque increases with the volume fraction of particles. The 6 % case shows the largest drag. Figure 1.3b shows the same data in terms of drag reduction as function of  $Ta$ . A 2 % volume fraction of particles gives the highest drag reduction. With increasing  $\alpha$  the drag reduction decreases. These measurements are in contrast with the findings for bubbly drag reduction [52], for which the net drag decreases with increasing gas volume fraction. of drag in a particle-laden flow is the larger apparent viscosity. If we would calculate the apparent viscosity for our case with the Einstein relation (equation 1.1) for  $\alpha = 6\%$ , the drag increase would be 15 %, as compared to the pure working fluid. Including this effect in our drag reduction calculation would result in reductions of the same order. However, when comparing the drag with or without particles, the *net* drag reduction is practically zero. This result is different from the work a in turbulent channel flow where they found that the drag increased more than the increase of the viscosity[30].

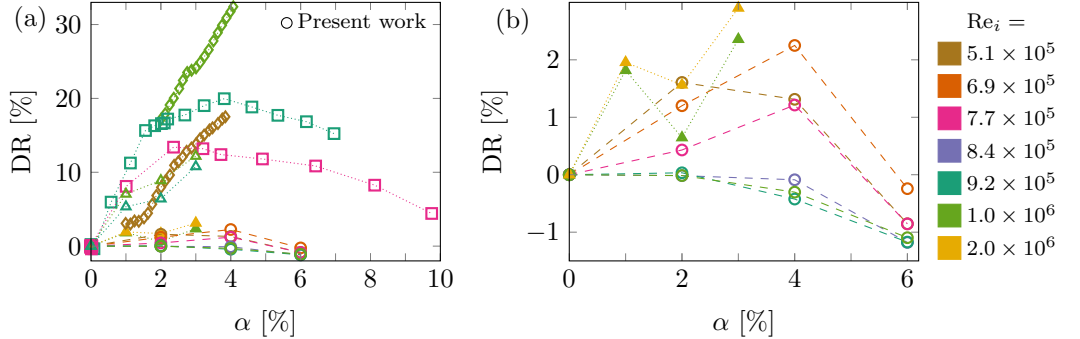


Figure 1.4: (a) Drag reduction as function of particle volume fraction from  $\circ$ :  $d_p = 8$  mm particles from present work compared to similar gas volume fractions from  $\square$ : van den Berg[47],  $\diamond$ : van Gils[52], and  $\Delta$ : Verschoof[66]. Symbols indicate the different studies while colours differentiate between the Reynolds numbers. The current work has DR defined as  $(1 - \text{Nu}_\omega(\alpha)/\text{Nu}_\omega(\alpha = 0))$ ; the other studies use dimensionless torque  $G$  [52], friction coefficient  $c_f$  [47], or plain torque  $\tau$  [66] to define DR. (b) Zoom of the bottom part of (a) where the data from the present work is compared to bubbly drag reduction data using 6 ppm of surfactant [66]

For a better comparison with bubbly drag reduction, we plot the drag reduction as a function of (gas or particle) volume fraction  $\alpha$ ; see figure 1.4a. Different studies are shown using different symbols, and  $\text{Re}$  is indicated by colours. None of the datasets were compensated for the changes in effective viscosity. DR is defined in slightly differently way in each study: van den Berg [47] makes use of the friction coefficient  $(1 - c_f(\alpha)/c_f(0))$ ; van Gils [52] uses the dimensionless torque  $G = \tau/(2\pi L_{mid}\rho\nu^2)$ ,  $(1 - G(\alpha)/G(0))$ ; and Verschoof [66] uses the plain torque value  $(1 - \tau(\alpha)/\tau(0))$ . While the rigid particles only showed marginal drag reduction, some studies using bubbles achieve dramatic reduction of up to 30 % and beyond. Figure 1.4b shows a zoomed in view of the bottom part of the plot with the rigid sphere data. The triangles denote the data from Verschoof [66], corresponding to small bubbles in the Taylor-Couette system. The rigid particles and the small bubbles show a similar drag response. What is remarkable is that this occurs despite the huge difference in size. The estimated diameter of the bubbles in Verschoof [66] is 0.1 mm, while the rigid spheres are about two orders in magnitude larger. This provides key evidence that the particle size alone is not enough to cause drag reduction, also the density ratio of the particle and the carrier fluid is of importance.

### 1.3.3 Effect of marginal changes in particle density ratio

With the effects of particle size and volume fraction revealed, we next address the sensitivity of the drag to marginal variations in particle density. A change in the particle density ratio brings about a change in the buoyancy and centrifugal forces on the particle, both of which can affect the particle distribution within the flow. We tune the particle to fluid density ratio  $\phi \equiv \rho_p/\rho_f$  by changing the volume fraction of glycerol in the fluid, such that the particles are marginally buoyant ( $\phi = 0.94, 0.97$ ), neutrally buoyant ( $\phi = 1.00$ ) and marginally heavy ( $\phi = 1.04$ ) particles. In figure 1.5a we show the compensated  $\text{Nu}_\omega$  as function of  $\text{Ta}$  for various  $\phi$ .  $\alpha$  was fixed to 6 % and only 8 mm particles were used. The darker shades of colour correspond to the single phase cases, while lighter shades correspond to particle-laden cases. In general, the single phase drag is larger as compared to the particle-laden cases. However, there is no striking difference between the different  $\phi$ . In figure 1.5b, we present the drag reduction for particle-laden cases at different density ratios. On average we see for all cases drag modification of approximately  $\pm 2\%$ . We can also identify a small trend in the lower  $\text{Ta}$  region: the two larger  $\phi$  (heavy and neutrally buoyant particles) tend to have a drag increase, while the smaller  $\phi$  cases (both light particles) have a tendency for drag reduction. Nevertheless, the absolute difference in DR between the cases is within 4%. The above results provide clear evidence that minor density mismatches do not have a serious influence on the global drag of the system. To investigate for strong buoyancy effects, additional measurements were done using 2 mm expanded polystyrene particles ( $\phi = 0.02$ ). However, due to the particles accumulating between the inner cylinder segments leading to additional mechanical friction, these measurements were inconclusive.

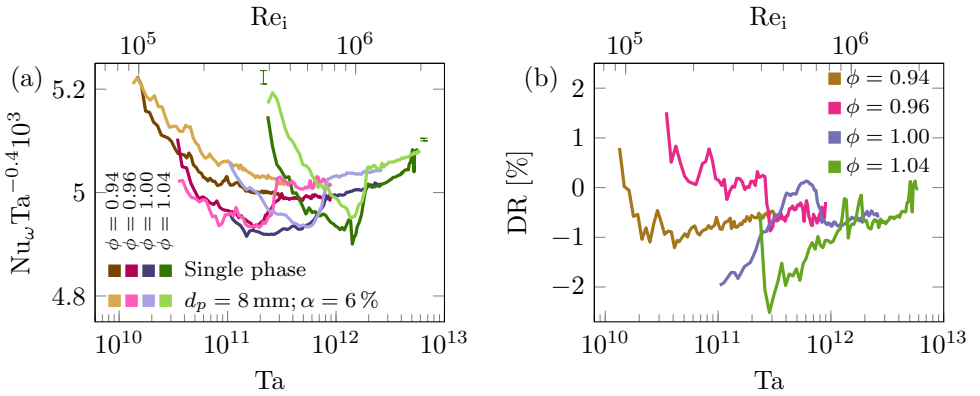


Figure 1.5: (a)  $\text{Ta}$  as function of  $\text{Nu}_\omega$  compensated by  $\text{Ta}^{0.4}$  for various density ratios  $\phi = \rho_p/\rho_f$  indicated by the corresponding colour. The darker shades indicate the single phase cases while the lighter shades show the cases using 6 % particle volume fraction of 8 mm diameter particles. Due to the increase in viscosity the maximum attainable  $\text{Ta}$  is lower for larger density ratios. The uncertainty is again estimated using the maximum deviation from the average for multiple runs and here only shown for the green curves. This value is slightly below 1 % at lower  $\text{Ta}$  and decreases with increasing  $\text{Ta}$  to values below 0.25 %. This trend is seen for all  $\phi$ . (b) Drag reduction, calculated from the data of figure 5a, plotted against  $\text{Ta}$ . The drag reduction is defined as  $\text{DR} = (1 - \text{Nu}_\omega(\alpha = 6\%)/\text{Nu}_\omega(\alpha = 0))$ .

### 1.3.4 Flow statistics using particles

In the above sections, we presented the effects of changing particle size, volume fraction, and density on the global drag of the system. Next we look into local flow properties using LDA while the particles are present. First, we collected a total of  $1 \times 10^6$  data points of azimuthal velocity at mid-height and mid-gap. These were captured over a period of approximately  $3 \times 10^4$  cylinder rotations. From this data we calculate the probability density function (PDF) of  $u_\theta$  normalised by  $u_i$  for various  $\alpha$ , shown in figure 1.6a. The particle size was fixed to 8 mm and the Reynolds number was set to  $1 \times 10^6$ . From this figure we see a large increase in turbulent fluctuations, resulting in very wide tails. While the difference between 2%, 4%, and 6% is not large, we can identify an increase in fluctuations with increasing  $\alpha$ . These increased fluctuations can be explained by the additional wakes produced by the particles [39, 55]. The increase in fluctuations can also be visualized using the standard deviation of  $\sigma(u_\theta) = \langle u'_\theta^2 \rangle^{1/2}$  normalised by the standard deviation of the single phase case—see figure 1.6b. In this figure,  $\sigma(u_\theta)$  is shown for three different Re, again for 8 mm particles. In general, we see a monotonically increasing trend with  $\alpha$ , and it seems to approach an asymptotic value. One can speculate that there has to be an upper limit for fluctuations which originate from wakes of the particles. For large  $\alpha$  the wakes from particles will interact with each other and with the carried flow.

Measurements using 4 mm particles yielded qualitatively similar results. It is known that in particle-laden gaseous pipe flows, large particles can increase the turbulent fluctuations, while small particles result in turbulence attenuation [70, 71, 72]. The LDA measurements were not possible with the smallest particles (1.5 mm), as the large amount of particles in the flow blocked the optical paths of the laser beams.

We are confident that for these bi-disperse particle-laden LDA measurements, the large particles do not have an influence on the measurements as these *millimetric*-sized particles are much larger than the fringe spacing ( $d_f = 3.4 \mu\text{m}$ ) and do not show a Doppler burst. However, during the measurements the particles get damaged and small bits of material are fragmented off the particles. We estimate the size of these particles slightly larger than the tracer particles and these can have an influence on the LDA measurements as they do not act as tracers.

How the average azimuthal velocity changes with particle radius is shown

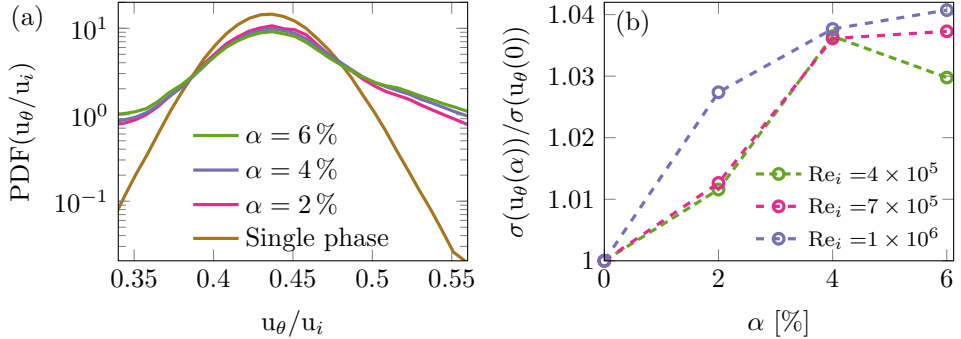


Figure 1.6: (a) PDF of  $u_\theta/u_i$  for various  $\alpha$  and the single phase case. The particle size was fixed to 8 mm and  $Re_i = 1 \times 10^6$  for all cases. (b) Standard deviation of the azimuthal velocity normalized by the standard deviation of the single phase case for three different  $Re$  for a fixed particle size of 8 mm.

in figure 1.7. We measured a total of  $3 \times 10^4$  data points during approximately 900 cylinder rotations. Again, the data were corrected for velocity bias by using the transit time as a weighing factor. Figure 1.7a shows the effect of particle size for  $\alpha = 2\%$ , and figure 1.7b shows the effect of particle volume fraction for 8 mm particles. Both figures additionally show the high-precision single phase data from another study [73] for which our single phase measurements are practically overlapping. Since LDA measurements close to the inner cylinder are difficult, due to the reflecting inner cylinder surface, we limited our radial extent to  $\tilde{r} = (r - r_i)/(r_o - r_i) = [0.2, 1]$ . We found that the penetration depth of our LDA measurements is the smallest for experiments with the smallest particles and the largest  $\alpha$ . All differences with the single phase case are only marginal and we can conclude that the average mean velocity is not much affected by the particles in the flow, at least for  $\tilde{r} \geq 0.2$ .

To get an idea of the fluctuations we can use the previous data to construct a two-dimensional PDF of the azimuthal velocity as function of radius. These are shown for  $Re = 1 \times 10^6$  using 8 mm particles at various  $\alpha$  and the single phase case in figure 1.8. First thing to notice is again that the penetration depth is decreasing with increasing  $\alpha$ . The single phase case shows a narrow banded PDF. When  $\alpha$  is increased, for the lower values of  $\tilde{r}$  the PDF is much wider. While it makes sense that an increase in  $\alpha$  increases the fluctuations due to the increased number of wakes of particles, this is expected everywhere

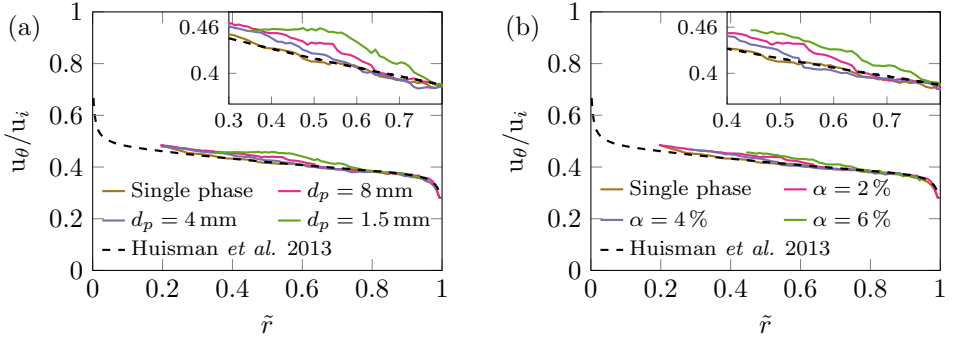


Figure 1.7:  $u_\theta$  normalised by the velocity of the inner cylinder wall  $u_i$  as function of the normalised radius for various  $d_p$  while  $\alpha = 2\%$  (a) and various  $\alpha$  while  $d_p = 8 \text{ mm}$  (b). In all cases  $\text{Re}_i$  is fixed to  $1 \times 10^6$ . For comparison, the single phase case using water at  $\text{Re}_i = 1 \times 10^6$  from Huisman [73] is also plotted in dashed black in both plots. Both figures have an inset showing an enlargement of the centre area from the same figure.

in the flow, not only closer to the inner cylinder. It is possible that the particles have a preferred concentration closer to the inner cylinder. We have tried to measure the local concentration of particles as function of radius but failed due to limited optical accessibility. Therefore, we can only speculate under what circumstances there would be an inhomogeneous particle distribution which would lead to the visible increase in fluctuations. The first possibility is a mismatch in density between the particle and the fluid, which would result in light particles ( $\phi < 1$ ) to accumulate closer to the inner cylinder. Another possibility is that due to the rotation of the particle, an effective lift force arises, leading to a different particle distribution in the flow. While this is quite plausible, this is difficult to validate as we would need to capture the rotation. The fragments of plastic that are sheared off the particles can also have a bias to the LDA measurement. While we estimate them to be larger than the tracers, they might still be small enough to produce a signal and they might not follow the flow faithfully.

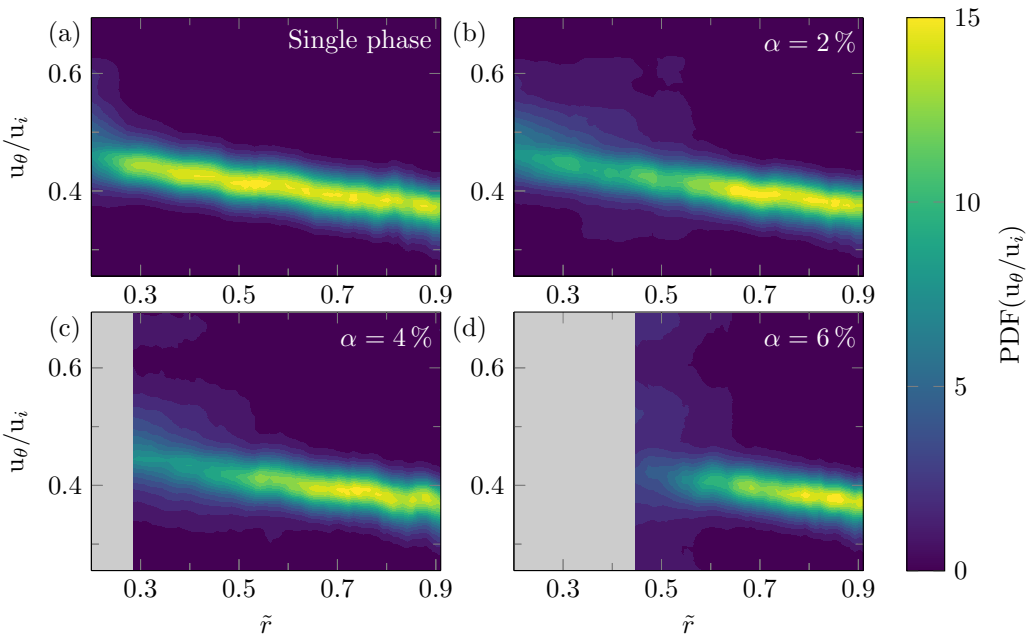


Figure 1.8: PDF of the normalised azimuthal velocity as a function of normalised radial position for various  $\alpha$  for the case of 8 mm particles and the single phase case while keeping  $Re$  at  $1 \times 10^6$ . With increasing  $\alpha$  the maximum penetration depth decreases. The grey areas indicate radial positions for which no data is available.

## 1.4 Conclusions and outlook

We have conducted an experimental study on the drag response of a highly turbulent Taylor-Couette flow containing rigid neutrally buoyant spherical particles. We have found that, unlike the case of bubbles used in prior works [52, 66], rigid particles barely reduce (or increase) the drag on the system, even for cases where their size was comparable to that of bubbles used in other studies. There was no significant size effect. Even for very large particles, which can attenuate turbulent fluctuations and generate wakes, there was no distinct difference with the single phase flow. We also varied the volume fraction of the particles in the range 0%–6%. The particle volume fraction has no greater effect on the system drag than what is expected due to changes in the apparent viscosity of the suspension. Further, we tested the sensitivity of our drag measurements to marginal variations in particle to fluid density ratio  $\phi$ . A trend was noticeable, towards drag reduction when  $\phi$  was reduced from 1.00 to 0.94. This suggests that a low density of the particle could be a necessary ingredient for drag reduction. Finally, we have also probed the local flow at the mid height and mid gap of the system using LDA. With the addition of particles, the liquid velocity fluctuations are enhanced, with wider tails of the distributions. A finite relative velocity between the particle and the flow around it can cause this increase in velocity fluctuations [54], as seen for bubbly flows (pseudo-turbulence), and in situations of sedimenting particles in quiescent or turbulent environments [71]. In the present situation, the relative velocity between the particle and the flow is expected, owing to the inertia of the finite-sized particles we used. There is only a marginal deviation from the single phase case in the average azimuthal velocity over the radial positions measured using any size or concentration of particles measured. From the two-dimensional PDFs, we see that closer to the inner cylinder, using smaller  $d_p$  or larger  $\alpha$ , the PDF gets wider. This can be due to a preferential concentration of the particles or a slight density mismatch.

Our study is a step towards a better understanding of the mechanisms of bubbly drag reduction. Bubbles are deformable, and they have a tendency to migrate towards the walls, either due to lift force [27], or due to the centripetal effects [52]. When compared to the drag reducing bubbles [52, 66], our particles do not deform, and they do not experience centripetal effects as they are density matched. At least one of these differences must

therefore be crucial for the observed, bubbly drag reduction in those experiments. In a future investigation, we will conduct more experiments using very light spherical particles that experience similar centripetal forces as the bubbles in van Gils [52], but are non-deformable. These particle need to be larger than the size of the gap between the inner cylinder segments and very rigid, or the setup needs to be modified to close the gap between the IC segments. Such experiments can then disentangle the role of particle density on drag reduction from that of the particle shape.



# 2

## Statistics of rigid fibers in strongly sheared turbulence<sup>✉</sup>

---

Practically all flows are turbulent in nature and contain some kind of irregularly-shaped particles, e.g. dirt, pollen, or life forms such as bacteria or insects. The effect of the particles on such flows and vice-versa are highly non-trivial and are not completely understood, particularly when the particles are finite-sized. Here we report an experimental study of millimetric fibers in an strongly sheared turbulent flow. Remarkably, the fibers do not align with the vorticity vector as they do in homogeneous turbulence, but, instead, show a universal preferred orientation of  $-0.38\pi \pm 0.05\pi$  ( $-68 \pm 9^\circ$ ) with respect to the mean flow direction, for all studied Reynolds numbers, fiber concentrations, and locations. In spite of the finite-size of the anisotropic particles, we can explain the preferential alignment by using Jefferey's equation, which provides evidence of the benefit of a simplified point-particle approach. Furthermore, the fiber angular velocity is strongly intermittent, again indicative of point-particle-like behavior in turbulence. Thus large anisotropic particles still can retain signatures of the local flow despite classical spatial and temporal filtering effects.

---

<sup>✉</sup>Based on: **Dennis Bakhuis**, Varghese Mathai, Ruben A. Verschoof, Rodrigo Ezeta, Sander G. Huisman, Detlef Lohse, and Chao Sun *Statistics of rigid fibers in strongly sheared turbulence*, under review.

## 2.1 Introduction

Control and prediction of flows containing anisotropic particles are important for many industrial settings. For example, in the paper production process, the alignment of the fibers of the pulp determines the mechanical strength of the paper [74]. In nature, one objective is on flow prediction, e.g. the dispersion of pollen and seeds [75] or sediment transport in rivers [76]. The addition of fibers to the flow can have significant consequences on the rheology of the suspensions [77, 78]. In homogeneous turbulence, rod-like fibers can become preferentially aligned with the vorticity vector [79, 80, 81, 82, 83]. When the fibers behave as tracers, their orientations become correlated with the local velocity gradients in the flow, and this alignment strongly depends on the fiber shape [82]. In the case of prolate spheroids, the orientation vector is likely to align with the axis of symmetry of the flow [84]. In comparison, the behavior of fibers in viscous shear flows can be noticeably different. Here, the fiber orientation is a result of the competition between alignment by mean velocity gradients and randomization by fluctuating velocity gradients [83]. This can lead to either an alignment parallel to the flow direction [85, 86] or at an angle with the wall [87, 88, 89, 90, 91, 92, 93]. However, most of the studies in shear flows have been done by numerical simulations, addressing the simplified case of inertial point-like fibers without gravity. Often a point-particle approach is used, which is considered to be limited in its applicability to small sub-Kolmogorov scale [94, 95] particles, and they have a negligible particle Reynolds number [96].

In most practical situations, however, the suspended particles are not small, and they have a finite Reynolds number. Fully resolved numerical simulations, addressing the effect of fibers in turbulent channel flows showed that finite size effects lead to fiber–turbulence interactions that are significantly different from those of point-like particles[97]. This can lead to an increased dissipation near the particle, and decreased dissipation in its wake. In such situations, no analytic expressions are available for the forces and torques acting on the particles. In general, it is considered that such finite-sized particles filter out the spatial and temporal flow fluctuations [13, 98, 99, 100, 37, 54, 55, 101, 56], and hence do not actively respond to the local gradients in the flow. Few experiments have explored this regime of finite sized rod-like fibers in sheared turbulence.

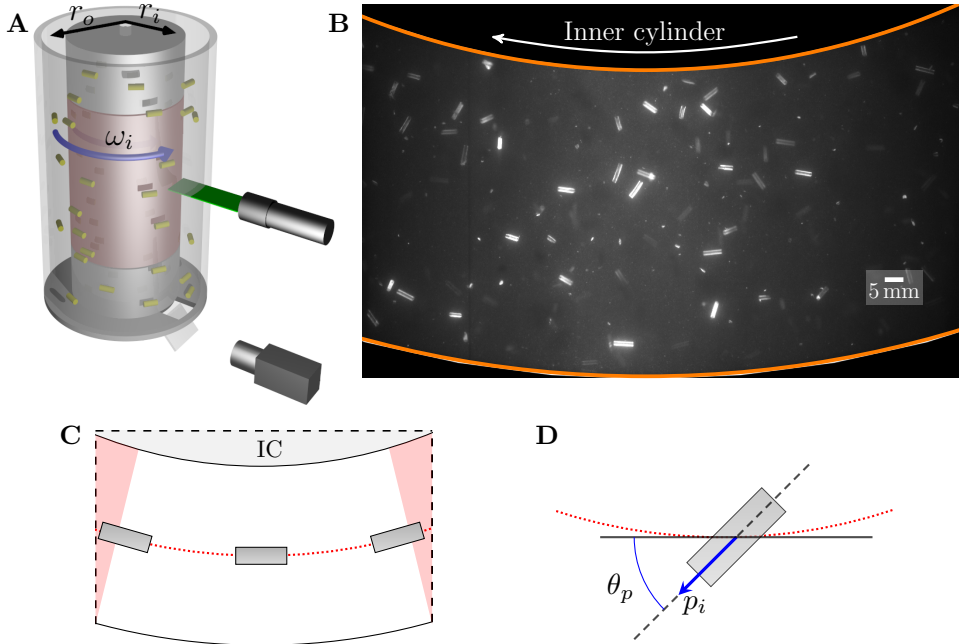


Figure 2.1: (A) Schematic of the experimental apparatus (not to scale). The flow is confined between two concentric independently rotating cylinders with radii  $r_i$  and  $r_o$ . Only the inner cylinder (IC) rotates with an angular velocity  $\omega_i$ . A mirror and a window in the bottom plate provide optical access to the  $r$ - $\theta$  plane for a high-speed camera. (B) A typical still image with the inner and outer cylinder highlighted in orange. The fibers (aspect ratio  $\Lambda = 5.3$ ) are clearly visible as white rods.  $Re_i = 1.7 \times 10^5$  and  $\alpha = 0.05\%$ . (C) Schematic of the  $r$ - $\theta$  plane. The orientation of the particle,  $\theta_p$ , is zero when it is aligned with the IC. Fibers with their center in the red areas are removed from all statistics. (D) Definition of the orientation,  $\theta_p$ , and the orientation vector,  $p_i$ , of a fiber.  $\theta_p$  is measured with respect to the azimuthal direction and is defined positive in the counter-clockwise direction.

## 2.2 Experiments and results

In this chapter we probe the dynamics of a suspension of millimetric rod-like fibers in a strongly turbulent Taylor–Couette (TC) flow (see figure 2.1AB). The reason for choosing this geometry is at least three-fold: (i) it is a closed geometry, allowing for direct relationships between local and global quantities [12], (ii) there are no spatial transients, *i.e.*, the turbulence intensity does not depend on the streamwise position as it does in channels and pipes, and (iii) it allows for high Reynolds numbers in a limited space [9]. All experiments are conducted in the Twente Turbulent Taylor–Couette ( $T^3C$ ) facility [63], which confines the flow between two concentric cylinders (see figure 2.1A). The inner and outer cylinders radii are  $r_i = 0.2000\text{ m}$  and  $r_o = 0.2794\text{ m}$ , respectively, giving a radius ratio of  $\eta = r_i/r_o = 0.716$  and a gap width  $d = 79.4\text{ mm}$ . The height of the system is  $L = 0.927\text{ m}$ , which results in an aspect ratio of  $\Gamma = L/d = 11.7$ . We rotate the inner cylinder (IC) with angular velocity  $\omega_i$  while the outer cylinder (OC) is kept at rest. The flow is seeded with rigid fibers of length  $\ell = 5.22 \pm 0.07\text{ mm}$ , cut from a PMMA optical fiber of diameter  $d_p = 0.99 \pm 0.01\text{ mm}$  (aspect ratio  $\Lambda = \ell/d_p = 5.3$ ). The 2D projection of the orientation angle on the radial-azimuthal plane,  $\theta_p$ , is defined to be zero when the fiber is aligned with the IC (figure 2.1C) and positive values are in the counter-clockwise direction (figure 2.1D). To minimize density effects, glycerol and water are mixed 1:1, giving a density ratio of  $\rho_p/\rho_{\text{fluid}} = 1210\text{ kg m}^{-3}/1140\text{ kg m}^{-3} = 1.06$ . The dominant velocity is in the azimuthal direction. Velocities in the axial and radial directions are due to secondary flows and are approximately 5 % of the azimuthal velocity. While the particles are free to rotate in all directions, the largest velocity gradient is in the radial direction, resulting in a rotation in the axial direction. For the flow under consideration, the control parameters are the Reynolds number  $Re_i = \omega_i r_i (r_o - r_i)/\nu$  and the volume fraction of the fibers  $\alpha$ . Here  $\nu$  is the the kinematic viscosity.  $Re_i$  is varied by changing  $\omega_i$ , resulting in a  $Re_i$  range from  $8.3 \times 10^4$  to  $2.5 \times 10^5$  which lies in the so-called ultimate regime [60, 63, 102, 103] of turbulent Taylor–Couette flow, where both the bulk and boundary layers are turbulent. From the volume fraction of fibers  $\alpha = 0.025\%$  to  $\alpha = 0.100\%$ , the suspensions we study are on the border of dilute and dense suspensions, which has either two- or four-way coupling [14]. To capture the orientation and velocities of the fibers, images in the radial-azimuthal plane are captured using a Photron SA-X2 high-speed camera. Illumination comes from

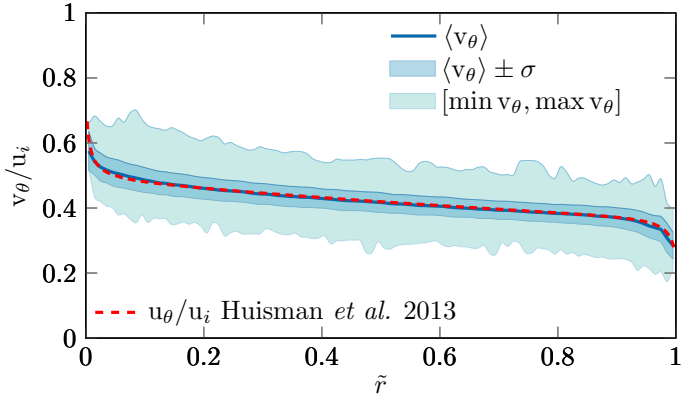


Figure 2.2: Fiber velocity as a function of the dimensionless radius  $\tilde{r} = (r - r_i)/d$  for  $Re_i = 1.7 \times 10^5$ ,  $\alpha = 0.05\%$ , and  $\tilde{z} = z/L = 0.24$ . All velocities are normalized using the velocity of the IC  $u_i$ . For comparison, the azimuthal flow profile is included as a red dashed line. We find that the azimuthal velocity of the fibers is very close to the velocity of the flow.

a Litron LDY-303 pulsed laser and sheet optics. Figure 2.1B shows a typical captured image in which the IC and OC are highlighted. A total amount of 64 thousand images per case ( $Re_i, \alpha, z/L$ ) are captured and the position and orientation of each of the fibers are extracted, see figure 2.1CD. These are then tracked over time, from which, the velocity,  $v_\theta$ , and angular velocity,  $\dot{\theta}_p$ , can be determined. We find that the fibers distribute nearly homogeneously in the radial direction of the measurement volume. Moreover, we find that their azimuthal velocity, normalized using the velocity of the IC,  $u_i$ , closely follows the azimuthal velocity profile of the flow,  $u_\theta$ , [73], see figure 2.2. These fibers, therefore, do not show clustering or relative velocities, which seems surprising considering their rather large size. However, the absence of clustering can be expected, since the fibers are nearly neutrally buoyant [50, 98, 58]. Yet, this cannot explain the absence of relative velocities with the flow (see figure 2.2) we observe in our experiment. To explain this behavior, we calculate the Stokes number  $Stk_K \equiv \tau_v/\tau_K$ , where  $\tau_v = \frac{\ell^2}{3\beta\nu}$  with  $\beta = \frac{3\rho_f}{2\rho_p + \rho_f}$  is the particle response time [104], and  $\tau_K = \sqrt{\frac{\nu}{\epsilon}}$  is the Kolmogorov time scale. For our flow conditions we find that  $\tau_K = [2.2 \text{ ms}, 0.5 \text{ ms}]$  and the Kolmogorov length scale  $\eta_K = [113 \mu\text{m}, 52.6 \mu\text{m}]$ , where each two values correspond to our lowest and highest Reynolds numbers  $Re_i = 8.3 \times 10^4$  and  $2.5 \times 10^5$ , respectively. These values result then in  $Stk_K = [110, 510]$ , and size ratios  $\ell/\eta_K = [44, 95]$ . This suggests that the fibers are large and highly inertial, and hence, should

filter out the flow fluctuations [98, 99, 89, 80, 90, 83]. We therefore have to correct our previous Stokes number estimation as the relevant time scale is not given by  $\tau_K$ , but rather by the time scale  $\tau_\ell$  of turbulent eddies comparable to the fiber size.  $\tau_\ell = (\ell^2/\epsilon)^{1/3}$  [105], resulting in  $\text{Stk}_\ell \equiv \tau_v/\tau_\ell = [9, 24]$ .  $\text{Stk}_\ell$ , though, assumes that the particles have a tiny Reynolds numbers. Based on the liquid velocity fluctuations [98], we calculate the particle Reynolds number  $\text{Re}_p = \sigma(u_\theta)\ell/\nu = \mathcal{O}(10^3)$ , with  $\sigma$  the standard deviation, which far exceeds the viscous flow limit. Based on these insights, we use a modified viscous time scale [106, 104] for the particle  $\tau_p$ , which also takes into account the drag coefficient  $C_D(\text{Re}_p)$ . Remarkably, the resulting Stokes number  $\text{Stk}_p \equiv \tau_p/\tau_\ell = [2, 3]$ , indicating that the fibers are only slightly inertial, which explains why they follow the flow field (at their length scale) quite accurately.

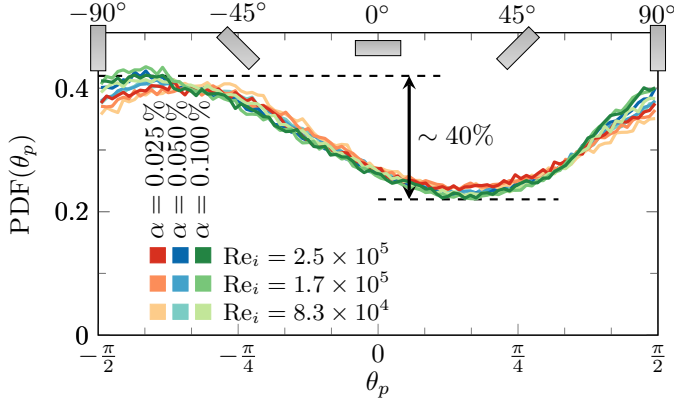


Figure 2.3: PDF of the fiber orientation  $\theta_p$  measured at  $\tilde{z} = 0.24$ . Different  $\alpha$  are indicated by different hues and different  $\text{Re}_i$  are shown with different shades. A representation of the fiber alignment is shown at the top of the figure. Independent of  $\alpha$  and  $\text{Re}_i$  there is a clear preference for an alignment around  $-0.38\pi \pm 0.05\pi$  ( $-68 \pm 9^\circ$ ). A large 40 % difference between the most and least probable orientation is observed.

Next, we address the orientation statistics of the fibers in the flow. To check whether or not the fibers show any preferential alignment, we first look at the probability density function (PDF) of the orientation (see figure 2.1D for definition) for various  $\alpha$  and  $\text{Re}_i$ , see figure 2.3. We find that for all cases studied, the PDF of the orientation shows a preference for  $\theta_p = -0.38\pi \pm 0.05\pi$  ( $-68 \pm 9^\circ$ ). Since Taylor–Couette flow [9] is known to have (turbulent) Taylor vortices [69, 107] (Relative positions shown in the

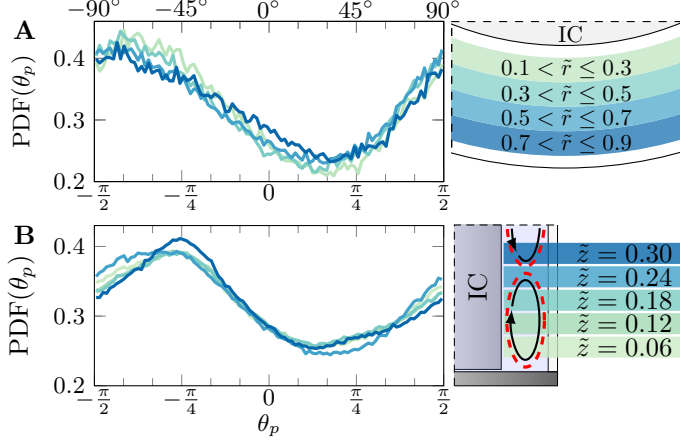


Figure 2.4: (A) PDF of the fiber orientation  $\theta_p$  at various radial bins, indicated by different colors.  $\alpha$  is fixed to 0.05 %,  $Re_i = 2.5 \times 10^5$ , and the measurement is performed at  $\tilde{z} = 0.24$ . (B) Axial dependence of the PDF of  $\theta_p$ , indicated by different colors. For these measurements  $\alpha = 0.05$  % and  $Re_i = 8.3 \times 10^4$ . The diagram on the right indicates the position of the weak vortical structures [69, 107]. The distribution is found to be nearly independent of the radius and the axial position and all show similar alignment.

right diagram of figure 2.4B), one might expect this preferential alignment to depend on the axial ( $\tilde{z} = z/L$ ) and radial ( $\tilde{r} = (r - r_i)/d$ ) positions of the fibers. We therefore provide PDFs conditioned on  $\tilde{r}$ , and perform additional measurements at several  $\tilde{z}$ , see figure 2.4. Surprisingly, the preferential alignment around  $\approx -0.38\pi$  persists throughout the flow. We find nearly identical orientation PDFs for different  $Re_i$  and  $\alpha$ , and even at different  $\tilde{r}$  and  $\tilde{z}$ . This striking universality is remarkable for such large particles in a flow with strong flow anisotropies.

In order to understand the preferential alignment of the fibers, we model their dynamics using a simplified model based on the equations by Jeffery [85], derived for ellipsoidal particles in a viscous fluid in the limit of small Stk and small  $Re_p$ . Jeffery's equations in the non-inertial limit are duplicated here:

$$\dot{p}_i = \Omega_{ij} p_j + \frac{\Lambda^2 - 1}{\Lambda^2 + 1} (S_{ij} p_j - p_i p_k S_{kl} p_l) \quad (2.1)$$

where  $p_i$  is the orientation vector (see figure 2.1D),  $\Omega_{ij}$  is the vorticity tensor  $\Omega_{ij} = \frac{1}{2} \left( \frac{\partial u_i}{\partial x_j} - \frac{\partial u_j}{\partial x_i} \right) = -\epsilon_{ijk} \omega_k$ , where  $\epsilon_{ijk}$  is the Levi-Civita symbol in 3D,

$\omega_k$  is the vorticity vector,  $\Lambda$  is the aspect ratio of the particle, and  $S_{ij}$  is the strain-rate tensor  $S_{ij} = \frac{1}{2} \left( \frac{\partial u_i}{\partial x_j} + \frac{\partial u_j}{\partial x_i} \right)$ . We model a stochastic mean field process by assuming that the fibers are initially randomly oriented by the turbulent fluctuations every time interval  $\sim \mathcal{O}(\tau_\ell)$ . Next, we model the flow seen by the fiber as a simple shear flow, with a mean shear rate equal to that in the bulk of the turbulent Taylor–Couette flow, i.e.  $\dot{\gamma} = \langle \partial u_\theta / \partial r \rangle_{\tilde{r} \in [0.25, 0.75]}$  from figure 2.2. We integrate eqs. 2.1 for all initial conditions  $p_i(t = 0) = \sin\left(\frac{\pi i}{2} - \theta\right)$  for  $\theta \in [-\pi/2, \pi/2]$  over a variety of time scales  $t \in [0, C\tau_\ell]$  where  $C$  is a dimensionless constant of  $\mathcal{O}(1)$ , to obtain  $p_i(t)$  for every initial condition. These evolutions of  $p_i(t)$  are converted to  $\theta(t)$  using the definition given in figure 2.1D, aggregated, and binned to calculate the PDF of  $\theta$ , see figure 2.5. The PDF shape predicted by this simplified model is similar to our experimental observations. The preferred orientation (peak) calculated from Jeffery’s equation is approximately  $-0.27\pi$  ( $\approx 50^\circ$ ), which is close to the measured value of  $-0.38\pi$  ( $68^\circ$ ). The amplitude of the measured PDF is close to the calculation with the integration time being  $2\tau_\ell$ , which measures the time scale of rotation of a non-inertial fiber in the bulk of the flow. The non-inertial approach for orientation modeling is reasonable, since typically the rotational Stokes number  $\text{Stk}_r \sim \mathcal{O}(0.1 \text{ Stk}_p)$  for long prolate ellipsoids [93]. Nevertheless, slight differences between the calculation and experimental results (seen in figure 2.5) are expected, since our fibers are not truly in the  $\text{Stk}_r \rightarrow 0$  limit [108].

The PDF of the fiber rotation rate at different  $\text{Re}_i$  is shown in figure 2.6

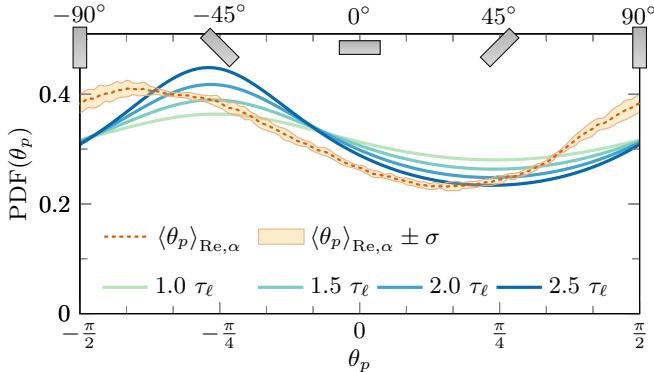


Figure 2.5: Averaged PDF of the experimentally found fiber orientation (dashed) compared to the alignment found from integrating Jeffery’s equations (solid lines). The legend indicates the integration time scale as multiples of  $\tau_\ell$ .

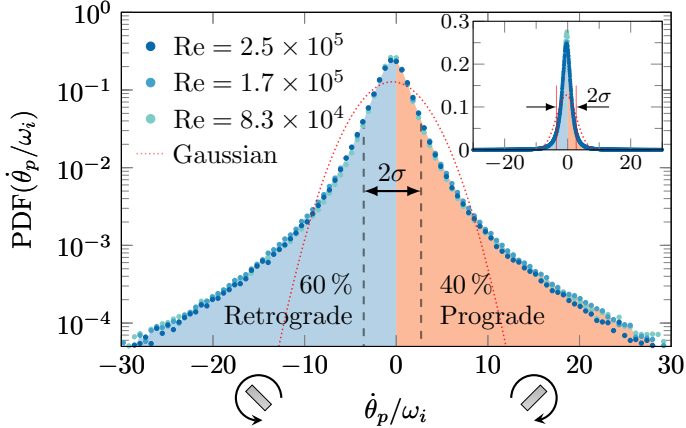


Figure 2.6: PDF of the rotation rate of the fibers for  $\alpha = 0.05\%$  and  $z/L = 0.24$ . Rotational velocities are normalized using the angular velocity of the IC. The PDF is independent of  $Re_i$  and shows a slight preference for retrograde rotation (blue). Note that the icons holds for CW rotation of the inner cylinder. The mean rotation is  $\langle \dot{\theta}_p/\omega_i \rangle \approx -0.42$  with a standard deviation of  $\sigma(\dot{\theta}_p/\omega_i) = 3.13$ , which reveals that a large number of fibers rotates much faster than the inner cylinder. For comparison, a Gaussian distribution with the same mean and variance is added. The skewness and kurtosis are found to lie in the range  $[-0.14, 0.24]$  and  $[34, 40]$ , respectively. The inset shows the same data on a linear scale.

(The inset shows the same data on linear scale). The PDF of the normalized rotation rate is found to be independent of the Reynolds number. Due to the mean shear in the bulk of the flow, it has a slight preference for retrograde rotation (rotation in the opposite direction of the IC) with 60% probability. We notice that the peak of the PDF is located at  $\langle \dot{\theta}_p/\omega_i \rangle \approx -0.42$ , which is comparable to the mean vorticity in the bulk of the flow. The standard deviation is  $\sigma(\dot{\theta}_p/\omega_i) = 3.13$ , which reveals that a large number of fibers rotate much faster than the inner cylinder. What is really remarkable is the strong intermittency of the PDF with tails extending beyond  $\pm 30\omega_i$ , which occurs despite the large size of the fibers. We find a skewness of the angular velocity between  $[-0.14, 0.24]$ . The kurtosis of the angular velocity lies in the range  $[34, 40]$ , which is much larger than the kurtosis of spheres of similar size ratios [109, 110, 111]. This can be attributed to the fact that for elongated ellipsoids the rotational inertia is typically much lower than the rotational inertia of similar-sized spheres [93]. Furthermore, the length of the fibers is of  $\mathcal{O}(100\eta_K)$ , the two ends of the fibers can therefore experience extremely high instantaneous velocity differences due to the intermittent

nature of the turbulent velocity fluctuations. These instantaneous velocity differences can create high torques on the fiber, resulting in violent rotational intermittency.

## 2.3 Summary

To summarize, we report on the statistics of translation and rotation of finite-sized fibers in a strongly sheared turbulent flow. The fibers tend to follow the flow almost perfectly, despite their large size. This adherence to the flow can be explained by considering the turbulent dynamic time at the scale of the fiber, compensated by effects of non-linear drag at the finite Reynolds number of the fiber, yielding a Stokes number estimate that is just above unity. For the fiber orientation statistics, while it was often hypothesized that no systematic alignment would be possible in such highly turbulent flows, in this canonical TC flow geometry, we show that fibers do align with an angle of  $-0.38\pi \pm 0.05\pi$  ( $-68 \pm 9^\circ$ ) with respect to the IC wall. The difference between the most and least preferred alignment is dramatic, namely 40 %. This alignment is universal for all tested Reynolds numbers ( $Re_i$ ), fiber volume fractions ( $\alpha$ ), and spatial coordinates. We model the fiber orientation statistics using Jeffery's equations, which provides a fair estimate of the shape of the alignment PDFs. Additionally, it is found that the fiber angular velocity shows extremely high intermittency with instantaneous rotation rates much larger than that of the rotating cylinder. Thus, in a number of ways, finite-sized (millimetric) fibers behave remarkably similar to tiny particles in turbulence [83, 13], extending the applicability of the point-particle approach to model large anisotropic particles in turbulence.

# 3

## Dramatic change in drag by catastrophic phase inversion<sup>©</sup>

---

In this letter we investigate oil-water mixtures in highly turbulent Taylor–Couette flow. In the absence of an emulsifier, energy-input from the turbulence provides the energy to continuously break-up droplets, such that the phases do not separate. We show how a mixture of oil and water can have effective viscosities larger or smaller than each species. In addition, we report on the catastrophic phase-inversion of these mixtures, with its concomitant drop in effective viscosity. We find that for a fixed oil fraction we can have either a water-in-oil or oil-in-water mixture with vastly different droplet sizes and rheological properties. The manifestation of these states is exemplified by providing combined local and global measurements of highly turbulent oil-water mixtures in the Twente Turbulent Taylor–Couette facility, including in-situ microscopy imaging. We explain our findings due to the different nature of droplet size distributions and associated deformability. Our findings demonstrate that using an optimal mix of two immiscible fluids can lead to drastic energy reductions while exceeding this optimum will lead to the opposite.

---

©Based on: Dennis Bakhuys, Rodrigo Ezeta, Pim A. Bullee, Sander G. Huisman, Alvaro Marin, Detlef Lohse, and Chao Sun *Dramatic change in drag by catastrophic phase inversion*, manuscript in preparation.

### 3.1 Introduction

Mixtures of oil and water are omnipresent in petro-chemical processes, biological systems, as well as in the food industry. For oil recovery, for example, water is generally used as a carrier liquid to extract oil from the ground creating an emulsion. In food industry emulsions are generally found in all sorts of products together with stabilizers [112]. Due to their polar and non-polar nature, water and oil are immiscible. Although by definition immiscible fluids cannot be mixed, they can be dispersed into each other by vigorously shaking or stirring. One phase is typically fragmented in the form of drops (becoming the dispersed or internal phase) and suspended inside the other fluid (i.e. the continuous or external phase), thereby, creating an emulsion. Emulsions can be categorized in two morphologies types: simple emulsions and multiple emulsions [113]. Simple emulsions are oil droplets suspended in water ( $o-w$ ) or water droplets suspended in oil ( $w-o$ ). An emulsion can become easily unstable, typically by coalescence of the disperse phase as a result, the two phases completely separate. Depending on the application, emulsifiers (surfactants and/or polymers) can be added to gain stability against coalescence. As the dispersed phase volume fraction is increased, a phase inversion might occur in which dispersed and continuous phases switch roles [114, 115]. There are various attempts to model the phase inversion: continuous drops trapped in multiple emulsions [116, 117], minimal dissipation model [118, 119], energy barrier model [120], or a coalescence/breakup model [121, 122]. A phase inversion process can occur at very different time scales: it can take up to days when it occurs due to gravitational effects (sedimentation or flotation of the dispersed phase), or it can occur instantaneously. The latter scenario is typically called a *catastrophic phase inversion* [123, 124, 125]. The critical inversion point of  $o-w$  and  $w-o$  are generally not at the same oil volume fraction and hysteresis is observed [121, 122, 126, 127]. It was found that width of the hysteresis region, also known as the ambivalence region, is a unique property of the emulsion mixture and independent of Reynolds, Froud, and Weber number [120]. The break-up of droplets in a turbulent flow was pioneered by Kolmogorov [128] and Hinze [129]. Their focus was to determine a correlation between the flow scales and the average droplet diameter by dimensional analysis. Turbulent eddies with a scale similar to the droplet can destabilize the interfaces, leading to the break-up of droplets [130]. While the smallest

scale in a turbulent flow, i.e. the Kolmogorov scale  $\eta_K$ , was hypothesized as the lower bound for the droplet diameter, a large portion of droplets can have a smaller size [131]. At these scales (viscous subrange), subeddy viscous stresses dominate over inertial stresses, making smaller droplets possible [132, 133]. In a turbulent flow, without any surfactant or emulsifier, a dynamic equilibrium emerges: the energy-input of the turbulence continuously provides energy to break up droplets, while the droplets continuously merge and coalesce. Stopping the energy input quickly destroys the equilibrium and the phases separate. Adding inclusions such as solids, gas or immiscible fluids to a liquid can dramatically change its rheology [134, 41]. Solids generally increase the effective viscosity [101], while small amounts of polymers [32], oil without surfactant [116], or gas [52, 66] are known to reduce drag, yielding a lower effective viscosity as the original liquid phase. For the case of air-lubrication, the current understanding suggests [66, 52, 2] that the requirement for large drag reduction is the deformability (expressed as the Weber number) of the gas phase.

## 3.2 Experiments and results

In this chapter we investigate the dynamic phase stability of a meta-stable emulsion without surfactants, in a highly turbulent shear flow. For doing so, we measure the effective viscosity effective viscosity  $\nu_{\text{eff}}$  of the turbulent emulsion. Viscosities of meta-stable emulsions (MSE) can not be easily measured in the laminar regime, as the phases would quickly separate. To keep the MSE mixed, a turbulent flow is required. Unfortunately, conventional rheometers work in predictable flow regimes and therefore they can only operate in the laminar regime. Recent advances [9] in turbulent Taylor–Couette (TC) flows makes it possible to use this geometry as a rheometer—classically solely used in the laminar regime—even in the turbulent regime. For all measurements we make use of the Twente Turbulent Taylor–Couette ( $T^3C$ ) facility [63], as this provides local and global measurement access in a controlled and closed geometry (schematic shown in figure 3.1A). The apparatus has an inner cylinder (IC) radius  $r_{\text{ic}} = 200 \text{ mm}$ , an outer cylinder (OC) radius of  $r_{\text{oc}} = 279.4 \text{ mm}$ , and a height of  $L = 927 \text{ mm}$ , resulting in a gap width  $d = 79.4 \text{ mm}$ , a radius ratio of  $\eta = r_{\text{ic}}/r_{\text{oc}} = 0.716$ , and an aspect ratio  $\Gamma = L/d = 11.7$ . The torque,  $\mathcal{T}$ ,

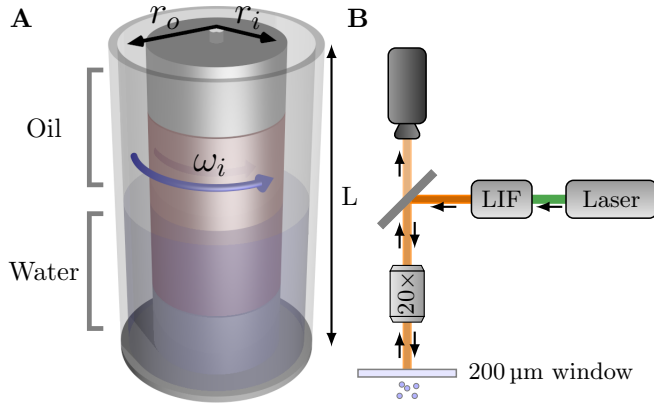


Figure 3.1: A. Schematic of the T<sup>3</sup>C setup. Initially, the water (bottom) and oil (top) are separated. B. In-situ high-speed microscopy using LIF lighting, a half-mirror, and a 20× magnification lens, through a 200  $\mu\text{m}$  thick window at the top of the setup shown in A.

required to rotate the IC at constant angular velocity  $\omega_{\text{ic}}$  is measured using a hollow reaction torque sensor, while the temperature is kept at  $21.0 \pm 0.5^\circ\text{C}$ . Optical access to the flow is through a window on top of the system, modified to hold a 200  $\mu\text{m}$  glass plate, thereby, allowing to operate a microscopy system (shown in figure 3.1B). The microscopy system consists of laser-induced fluorescence lighting (LIF), a half-mirror, 20× magnification lens, and two cameras: Lumenera LM165 and Photron SA-Z. We make use of demineralised water and a low-viscosity silicone oil [135] with  $\nu_o = 1.03 \text{ mm}^2 \text{ s}^{-1}$  at  $25^\circ\text{C}$  and an interfacial tension with water of  $\gamma = 42.7 \text{ mN m}^{-1}$  [136].

The driving of TC flow can be characterized by the Taylor number [12]:

$$\text{Ta} = \frac{1}{4}\sigma d^2(r_{\text{ic}} + r_{\text{oc}})^2(\omega_{\text{ic}} - \omega_{\text{oc}})^2/\nu^2 \quad (3.1)$$

where  $\sigma = ((1+\eta)/(2\sqrt{\eta}))^4$  is a geometric constant. The output of the system, the torque, can then be captured as a  $\omega$ -Nusselt number:

$$\text{Nu}_\omega \equiv \frac{J_\omega}{J_\omega^{\text{lam}}} = \frac{\mathcal{T}}{2\pi L\rho J_\omega^{\text{lam}}}. \quad (3.2)$$

Here  $J_\omega^{\text{lam}} = 2\nu r_{\text{ic}}^2 r_{\text{oc}}^2 (\omega_{\text{ic}} - \omega_{\text{oc}})/(r_{\text{oc}}^2 - r_{\text{ic}}^2)$  is the angular velocity transport for laminar, non-vortical flow and the angular velocity of the OC is  $\omega_{\text{oc}} = 0$ .

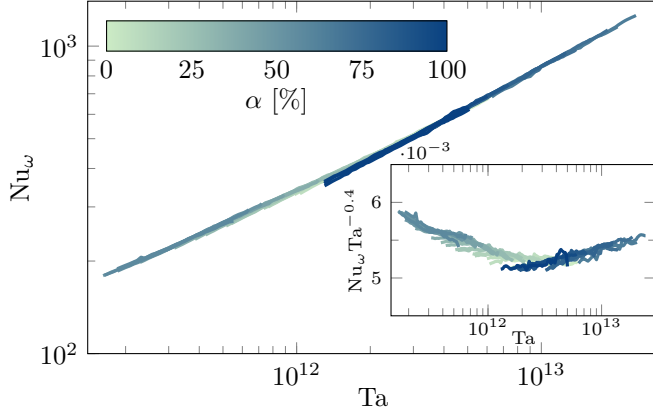


Figure 3.2: Exploiting the relation between  $\text{Nu}_\omega = f(\text{Ta})$ , a  $\nu_{\text{eff}}$  was found such that 32 datasets share a single curve, by minimizing  $\sigma(\text{Nu}_\omega)$  for the collective data, binned in  $\text{Ta}$ . The result of this minimization is shown as the closest to a single curve for all sets, for  $\text{Nu}_\omega$ . The inset shows the same datasets, compensated using  $\text{Ta}^{0.4}$ , revealing the overlap within a couple of percent.

From previous studies [137, 62, 102, 138, 69, 9] we know that  $\text{Nu}_\omega = f(\text{Ta}, \eta, \omega_{\text{ic}}/\omega_{\text{oc}})$ . In order to compute an effective viscosity for the MSE, we will assume that it responds as a Newtonian liquid at these shear rates. While quasi-statically driving the inner cylinder for  $\omega_{\text{ic}}/(2\pi) = 4\text{--}20\text{ Hz}$ ,  $\mathcal{T}$  was measured for various oil volume fractions  $\alpha = V_o/(V_o + V_w)$ , where  $V_o(V_w)$  is the volume of the oil(water) phase. Experiments based on liquids with known viscosity defines the curve  $\text{Nu}_\omega = f(\text{Ta})$  for our geometry, which we do so using the  $\alpha = 0\%$  and  $\alpha = 100\%$  cases and exploiting the known scaling [60, 137, 62]. This scaling in the ultimate regime,  $\text{Nu}_\omega = f(\text{Ta})$ , can now be exploited to determine  $\nu_{\text{eff}}(\alpha)$  such as to collapse all the data on to a single curve, see the collapsed data of 32 experiments in figure 3.2. All datasets collapse onto a single universal curve, consistent with previous studies on Newtonian liquids [60, 137, 138]. To appreciate the quality of the collapse, all data is compensated by  $\text{Ta}^{0.4}$  (inset of figure 3.2), which shows that all datasets have an error of 1.2 % and justifies the Newtonian assumption made earlier for the MSE at such large shear rates.

The effective viscosity  $\nu_{\text{eff}}(\alpha)$ , normalized using the viscosity of water  $\nu_w$  (all at 21 °C) are shown in figure 3.3 as blue circles. Each experimental measurement in this set is performed at constant oil fraction  $\alpha$ , and therefore

is depicted as *static*  $\alpha$  in the plot. Remarkably, we observe two disconnected branches, the left branch for  $\alpha \leq 65\%$ , and the right branch for  $\alpha \geq 70\%$ . Starting from pure water, adding oil (Ⓐ) increases the effective viscosity beyond the viscosities of each of the constituents, making the fluid three times as viscous for  $\alpha = 65\%$ . Further increasing  $\alpha$  in excess of 65% results in a dramatic drop in  $\nu_{\text{eff}}$ . This is caused by a phase inversion; whereas for  $\alpha \leq 65\%$  we had o-w, for  $\alpha \geq 70\%$  we have w-o, showing a tremendous change in rheology. When starting from pure oil, adding water (Ⓑ) lowers the effective viscosity, and thereby, resulting in drag reduction. For  $\alpha = 70\%$ , the torque is 13% lower as for pure oil, similar to other w-o emulsions [116]. For the present regime of  $\text{Ta} = \mathcal{O}(10^{11}-10^{13})$ , one can derive that  $T_o/T_w \propto (\nu_o/\nu_w)^{0.2}$ , and from this we, indeed, find a  $\nu_{\text{eff}}$  approximately half the value of pure oil for  $\alpha = 70\%$ . At phase inversion,  $\nu_{\text{eff}}$  decreases (or increases) by a factor 6, resulting in a tremendous change of more than 40% in torque. To further investigate what is happening at phase inversion we now quasi-statically increase  $\alpha$  by slowly draining the setup at the bottom while filling it with oil from the top, see the red curves( $d\alpha/dt > 0$ ) in figure 3.3. For all of these *dynamic* experiments,  $\omega_{\text{ic}}/(2\pi)$  was fixed to 17.5 Hz and the mass of the injected liquid was recorded. The instantaneous value of  $\alpha$  is obtained taking into account the injected liquid and assuming that the liquid drained is an homogeneous mixed emulsion. At the end of the experiment,  $\alpha$  was directly measured and found to be within 1% of the calculated value. Here, we observe a displaced *catastrophic* phase inversion at  $\alpha = 72\%$  (Ⓒ), exceeding  $\alpha$  from the *static* measurements. The reversed experiment, slowly decreasing  $\alpha$  by filling the system with water and draining the mixed emulsion, results in the opposite *catastrophic* phase-inversion, see the blue curves ( $d\alpha/dt < 0$ ) in figure 3.3. The torque measured by the inner cylinder sharply increases with more than 35%, switching from drag reduction to a severe drag increase slightly around  $\alpha = 50\%$ . What is striking is that the change in morphology at Ⓑ and Ⓒ happens instantaneously. The dispersed phase exceeds the critical amount and triggers a phase inversion resulting in a very different rheology of the MSE. The effects are instantly visible in the measured torque of the system, but also in the temperature, as the active cooling of the setup needs immediate adjustments. Repeating the *dynamic* measurements, indicated by shaded colors in figure 3.3, we observe that the critical  $\alpha$  (amount of dispersed phase required to get phase inversion) is very reproducible. Note that the volume fraction for the transition from w-o to o-w (Ⓓ) is distinctly

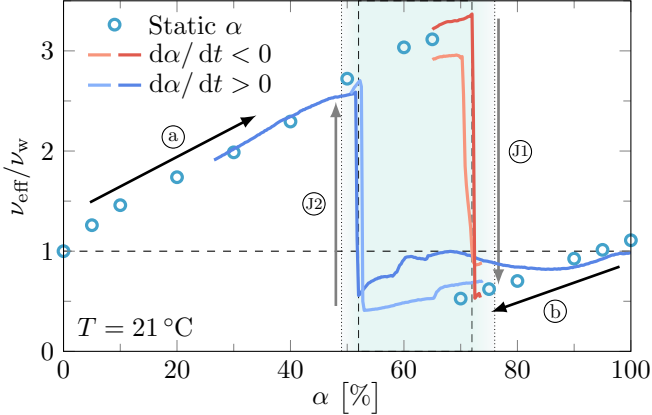


Figure 3.3: Effective viscosity normalized by the viscosity of water as function of oil volume fraction. The static measurements where the fluid is premixed are shown by circles. The continuous measurements, for which  $\alpha$  is changed during the experiments ( $\omega_{ic}/(2\pi)$  is fixed at 17.5 Hz), are shown solid lines. The shade area shows the ambivalence area, bounded by two catastrophic phase inversion, (J1): w-o  $\rightarrow$  o-w and (J2): o-w  $\rightarrow$  w-o. When water is the continuous phase, increasing  $\alpha$  leads to an increase in  $\nu_{\text{eff}}$  (a), while for oil, increasing the water fraction, decreases  $\nu_{\text{eff}}$  (b). When  $\omega_{ic}$  is decreased, the ambivalence region increases in width (indicated by dashed to dotted boundary).

different from the o-w to w-o (J1) case. Here, the MSE shows a hysteretic morphology, in the an ambivalence region,  $52\% \leq \alpha \leq 72\%$  (shaded blue area shown in figure 3.3), even for such high Reynolds numbers of  $\mathcal{O}(10^6)$ . One would naively think that for such a high Reynolds number the system provides ample power to trigger any instability, however it has been shown before that turbulent TC flow is susceptible to hysteresis [69, 107]. Also noteworthy is that in the ambivalence region, each morphology can have multiple values for  $\nu_{\text{eff}}$  as there is some discrepancy between the repeated measurements. We expect the distribution of droplet sizes differ slightly between the measurements which can have a large impact on the rheology [139]. Catastrophic phase inversion has been also observed in turbulent pipe flows [126, 140], in which the width of the ambivalence region is solely dependent on the ratio of the dispersed phase injection rate and the total flow rate. In our case, we have a dispersed phase injection rate of approximately  $12.5 \text{ mL s}^{-1}$ , which can either be water or oil. We do, however, observe that the ambivalence region gets slightly wider when  $T_a$  is decreased (illustrated from dashed to dotted boundaries in figure 3.3). The

ambivalence region increases by a couple percent on both sides, thereby displacing the phase inversion for each morphology. The different response seen on the left and right branches in Figure 3.3 demands a detailed look of the flow. The decrease in  $\nu_{\text{eff}}$  for w-o emulsions (⑤) could be a similar process as in bubble drag reduction [48, 66], related with the deformability of the dispersed phase, for which large droplets are required. Using the same reasoning, an increasing  $\nu_{\text{eff}}$  (⑥) should be connected with the presence of small and non-deformable droplets which would act as solid-like particles and therefore increase  $\nu_{\text{eff}}$  [41, 101]. Consequently, we could explain the observed changes in viscosity by analyzing the droplet distribution. However, due to the metastable nature of the mixture, the emulsion quickly separates when energy is not supplied, and therefore we cannot guarantee that samples taken from the system and analyzed under a standard microscope have the same morphology as those flowing in the system at high energy. Consequently, we choose for bringing the microscope to our apparatus and size the dispersed phase while flowing. The optical system arranged is shown in figure 3.1B. Note that the dispersed droplets are visualized by the reflected light from their interface and that no fluorescent dye was employed. The MSE was premixed (*static*) at  $\alpha = 60\%$  and the IC was fixed to an angular velocity  $\omega_{\text{ic}}/(2\pi) = 8\text{ Hz}$ . For this  $\alpha$ , we are approximately in the middle of the ambivalence region (see in Fig.3.3) and consequently viscosity is multivalued: the system can either flow at the lower viscosity branch ( $\nu_{\text{eff}} \approx 0.5\nu_w$  for o-w) or at the higher viscosity branch ( $\nu_{\text{eff}} \approx 3\nu_w$  for w-o). Interestingly, to get the system to flow at the upper branch (w-o, larger  $\nu_{\text{eff}}$ ) we need a slow transient until the IC achieves its chosen angular velocity, in this particular case the acceleration period took approximately two hours. Figure. 3.4A shows the captured high-speed images of the o-w state. A large amount of tiny droplets is identified in each captured frame. The observed rings visible in the droplet images could be due to light diffraction (as the droplets are only a couple of microns in diameter), or due to the presence of a double emulsion (which has been also observed in Turbulent catastrophic inversion regimes [140]). Using a larger acceleration rate (a few minutes start-up time), results in  $\nu_{\text{eff}}$  being in the lower branch, which results in a lower torque value compared to the single phase case. From the typical image shown in figure 3.4B it is already evident that for w-o, the droplets are considerably larger. The deformability is also obviously affected: o-w droplets are mostly spherical while the w-o droplets are commonly seen with larger degree of deformation. To characterize the droplet size distribution we

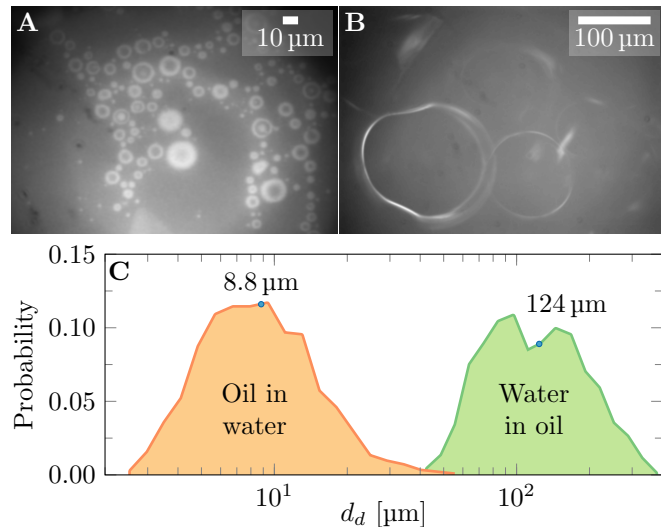


Figure 3.4: A. In-situ microscopic image taken of an o-w suspension of  $\alpha = 60\%$  in operation at  $\omega_{ic}/(2\pi) = 8\text{ Hz}$ . B. In-situ microscopic image taken of an w-o suspension operating at the same  $\alpha$  and  $\omega_{ic}$  as A. C. Probability distributions of the typical diameter of oil drops (in water) and water drops (in oil) for the cases shown in A and B. Statistics based on  $\mathcal{O}(10^3)$  samples, mean values are indicated above the curves.

collected  $\mathcal{O}(10^3)$  samples for each type (o-w and w-o) and calculated the probability distribution shown in figure 3.4C. Water droplets are roughly  $14\times$  larger in diameter as compared to oil drops—a staggering  $2800\times$  larger in volume. Using  $d_d$  we calculate the Weber number,  $We = \rho u'^2 d_d / \gamma$ , where  $\rho$  is the density of the mixture and  $u'$  velocity fluctuations. The Weber number of the o-w MSE is  $We_{o-w} = 0.01$ , while for the w-o case this is more than an order of magnitude larger,  $We_{w-o} = 0.16$  but still below unity, a requirement found for bubble drag reduction [48, 66]. The size of the droplets are linked to the underlying flow structures and a first guess is generally the Kolmogorov length scale:  $\eta_K = (\nu_{\text{eff}}^3/\epsilon)^{1/4}$ , where  $\epsilon$  is the turbulent energy dissipation. From this relation we find  $46\text{ }\mu\text{m}$  and  $13\text{ }\mu\text{m}$  for the o-w and w-o case respectively. These values are both quite off, but this relation does not take into account interfacial tensions and assumes homogeneous isotropic turbulence. The scaling from Hinze [129] does take into account the interfacial tensions:

$$d_{d,\max} \approx 0.725 (\rho/\gamma)^{-3/5} \epsilon^{-2/5}. \quad (3.3)$$

Unfortunately, using the Hinze relation straight away, results in overestimated droplets, with dimensions above a millimeter. We can however, use this relation to calculate  $\epsilon$  required to find a similar size of droplets, which showed that  $\epsilon$  should be at least  $\mathcal{O}(10^2)$  times larger. The dissipation of turbulent energy is much larger close to the boundaries as compared to the bulk. In simulations at a slightly lower Ta,  $\epsilon$  was found to be approximately  $350\times$  larger than in the bulk [141]. It is therefore plausible that close to boundaries,  $\epsilon$  is large enough and this would infer that these droplets are mostly generated at these boundaries. However, since such an argument is based solely on surface energies, it should be symmetric, i.e. applicable both for o-w and for w-o droplets identically. We therefore cannot explain such a large asymmetry in droplet sizes between branches. We speculate that the origin of the asymmetry could be found in the existence of electrical double layers when the continuous medium is polar and conductive (o-w) [142, 143]. The presence of certain interfacial electrical charges at the o-w emulsion would hinder coalescence and facilitate break-up. Consequently, the addition of salt to the water phase can be a method to alter drastically the dynamics of the system, opening ways to test this hypothesis in the future.

### 3.3 Summary

To summarize, in this work we have studied the flow of meta-stable emulsions with oil volume fractions between  $\alpha = 0\text{--}100\%$  on a wall boundary in an intensely sheared rotating flow. Exploiting the known scaling of the ultimate regime of Taylor–Couette flow, an effective viscosity of the emulsion can be calculated, and thereby using the TC apparatus as a rheometer far beyond the conventional regime. With water as the continuous phase, the addition of oil droplets increases the drag of the system. Interestingly, drag is reduced when the water is injected in a continuous oil phase. At a critical volume fraction, a *catastrophic* phase inversion takes place, which dramatically changes the rheological properties. Using an in-situ optical microscopy setup, we were able to obtain droplet size distributions while flowing in the TC system. This showed that the w–o droplets are  $14\times$  larger than o–w droplets, deformable, and therefore showing a similar drag reduction mechanism as for bubbly drag reduction [48, 66]. The asymmetry found in the droplet size distribution explains the different rheological response of the system, and it is a truly surprising example of how microscopic phenomena can influence critically the macroscopic behavior of the global system. Our results demonstrate that by tweaking the volume fractions of two immiscible fluids can result in major energetic reductions. However, exceeding a critical volume fraction can turn this benefit to an energetic disaster.



# 4

## Mixed boundary thermal conditions in Rayleigh-Bénard convection<sup>2</sup>

---

A series of direct numerical simulations of Rayleigh-Bénard convection, the flow in a fluid layer heated from below and cooled from above, were conducted to investigate the effect of mixed insulating and conducting boundary conditions on convective flows. Rayleigh numbers between  $\text{Ra} = 10^7$  and  $\text{Ra} = 10^9$  were considered, for Prandtl numbers  $\text{Pr} = 1$  and  $\text{Pr} = 10$ . The bottom plate was divided into patterns of conducting and insulating stripes. The size ratio between these stripes was fixed to unity and the total number of stripes was varied. Global quantities such as the heat transport and average bulk temperature and local quantities such as the temperature just below the insulating boundary wall were investigated. For the case with the top boundary divided into two halves, one conducting and one insulating, the heat transfer was found to be approximately two thirds of the fully conducting case. Increasing the pattern frequency increased the heat transfer which asymptotically approached the fully conducting case, even if only half of the surface is conducting. Fourier analysis of the temperature field revealed that the imprinted pattern of the plates is diffused in the thermal boundary layers, and cannot be detected in the bulk. With conducting-insulating patterns on both plates, the trends previously described were similar, however, the half-and-half division led to a heat transfer of about a half of the fully conducting case instead of two-thirds. The effect of the ratio of conducting and insulating areas was also analyzed, and it was found that even for systems with a top plate with only 25% conducting surface, heat-transport of 60% of the fully conducting case can be seen.

---

<sup>2</sup>Based on: Dennis Bakhuys, Rodolfo Ostilla-Mónico, Erwin P. van der Poel, Roberto Verzicco, and Detlef Lohse *Mixed insulating and conducting thermal boundary conditions in Rayleigh-Bénard convection*, J. Fluid Mech. **835**, 491–511 (2018).

## 4.1 Introduction

Natural convection is a common and important phenomenon which is omnipresent in Nature. It leads to the transfer of internal energy, within an unstably stratified fluid layer, via a buoyancy induced flow. Ocean currents, which are driven by gradients in density and salinity [144, 145], and the mantle convection inside the Earth, which drives the plate tectonics and generates the geomagnetic field [146, 147], are two examples of natural convection. Even outside of our planet, at the most distant stars, convection is of tremendous importance [148, 149].

An idealized system that is commonly used to study natural convection, as it is mathematically well-defined and can be reproduced in a laboratory experiment, is Rayleigh-Bénard (RB) convection [150, 151, 10, 152]. The RB system consists of a fluid in a container, that is heated from below and cooled from above. The fluid is subject to an external gravitational field  $g$ . Apart from the geometric ones, this system has two non-dimensional control parameters, namely the Rayleigh number  $\text{Ra} = \beta g \Delta H^3 / \nu \kappa$ , which measures the strength of the thermal driving, and the Prandtl number  $\text{Pr} = \nu / \kappa$ , a property of the fluid, where  $\beta$  and  $\kappa$  are the isobaric thermal expansion and temperature diffusivity coefficients of the fluid,  $H$  the system height,  $\Delta$  the applied temperature difference between the plates, and  $\nu$  the kinematic viscosity. Depending on the geometry of the system, other control parameters such as the aspect ratio of the system,  $\Gamma = L/H$  appear, where  $L$  is a characteristic horizontal length of the system.

Above a certain critical Rayleigh number, RB flow is linearly unstable, and any perturbation will cause the onset of convection. This critical value is determined by the properties of the fluid and the boundary conditions (BC) of the RB system. If the thermal driving of the system is far above the critical  $\text{Ra}$ , the flow becomes turbulent. This dramatically increases the heat transfer with respect to the purely conductive case. Modeling this heat transfer is essential for understanding what is going on inside stars, the Earth's mantle and many other systems. RB experiments (and simulations) typically consist of a bottom and a top plate which have homogeneous boundary conditions, and lateral boundary conditions which are either periodic (simulations) to mimic laterally unconfined systems or adiabatic (experiments) to account for a lateral confinement that minimizes the heat losses.

However, these idealized systems assume that both the top and bottom

plates have perfectly homogeneous conducting surfaces while for all real physical systems, there is a certain degree of imperfection. In Nature we see such inhomogeneities; for example, the fractures in ice floes [153] or the much debated insulating effects of continents on mantle convection [154]. Other examples include convection over mixed (agricultural) vegetation and cities [155]. In engineering applications, or in RB experiments these can be small defects or dirt at the conducting plates, which could result in lower than optimal heat transport. The limiting cases of the boundary conditions are constant heat flux boundary conditions, constant temperature boundary conditions, or thermally insulating boundary conditions with no heat flux. The difference in heat transfer between the first two types of boundary conditions, Dirichlet and von Neumann, was found to be negligible at large Ra DNS [156, 157, 158], but the increase in flow strength under fixed-temperature BC cannot be neglected [159]. Accounting for a finite conductivity of the thermal sources can lead to significant reduction in the heat transport [160].

Temperature boundary conditions can also be spatially and temporally varying. A way to study imperfections is to apply sinusoidal temperature boundary conditoins on both plates to mimic plates with embedded heaters [161, 162]. These plates are locally hotter, when closer to the heater elements.

The Nusselt number is increased when the energy input into the system from the plates is periodically pulsed instead of stationary [163]. Recent experiments using insulating lids at the top boundary of a RB cell showed that with increasing insulating fraction the same amount of heat goes through a smaller cooling area[164]. Some simulations of inhomogeneous boundary conditions have also been performed. Simulations of two and three-dimensional Rayleigh-Bénard systems of mixed adiabatic-conducting boundary conditions at one plate at moderate Rayleigh numbers, with a geophysical focus, showed that the distribution of the patches caused changes in the flow configuration, the bulk temperature and the Nusselt number [165]. Defects in the form of periodic non-conducting patches were added to the top plate of a two-dimensional numerical RB system [166] to study both, the transition to turbulence of RB flow, finding a delay in this transition when defects were present, and the fully turbulent regime, finding a decrease in Nusselt number when the patch wavelength was larger than the characteristic thermal boundary layer scale.

Here, we extend the research of Ripesi *et. al.* by applying non-conducting

stripe patterns to a three-dimensional RB system. We will focus on the fully turbulent regime instead of the transition to turbulence, and consider a wider range of patterns at higher Ra, extending previous work at lower Rayleigh numbers [165]. We start by applying distributions of striped insulating patterns to the top boundary only, and study the dependence of both local and global variables, e.g. effective heat transfer and average bulk temperature, on the number of stripes. For most of the study, we keep the conducting to insulating areas equal to each other, but the effect of this ratio is also studied, which mimics the degree of imperfections and pollution on the plates. We also study the effect of applying the same pattern to both plates and the role of the pattern geometry by applying a two-dimensional checkerboard insulating-conducting pattern on the top plate. Checkerboards and stripes can be seen as the two limiting cases for the pattern geometry.

This chapter is organized as follows: First, in section 4.2 we detail the geometry and numerical method. In the next section, the results for the stripe pattern variations will be discussed where both conducting and insulating areas are kept constant. This is first done on the top plate and later the pattern is applied on both plates. A Fourier analysis was performed to study the penetration depth of the pattern imprint in the flow. In section 4.3.2 a pattern is added to both plates, in section 4.3.3, we present and discuss the results for varying the ratio of conducting to insulating surface while keeping the number of divisions constant and in section 4.3.4 we present the results for a plate with a checkerboard pattern instead of a striped pattern. The chapter is concluded by presenting the conclusions and outlook in section 4.4.

## 4.2 Numerical method

In this numerical study, we solve the incompressible Navier-Stokes equations within the Boussinesq approximation for RB. In non-dimensional form, these read:

$$\begin{aligned}\frac{D\mathbf{u}}{Dt} &= -\nabla P + \left(\frac{\text{Pr}}{\text{Ra}}\right)^{1/2} \nabla^2 \mathbf{u} + \theta \hat{z}, \\ \frac{D\theta}{Dt} &= \frac{1}{(\text{PrRa})^{1/2}} \nabla^2 \theta, \\ \nabla \cdot \mathbf{u} &= 0,\end{aligned}\tag{4.1}$$

where  $\mathbf{u}$  is the non-dimensional velocity,  $P$  is the non-dimensional pressure,  $\theta$  is the non-dimensional temperature, and  $\hat{z}$  is the unit vector pointing in the direction opposite to gravity  $g$ . For non-dimensionalization, the temperature scale is the temperature difference between the plates  $\Delta$ , the length scale their distance  $H$  and the velocity scale is the free-fall velocity  $U_f = \sqrt{g\beta\Delta H}$ .

We consider a geometry which is a horizontally doubly-periodic cuboid. The domain has horizontal periodicity lengths of  $L_x$  and  $L_y$ , and a vertical dimension  $H$ , such that  $L_x/H = L_y/H = 1$ . These variables with a tilde superscript denote their non-dimensional counterparts. The equations were discretized using an energy-conserving second-order finite-difference scheme, and a fractional time-step for time marching using a third-order low-storage Runge-Kutta scheme for the non-linear terms, and a second order Adams-Baswworth scheme for all viscous and conducting terms [167, 168]. The code was heavily parallelized to run on hundreds or even thousands of cores simultaneously and was validated many times [169, 158, 168]. Recently, the code was open-sourced and is available for download at [www.AFiD.eu](http://www.AFiD.eu).

The domain was discretized by  $n_x \times n_y \times n_z = 360 \times 360 \times 288$  grid points. In both horizontal directions, the grid was uniformly divided, and in the vertical direction the points were clustered near the top and bottom plates. A number of simulations were conducted to test the aspect ratio dependence and the grid independence. These tests did not show any significant differences in the range of Rayleigh numbers used in this study. For RB convection, a series of exact relationships which link the Nusselt number to the global kinetic energy dissipation ( $\nu \nabla^2 \mathbf{u}$ ) and the thermal dissipation ( $\kappa \nabla^2 \theta$ ) exist [170, 151], and they have been further used to check the spatial accuracy of the simulation [169]. The size of the time steps was chosen dynamically by imposing that the

Courant-Friedrichs-Lowy (CFL) number in the grid would not exceed 1.2.

The main response of the system is the Nusselt number (Nu), which is the heat transfer non-dimensionalized using the purely conductive heat transfer:

$$\text{Nu} = \frac{\langle u_z \theta \rangle_A - \kappa \partial_z \langle \theta \rangle_A}{\kappa \Delta L_z}, \quad (4.2)$$

where  $\langle \cdot \rangle_A$  indicates the average over any horizontal plane. The simulations were run between 50 and 100 large-eddy turnover times based on  $U_f$  and  $H$ . Statistical convergence is assessed by calculating differences in Nu between final and half the amount of measurement points. These are shown as error bars in the plots.

In the classical RB case, both the top and bottom plates have a homogeneous boundary condition, i.e. they are perfectly conducting. Here, we use this boundary condition only for the bottom plate, while top plate is taken to have periodic patches of insulating regions which do not contribute to the heat transfer from fluid to plate. The definition of these patches are similar to those in other work [166]:

$$\begin{aligned} \theta(\hat{x}, \hat{y}, \hat{z} = 1) &= 0 & \sin(\pi \hat{x}) \geq 0, \forall \hat{y} \\ \partial_z \theta(\hat{x}, \hat{y}, \hat{z} = 1) &= 0 & \sin(\pi \hat{x}) < 0, \forall \hat{y} \\ \theta(\hat{x}, \hat{y}, \hat{z} = 0) &= 1 & \forall \hat{x}, \hat{y}. \end{aligned} \quad (4.3)$$

Here  $L_p$  is the width of a pair of patches.  $L_{p1}$  is the width of the conducting part,  $L_{p2}$  is the insulating part, and the hat on the spatial coordinates indicates non-dimensionalizations. For most of this study we keep the insulating and conducting areas equal, i.e.  $\ell_C = 1/2$ . The BC on the top plate depends only on the  $x$ -coordinate, which results in sets of insulating and conducting stripes. The number of stripe pairs in a horizontal direction  $L$  were defined as  $f = L/L_p$ , which is a central control parameter of this study. A two-dimensional schematic is shown in figure 4.1.

There are limitations on the value of  $f$ . As each stripe has to be an integer number of grid points, only integer multiples of the grid resolution are valid. In addition, the width of all stripes summed should fit inside the system, e.g. the width in grid points should exactly be the number of grid points in the  $x$ -direction. This results in a total of 18 different pattern frequencies. For the smallest possible frequency,  $f = 1$ , we have one conducting and one insulating stripe, which both have a width of 180 grid points. The pattern with the largest frequency,  $f = 90$ , has 90 stripe pairs where each stripe has a width of

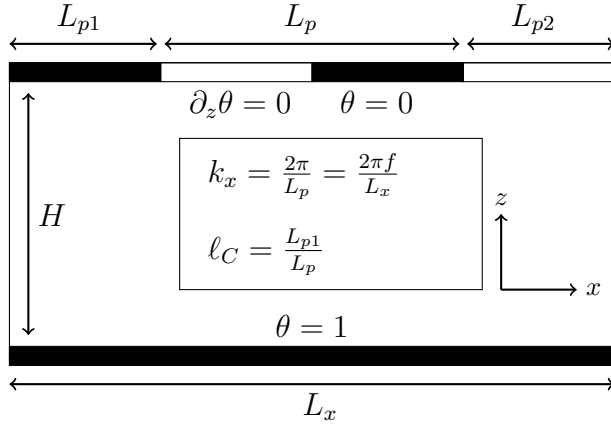


Figure 4.1: Two-dimensional  $y$ -cut of the geometry. The domain has the dimensions  $L_x \times L_y \times H$ . The bottom plate, at  $\hat{z} = 0$ , has  $\theta = 1$ . The top plate is divided into stripes of conducting ( $\theta = 0$ ) and insulating ( $\partial_z \theta = 0$ ) regions.

two grid points. In this chapter we will use the wavenumber  $k_x = (2\pi f) / L_x$ , to describe the stripe distribution.

To give an idea of how the flow in such a system looks like, two different instantaneous snapshots of the RB system with two different stripe frequencies are shown in figure 4.2. Both cases have exactly the same conducting and insulating areas, but a different stripe pattern. In section 4.3.4, we also vary the BC in  $y$ -direction, while keeping both the insulating and conducting areas equal, which results in a checkerboard pattern.

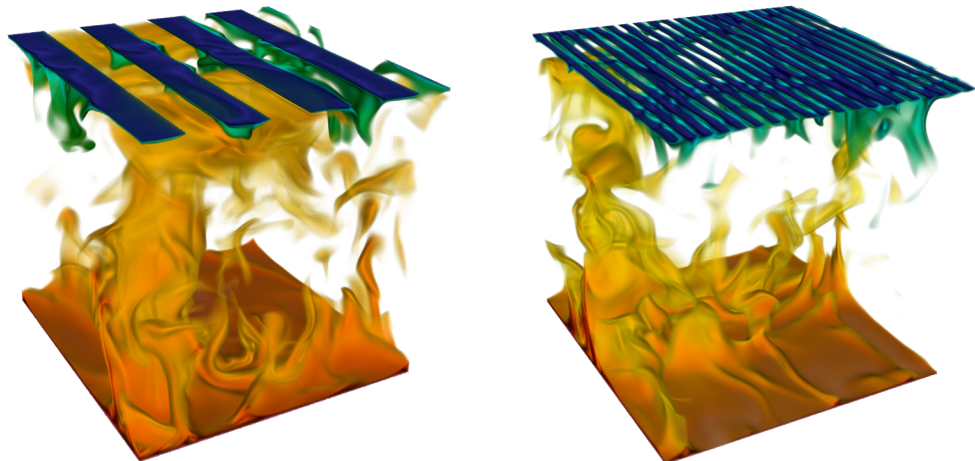


Figure 4.2: Two 3D visualizations of the instantaneous temperature field with different pattern frequencies applied to the top boundary.  $\ell_C = 0.5$ ,  $\text{Ra} = 10^8$  and  $\text{Pr} = 1$  for both cases. Only the extremes of the temperature are shown, such that hot fluid is shown in red while the cold fluid has a blue color. At the boundary, this results that the conducting regions are blue and the insulating regions transparent. The left visualization shows  $f = 4$ , four insulating stripes and four conducting stripes. The right visualization shows five times as many stripe pairs, with  $f = 20$ . Plumes of colder fluid are ejected primarily from the conducting areas for  $f = 4$  while for  $f = 20$  the plumes also eject on areas below insulating regions.

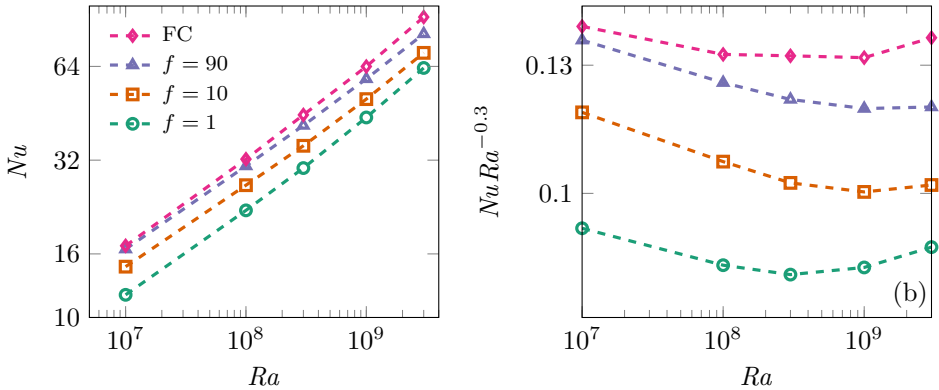


Figure 4.3: (a) Nusselt number  $Nu$  and (b) compensated Nusselt number  $NuRa^{-0.3}$  against  $Ra$  for various  $f$  and  $Pr = 1$ . The markers show the actual results while the dotted lines indicate the trend between these simulations.  $\ell_C$  was fixed to  $\ell_C = 0.5$  for all simulations.

## 4.3 Results

### 4.3.1 The effect of the number of stripes

In this subsection we present results of a series of simulations in which we varied the number of stripes while keeping  $\ell_C = 1/2$ . Four sets of cases were run for  $Ra = 10^7$ ,  $10^8$ , and  $10^9$  and  $Pr = 1$  and 10.

First we show in figure 4.3a the curves of  $Nu(Ra)$  for the fully conducting case and three striped cases with  $f = 1$ , 10, and 90. The markers show the actual results from the simulations and the dotted lines indicate the trend between the measurements. From this figure we see that the scaling does not differ significantly between all cases and all curves are almost parallel. We do see a strong dependence on the wavenumber of the pattern. For  $f = 1$ , we computed that  $Nu$  is approximately  $2/3$  of the fully conducting case. Increasing  $f$  results in a larger  $Nu$  and the values almost converge with the fully conducting case. Both the  $f = 90$  and  $f = 10$  cases are relatively closer to the fully conducting case at  $Ra = 10^7$  than at  $Ra = 3 \times 10^9$ . Our interpretation is that, due to the lower  $Ra$ , the thermal BL is thicker which

results in larger horizontal conduction of heat. As all curves have approximately the same scaling we have compensated the data using  $\text{Ra}^{-0.3}$ , which is shown in figure 4.3b. Here it is clearly visible that for low  $\text{Ra}$ , the  $f = 90$  case is almost as efficient as the fully conducting case, but the differences increase with increasing  $\text{Ra}$ . The two extreme cases,  $f = 1$  and the fully conducting case, follow a similar trend, however, the  $f = 1$  case is shifted to a lower, less efficient level. Both figures clearly show that an increase in wavenumber of the pattern results in an increase in  $\text{Nu}$ .

To make this point even more clear, we plotted  $\text{Nu}(k_x)$  in figure 4.4a. All datasets show a clear  $k_x$  dependence:  $\text{Nu}$  quite strongly increases with  $k_x$ . The gray area indicates the data points for which the width of the stripes  $L_p$  is smaller than the thermal boundary layer thickness  $\lambda_T$ , which can be estimated as  $\lambda_T = H/(2\text{Nu})$ . Ripesi et al. showed that the heat transfer monotonically increases with increasing  $k_x$  until  $L_p$  is comparable to  $\lambda_T$ . A similar trend is visible for  $\text{Ra} = 1 \times 10^7$  and  $\text{Ra} = 1 \times 10^8$  even if the  $\text{Ra} = 1 \times 10^7$  case shows minor increases in heat transfer when  $L_p$  is further decreased beyond  $\lambda_T$ . The change in  $\text{Pr}$  from  $\text{Pr} = 1$  to  $\text{Pr} = 10$  does not have a significant effect for the heat transfer, at least not for  $\text{Ra} = 10^8$ , for which the two datasets are practically overlapping. This behavior is similar to the standard Rayleigh-Bénard case, in which the  $\text{Pr}$  of  $\text{Nu}$  is also weak [151].

To perform a better comparison between the different  $\text{Ra}$ , we normalize the resulting  $\text{Nu}$  using  $\text{Nu}_{fc}$ , the Nusselt number of the fully conducting case. The normalized  $\text{Nu}$  for different stripe configurations are shown in figure 4.4b. We see the same trend for all  $\text{Ra}$  and  $\text{Pr}$ . At the lowest  $k_x$ , in which we only have a single conducting and single insulating stripe, the effective  $\text{Nu}$  is approximately two-thirds of the fully conducting case. When the number of stripes, i.e.  $k_x$ , is increased, we see that for all tested  $\text{Ra}$  and  $\text{Pr}$ , the Nusselt number slowly converges to almost the fully conducting case. So remarkably even if only half of the plate is conducting, it can be almost as effective as if the plate is fully conducting. In this compensated plot it is also clearly visible that for the largest  $k_x$  of  $\text{Ra} = 1 \times 10^7$ , for which  $L_p$  goes below the size of  $\lambda_T$ , the heat transfer is still increasing.

The differences between the different  $\text{Ra}$  are not so clear at the lowest  $k_x$ ; however, for a slight increase of  $k_x$  we see that the curves order themselves.  $\text{Ra} = 10^9$  increases slightly slower with  $k_x$  when comparing it to the  $\text{Ra} = 10^8$  case. The  $\text{Ra} = 10^7$  case increases slightly faster than the  $\text{Ra} = 10^8$  case and it ends at 99.7% of the fully conducting case for the largest number of stripes used. The explanation for this trend is the difference in boundary

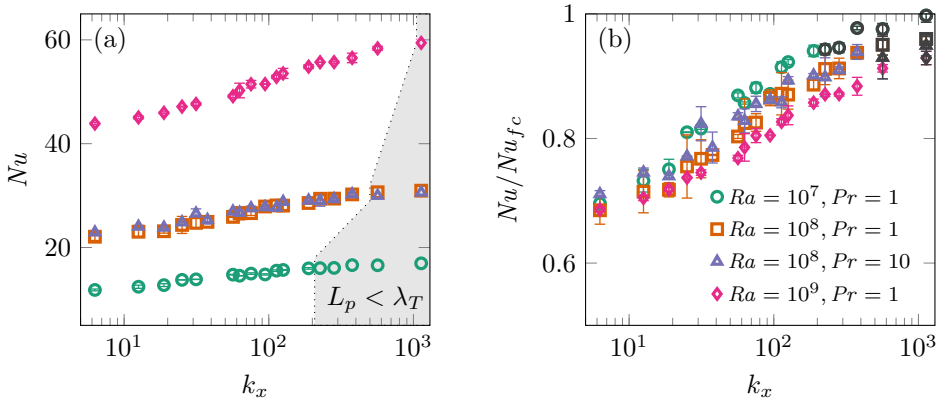


Figure 4.4: (a) Nusselt number  $Nu$  for various  $Ra$  and  $Pr$  versus pattern wavenumber  $k_x$ . The shaded area shows the data points for which the stripe width is smaller than the thermal boundary layer. (b) The same data but normalized by  $Nu_{fc}$ . The dark points are the same as in the shaded area of 4a. For both plots, the error bars shows the statistical convergence error.

layer thickness, which decreases when we increase  $Ra$ . The boundary layer controls the heat transport from the bulk to the conducting region. Below the insulating region, this heat transport must also go in the horizontal direction. By increasing  $Ra$  and thus decreasing the thickness of the boundary layer, the same amount of heat needs to be conducted through a smaller 'channel'. This explains the decreased effectiveness with increasing  $Ra$ .

In these sets of simulations, we also compare  $Pr = 10$  with  $Pr = 1$  for  $Ra = 10^8$ . The results for both  $Pr$  are quite similar. At lower  $k_x$ , we see that the  $Pr = 10$  case has only a marginally larger  $Nu$  and these differences become smaller with increasing  $k_x$  and are within the uncertainty of the simulation.

Figure 4.5a shows the average bulk temperature of the fluid plotted against the wavenumber. This average was computed over the horizontal plane at mid-height of the system. The effect is similar to what we see for  $Nu/Nu_{fc}$  in figure 4.4b. At the lowest  $k_x$  the average bulk temperature has increased to about  $2/3$ . In that case top plate is split in half and only one half is contributing to heat transfer. While ignoring the adiabatic area, we can divide the conducting areas into three equally sized parts with two parts on the bottom plate and one on the top plate. Using the same reasoning to that used for the symmetric case, we obtain the following equality for the average

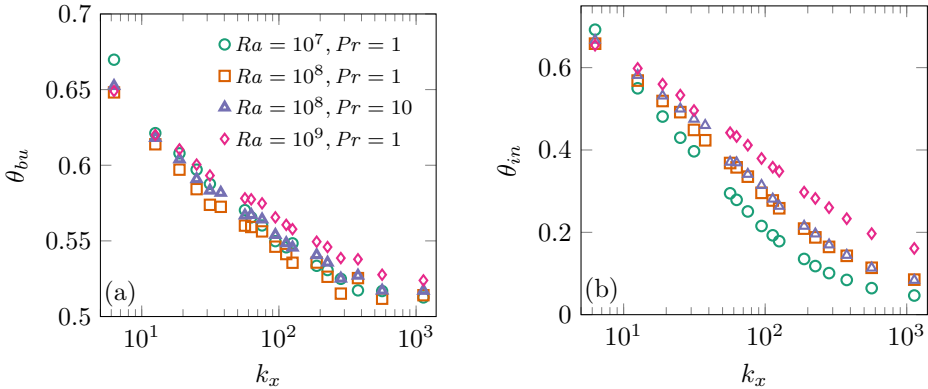


Figure 4.5: (a) Temperature of the bulk fluid  $\theta_{bu}$  for various Nu and Pr versus pattern wavenumber  $k_x$ . (b) Temperature below the insulating stripes  $\theta_{in}$ , averaged over the entire insulating area, for different Ra and Pr against pattern wavenumber  $k_x$ .

bulk temperature:  $\theta_{bulk} = \frac{2}{3}\theta_{bottom} + \frac{1}{3}\theta_{top} = 2/3$ . As with  $Nu/Nu_{fc}$ , we see that the average bulk temperature approaches the fully conducting case of  $\theta_{bulk} = 1/2$  for increasing  $k_x$ . When comparing the various curves, they all appear similar, with a maximum difference of about 0.02 to 0.03 in the average bulk temperature. Unfortunately, similar experiments do not report their average temperature [164] and a comparison to their calculations with large-wavelength imperfect boundary conditions is impossible.

In figure 4.5b we show the horizontally and time averaged temperature below the insulating area of the top plate as function of the wavenumber. At the lowest wavenumber (top plate split into equal conducting and insulating regions), we see that the averaged temperature is almost equal for all Ra and Pr. When increasing  $k_x$ , a dependence on Ra emerges. After just a few additional divisions in stripes, all curves order themselves according to Ra, with the lower Ra values approaching the lower bounds faster than the larger ones. At the largest  $k_x$ , the temperature difference between  $Ra = 10^9$  and  $Ra = 10^7$  is 15%. As the temperature below the insulating area is slightly higher than for the area below the conducting area because of lack of cooling, we can conclude that for larger Ra, the whole top layer is, on average, hotter than for the lower Ra.

These results suggest that it could be possible to account for the  $Nu(k_x)$  relationship by using corrected non-dimensional variables [160]. However,

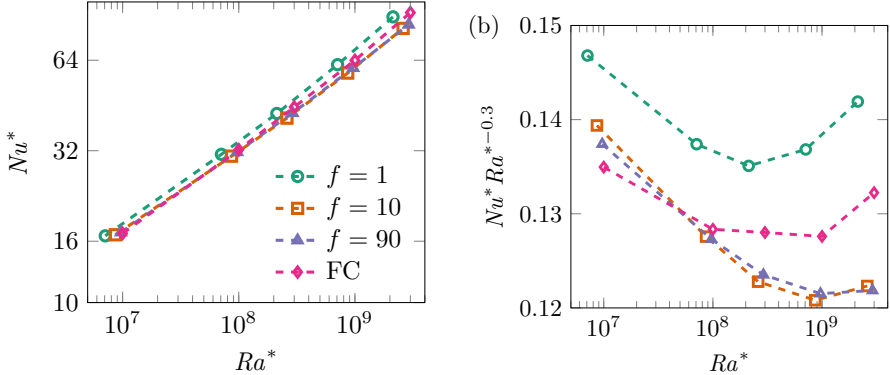


Figure 4.6: (a) Corrected Nusselt number against compensated Rayleigh number for selected pattern wavelengths. (b): Compensated and corrected Nusselt number against corrected Rayleigh number. No collapse, or natural ordering of the curves can be seen.

changing the (effective) thermal conductivity, ignores the heterogeneities of the plate which is the main source of the observed behavior. In figure 4.6, we show the corrected Nusselt number  $Nu^* = Nu/\theta^*$  against the corrected Rayleigh number  $Ra^* = Ra\theta^*$ , where  $\theta^*$  is the non-dimensional average temperature difference given by  $\theta^* = L_p \theta_{in}/L_p$ . No logical ordering can be seen, and as expected, an attempt to describe the results with some global effective thermal conductivity fails.

For horizontal slices of the instantaneous temperature field, a discrete two-dimensional Fourier transform can be applied, which is defined as:

$$\Theta(\gamma) = \left| \left\langle \sum_{y=0}^{n_y-1} \sum_{x=0}^{n_x-1} e^{-i[(2\pi/n_x)j_x x + (2\pi/n_y)j_y y]} \theta(x, y, t) \right\rangle_t \right|_{j_x=\gamma, j_y=0} \quad (4.4)$$

where  $\langle . \rangle_t$  is the time average and the  $j_y$  mode was set to zero, leaving a single wavenumber parameter  $\gamma \equiv j_x$ . Using the described method on the horizontal slice just below the top boundary we can identify the imprint the stripe structured BC leave on the flow.

Using the Fourier transform we one identify the imprint of the BC just below the top boundary in the flow itself. Using this distinct signature we can find out how far this pattern is still present once one moves away from the boundary wall. The distance from the top boundary wall is indicated using  $\hat{z}$ . In figure 4.7, we see the compensated spectra for  $f = 1$  at five different

planes for increasing  $\hat{z}$ . The colors are used to identify the different modes and except for figure 4.7d) are compiled using a single dataset (odd or even value). When moving away from the wall, we see that the two distinct modes approach each other and just outside the boundary layer, at  $\hat{z} = 0.970$ , it is hard to distinct the two different curves at all. Within the boundary layer the signature of the pattern almost completely fades away and in the bulk flow is not visible at all. The difference between the Fourier transform just outside the BL ( $\hat{z} = 0.970$ ) and at mid-height of the system ( $\hat{z} = 0.5$ ) is marginal. These findings hold for the complete range of  $f$ .

It is quite remarkable that even for the most extreme case at  $f = 1$ , the pattern is not visible in the bulk region. This means that in the boundary layer, in which conduction dominates, the temperature differences of the top plate are averaged such that an effective, slightly higher cold plate is seen by the bulk flow.

### 4.3.2 Patterns on both plates

Until now we only applied the insulating and conducting patches to the top boundary. This resulted in a normalized heat transfer of approximately two-thirds for the lowest  $k_x$  and almost the fully conducting case at the highest  $k_x$ . Using a simple argument we could indeed rationalize the value of two-thirds for the normalized heat transfer for the lowest wavenumber. If we now apply the same pattern also on the bottom plate, can we still get to the same efficiency as if we only applied the pattern to the top boundary wall?

The comparison of the normalized Nusselt number  $\text{Nu}/\text{Nu}_{fc}$  between the single- and double-sided case is shown in figure 4.8a. For the lowest  $k_x$  we see that the double-sided case conducts heat at approximately half the rate of the fully conducting case. This is in line with the expectations, as we only have half the effective area on both boundary walls. What also is visible is that the curve for the double-sided case is steeper than the curve of the single-sided case and therefore reducing the difference between both cases with increasing  $k_x$ . For the largest  $k_x$  the heat transfer of this system again is almost as efficient as if it were fully conducting. There is only half of the area available for heat entering the system and only half the area for heat leaving the system. Still, the same amount of heat transfer as if the system were fully conducting is achieved. For the single-sided case as for the double-sided one, for the lowest  $k_x$  the efficiency is not exactly  $2/3$  and  $1/2$  but slightly above these values. The

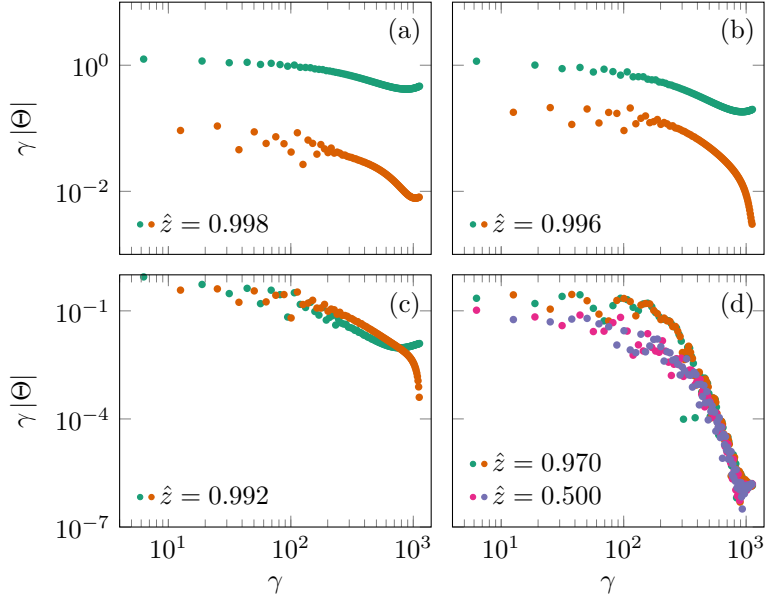


Figure 4.7: Premultiplied two-dimensional Fourier transform of a horizontal slice at various distances from the top boundary wall, averaged in time. Except for figure 4.7d, each figure is compiled using a single dataset. The colors help to identify the different modes which are present in each single dataset and are identified by the odd or even value. a) At the closest gridpoint ( $\hat{z} = 0.998$ ), the two different modes are clearly visible. b) One gridpoint further ( $\hat{z} = 0.996$ ), the distinction slowly fades. c) While still inside the boundary layer at  $\hat{z} = 0.992$ , both modes are practically overlapping. d) Just outside the boundary layer, it is impossible to distinguish two different modes at all. As a reference, we also show the spectrum at the centre of the system ( $\hat{z} = 0.5$ ).

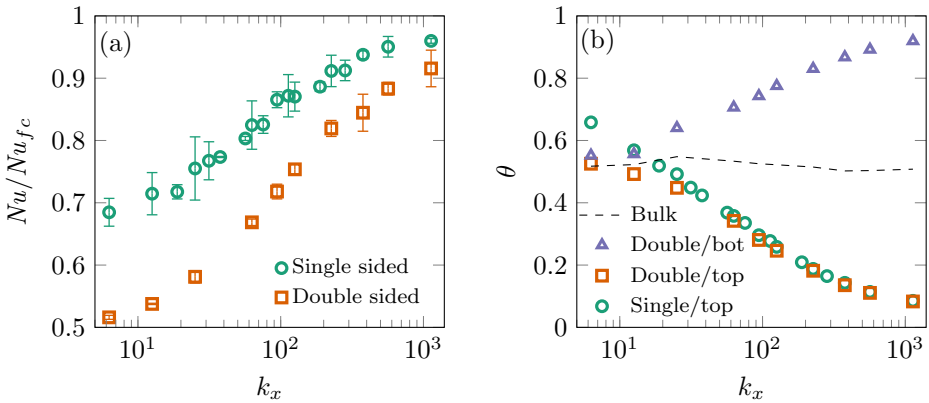


Figure 4.8: (a) Comparison of the normalized Nusselt number  $Nu/Nu_{fc}$  for the single and double-sided cases with  $Ra = 10^8$ ,  $Pr = 1$ , and  $\ell_C = 0.5$ . For the lowest  $k_s$  we see that the system is about  $2/3$  and  $1/2$  of the fully conducting case for the single and double-sided case, respectively. (b) Average temperature above or below the insulating stripes for the single- and double-sided case with  $Ra = 10^8$ ,  $Pr = 1$ , and  $\ell_C = 0.5$ . The dashed line shows the average bulk temperature, calculated at mid-height for the double-sided system.

geometry of the double-sided case can be decomposed into a regular Rayleigh-Bénard cell and a neutral domain, both with identical dimensions, positioned next to each other. The top and bottom boundaries from this neutral domain are both insulating and heat can only enter and exit from the sides. As we have periodic BC in the horizontal direction, both sides of the regular RB area are connected to this neutral domain which acts as a buffer for heat. This extra buffer is the only difference and thus the cause for the small difference.

The average temperature just below or above the insulating boundaries are shown against  $k_x$  in figure 4.8b. The difference in temperature below the top insulating boundary between the single-sided case, shown in green circles, and the double-sided case shown in orange squares is only significant at the lowest  $k_x$ . Only at the lower  $k_x$ , the single-sided system is hotter, just below the boundary. At larger  $k_x$ , the asymmetry does not make a difference on the temperatures and both temperatures converge to the conducting plate temperature. In the same plot, we also show the temperature just above the insulating area of the bottom plate and the bulk temperature. For the double-sided case for the lowest  $k_x$ , the top, bottom, and bulk temperatures are very

similar. This indicates that for the lowest  $k_x$  all the fluid in neutral domain, the large area confined by the insulating bottom and top plate, has approximately the same temperature and hardly contributes to the heat transfer. This fully agrees with  $\text{Nu}/\text{Nu}_{fc} \approx 0.5$  seen in figure 4.8a. The bulk temperature of the double-sided case stays approximately 0.5 for the full range of  $k_x$ , as must hold for a symmetric system. Temperatures above the bottom boundary and below the top boundary are also symmetric with respect to the bulk temperature confirming statistical convergence of our calculations. As for the single-sided case, figure 4.8b shows that for the largest  $k_x$  the temperature close to the insulating areas are very close to their conducting counterpart. The heat conduction in the boundary layer makes the bulk fluid see an almost perfect heat conductor.

### 4.3.3 Variation of the insulating fraction

All systems which we discussed until now had a conducting area with the size equal to the insulating area, i.e.  $\ell_C = 1/2$ . We can now vary  $\ell_C$  and look into its effect on the heat transfer. In the previous simulations we used  $k_x$  as the wavenumber and this sets the number of insulating and conducting stripes in the two-dimensional case. The width of the system,  $L_x$ , was divided in  $f$  equal pairs of these stripes. In the previous subsection, these divisions were of equal areas. Now we will change the ratio of areas to make the top plate less and less conducting. For these simulations we fixed  $k_x = 9$ ,  $\text{Ra} = 10^8$  and  $\text{Pr} = 1$ . Then the ratio between the insulating and conducting area was varied, namely we simulated  $\ell_C = 1.0, 0.875, 0.75, 0.625, 0.50$ , and  $0.25$ , thus gradually reducing the conducting area of the top plate from 85% to 25%.

Figure 4.9 shows the results of the simulations, as well as the data from the rectangular tank of from experiments [164] (extrapolated from Table 1). In the case where only 12.5% of the area is insulating we see that the difference with the fully conducting case is almost negligible and within the statistical error. Increasing the amount of insulating area to 25%, the heat transfer is still more than 90% of the fully conducting case. Even at 50% conducting region we still get the effectiveness of 80%. At the largest ratio of 75% insulating fraction we are still above 60% of the heat transfer of the fully conducting case. In other words, the effective area of the top plate is only a quarter of the fully conducting case but still we get a system that is only 40% less effective.

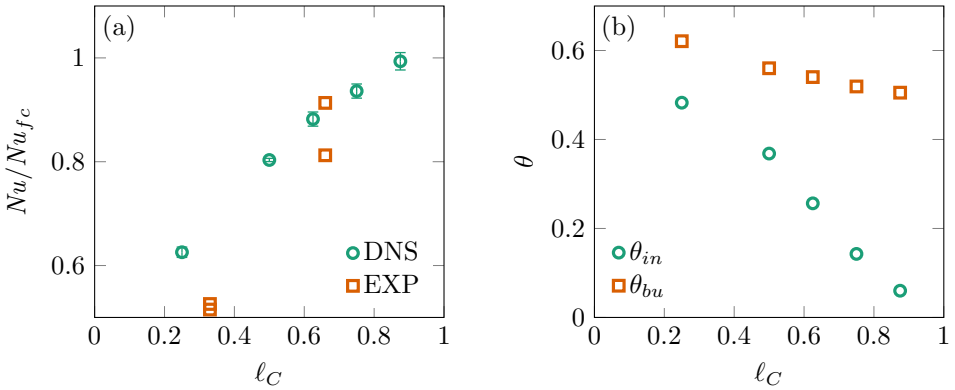


Figure 4.9: (a) Normalized Nusselt number  $Nu/Nu_{fc}$  for various fraction  $\ell_C$  of the conducting plate, while keeping the pattern frequency  $f = 9$ ,  $Ra = 10^8$ , and  $Pr = 1$  (green circles), and the rectangular tank experimental data [164] (orange squares). (b) Average temperature just below the insulating area  $\theta_{in}$  and average bulk temperature  $\theta_{bu}$ , both plotted against  $\ell_C$ . Other parameters are the same as for (a).

The rectangular tank in the experiment [164] has patches with dimensions comparable to the system size. Two data points for the two different wavelengths are available for each  $\ell_C$ . The data point with a smaller wavelength ('ACA' and 'CAC' patterns) corresponds to the higher values of  $Nu$ . While the points at  $\ell_C = 1/3$  show a considerably lower  $Nu$  than the DNS with a much smaller wavelength, a relatively good match between DNS and the experiment for  $\ell_C = 2/3$  provides some indication that at higher values of  $\ell_C$  the saturation wavenumbers, for which  $Nu \approx Nu_{fc}$  are smaller.

Figure 4.9b shows two different temperatures, namely, the average temperature just below the insulating region  $\theta_{in}$  and the average bulk temperature  $\theta_{bu}$  measured at mid-height of the system. For  $\ell_C = 0.85$ ,  $\theta_{in}$  is very close to zero, i.e. the top wall temperature. This is consistent with  $Nu$  nearly having the value of the conducting case (figure 4.9a). Also the bulk temperature is very close to the fully conducting case  $\theta = 0.5$ . When  $\ell_C$  is decreased, making the top plate less and less conducting,  $\theta_{in}$  increases gradually, reaching  $\theta_{in} = 0.5$  when  $\ell_C = 0.25$ . This equals the bulk temperature in a fully conducting system. However, when  $\ell_C$  is decreased, also the bulk temperature gradually increases and nearly reaches 0.6 for  $\ell_C = 0.25$ . This rise in the bulk temperature is much slower than the rise in the temperature above the insulating area, meaning that the gradient

between insulating regions at the plate and the bulk decreases and thus does the heat transfer, see figure 4.9a. Even though these simulations were conducted using only  $f = 9$ , one expects similar trends to apply for other values of  $f$ . From the previous simulations we found that when increasing  $f$ ,  $\text{Nu}/\text{Nu}_{fc}$  will rise and  $\Theta_{ins}$  will decrease. The same response can be achieved by increasing  $\ell_C$  as we increase the conducting area and approach the case of the fully conducting system.

#### 4.3.4 Mixed insulating and conducting patterns in two dimensions

Until now, all patterns that have been applied to the top and bottom boundary wall were one-dimensional stripe-like patterns. We only varied the width of the patches and the ratio between the insulating and conducting fractions. In this subsection we add an additional spatial dependence to these patterns to make them checkerboard-like:

$$\begin{aligned} \theta(\hat{x}, \hat{y}, \hat{z} = 1) &= 0 & \sin(\pi\hat{x}) \sin(\pi\hat{y}) \geq 0 \\ \partial_z \theta(\hat{x}, \hat{y}, \hat{z} = 1) &= 0 & \sin(\pi\hat{x}) \sin(\pi\hat{y}) < 0 \\ \theta(\hat{x}, \hat{y}, \hat{z} = 0) &= 1 & \forall \hat{x}, \hat{y}. \end{aligned} \quad (4.5)$$

A schematic of a set of four patches, two insulating and two conducting, is shown in figure 4.10. The dimensions of both types of patches were kept equal, i.e.  $L_{px1} = L_{py1} = L_{px2} = L_{py2}$ , meaning  $\ell_c = 1/2$ .

As we took both horizontal dimensions to be equal, we define a single frequency  $f$  in both directions. The plate is divided in  $f$  sets of patches which have dimensions  $L_{px} = L_{py} = L_p$ . When  $f = 1$  the complete boundary consists of a single set of patches. By increasing  $f$  to 2, the plate will consist of four sets of four patches each. To give a further impression how the temperature fields resulting from these boundary conditions look like, two visualizations of instantaneous temperature fields for  $f = 4$  and  $f = 20$  are shown in figure 4.11. The visualizations show respectively 16 and 400 sets of patches, which each consists of two insulating and two conducting areas.

Figure 4.12a shows the normalized Nusselt number  $\text{Nu}/\text{Nu}_{fc}$  for the 1D-(stripe) and 2D (checkerboard) patterns as function of  $k_x$ . For these cases,  $\text{Ra} = 10^8$ ,  $\text{Pr} = 1$  and the error bars indicate the statistical convergence error. On first sight, the heat transfer is not that different when applying one-dimensional or two-dimensional patterning. At the lowest division, where we have divided the system into two or four areas for the 1D and 2D case

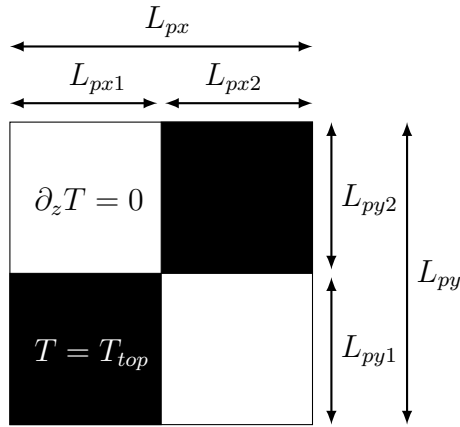


Figure 4.10: Top view of the top plate boundary conditions with applied checkerboard pattern ( $f = 1$ ).  $L_{px}$  and  $L_{py}$  are the horizontal and vertical dimensions of a set of patches. The set itself is divided in two insulating (white) and two conducting (black) areas, all with equal dimensions:  $L_{px1} = L_{py1} = L_{px2} = L_{py2}$ .

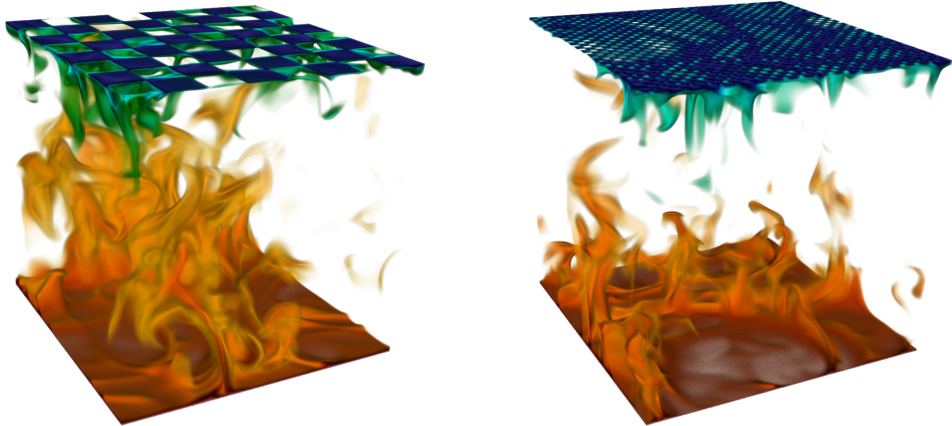


Figure 4.11: Two 3D visualizations of the instantaneous temperature field with different pattern frequencies at the top boundary. Only the extremes of the temperature are shown, such that hot fluid is shown in red while the cold fluid has a blue color. At the boundary, this results that the conducting regions are blue and the insulating regions transparent. For both visualizations,  $\text{Ra} = 10^8$  and  $\text{Pr} = 1$ . The left visualization shows  $f = 4$ , which results in 16 sets of patches containing each two insulating patches and two conducting patches. The right visualization has  $f = 20$  which results in 400 sets of patches. Hot plumes rise from the bottom plate while cold plumes are ejected from the top boundary.

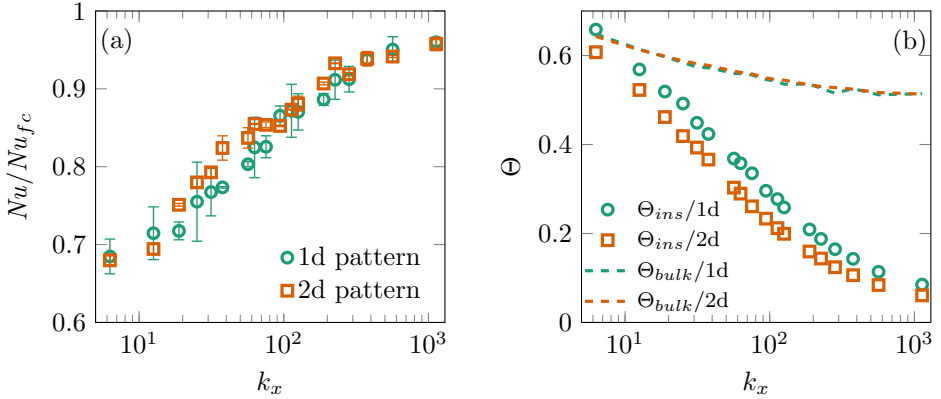


Figure 4.12: (a) Normalized Nusselt number  $Nu/Nu_{fc}$  for 1D and 2D patterning versus  $k_x$  for  $Ra = 10^8$  and  $Pr = 1$ . The error bars show the statistical convergence error. (b) Average temperature  $\theta_{in}$  just below the insulating area and average bulk temperature  $\theta_{bu}$ , both as function of  $k_x$  for the 1D and 2D patternings. The Ra and Pr are the same as for (a).

respectively, the difference is negligible. Also at the highest value of  $k_x$ , the difference is inside statistical errors and seems insignificant.

On first glance, the 1D stripe pattern and the 2D checkerboard pattern may seem idealized representations. However, all other stripe and rectangular checkerboard patterns fall within these extreme cases, as the stripe pattern has  $L_{px}/L_{py} \rightarrow \infty$  (or conversely  $\rightarrow 0$ ), while for the checkerboard pattern  $L_{px}/L_{py} = 1$ . Our work shows that, for the relatively small wavelengths considered here, the shape of these patterns do not have a significant influence on the flow dynamics. While we do not expect  $\ell_C$  to considerably affect this statement, larger wavelength patterns could show some dependence on their shape. In experiments, the patches have wavelengths comparable to the system height and their distribution considerably affects the flow structure [164]. Here, we consider wavelengths that are much smaller, affecting the flow only below the thermal boundary layer thickness, and reducing the Nusselt number. The largest wavelength considered in this work is still smaller than the smallest wavelength in the rectangular tank [164]. There appear to be two clear regimes: the large patch regime, which show a clear influence on the flow dynamics and whose effect is likely to be shape-dependent, and the small patch regime, which only affect the boundary layers and thus the heat

transfer. While there must exist a cross-over regime between both, it appears to be just outside the wavelengths we are considering.

When we look at  $\theta_{in}$ , the temperature just below the insulating region in figure 4.12b, we see a similar trend. The temperature just below the insulating region is on average always lower for the 2D pattern. This is even the case for the higher and lower limit of  $k_x$ . The average temperature just below the conducting area is very close to zero, regardless of which  $k_x$ . Therefore, the distance of the colder regions is shorter for the 2D- as for the 1D-pattern. This also explains that  $\theta_{in}$  for the 2D case is slightly lower when compared to the 1D case. The bulk temperature for both the 1D and 2D cases are almost identical which means that the change in pattern has no effect on this quantity. From these results we can conclude that the impact of the two different patterns is very similar, and the quantitative differences between stripe and checkerboard patterns are at most small.

## 4.4 Summary and conclusions

A series of DNS of turbulent Rayleigh-Bénard convection using mixed conducting- and insulating boundary conditions were conducted. First, we applied a stripe-like pattern on the top boundary and varied the amount of stripes while keeping conduction-insulation ratio constant at  $\ell_C = 1/2$ . When the top plate is divided in half, Nu has a value of approximately two-thirds of the fully conducting case. By increasing the frequency of the pattern, the Nu also increases, with a maximum value very close to as if it were fully conducting. With only half the effective conducting area on the top plate, when applying a dense pattern, the effect of the insulating patches almost completely vanishes. An increase in Ra results only in a marginal decrease in  $\text{Nu}/\text{Nu}_{fc}$  for the largest  $f$ . This shift towards the fully conducting efficiency as seen with the Nusselt number when increasing the pattern frequency is also visible in  $\theta_{bulk}$  and  $\theta_{ins}$ .

Using a two-dimensional Fourier transform, calculated from a horizontal slice of the instantaneous temperature it is possible to identify the imprint of the boundary conditions inside the flow. By comparing different spectra, each calculated from a horizontal slice slightly further away from the top boundary wall, the penetration depth of the boundary conditions inside the flow was investigated. The imprint of the striped pattern slowly fades away when moving from the top wall towards the border of the thermal boundary

layer. Outside of the thermal boundary layer the imprint has completely vanished, even for the extreme case  $f = 1$ . The thermal boundary layer masks the actual boundary, including all insulating imperfections and presents a new effective boundary to the bulk flow. In the thermal boundary layer, the heat is conducted to the conducting areas. This transport is more efficient when the pattern frequency is large. A lower Rayleigh number increases the thickness of the boundary layer and thereby, also increases the effectiveness of the heat transport.

Extending the pattern to both, the top and bottom boundary wall, resulted in similar behavior for the heat transfer and the average temperature just below the insulating area. The primary difference is for the lowest pattern frequency where we practically have only half a RB cell and we find a Nusselt number with half the value of the fully conducting case. Adding an additional dimension to the pattern, creating a checkerboard-like pattern, also did not change the behavior significantly.

Our results demonstrate that small and even large imperfections in the temperature boundary conditions are barely felt in the system dynamics in terms of global heat transfer and local temperature measurements. Only in extreme cases as a half-and-half conducting and adiabatic plate was the effect significant. The effect of imperfect temperature boundary conditions of fully turbulent RB is weaker than the effects of velocity boundary conditions in two-dimensional RB [171], or the effect of rough elements near the boundaries [172]. It is not yet clear if these boundary imperfections lead to significant changes in the dynamics of the bulk flow and this remains an open question for future works.

Going beyond the scope of the present chapter , we mention that other simulations and experiments [165, 164] show that with even larger adiabatic patches, changes in the flow topology can happen due to the arrangement of patches. The patches can also be varied in time, which is a way to control the bulk temperature or to fine tune the heat transfer, which is relevant for many industrial applications. The combination of shear and mixed boundary conditions could also play a critical role in the system dynamics [173]. Understanding the deeper reasons for this behavior may lead to better models for natural convection for geo- and astro-physically relevant flows.



# 5

## Controlling the secondary flows in turbulent Taylor–Couette flow<sup>✉</sup>

---

Highly turbulent Taylor–Couette flow with spanwise-varying roughness is investigated experimentally and numerically to determine the effects of the normalized axial size  $\tilde{s}$  of roughness patches on the total drag on the inner cylinder and the local flow structures. We apply sandgrain roughness, in the form of alternating bands to the inner cylinder. Numerically, the Taylor number is  $\mathcal{O}(10^9)$  and  $\tilde{s}$  is varied such that  $0.47 \leq \tilde{s} \leq 1.24$  and is simulated using a direct numerical simulation in conjunction with an immersed boundary method. Experimentally, we explore  $\text{Ta} = \mathcal{O}(10^{12})$  and  $0.61 \leq \tilde{s} \leq 3.74$  in the Twente Turbulent Taylor–Couette facility ( $T^3C$ ). For both approaches the radius ratio is fixed at  $\eta = 0.716$ . We present how the flow scales with  $\text{Ta}$  and how it depends on the boundary conditions set by  $\tilde{s}$ . Both numerically and experimentally, we find a maximum in the angular momentum transport when  $\tilde{s}$  is varied. We attribute this to the re-arrangement of the large-scale structures triggered by the presence of the rough patches, which yields effectively, tuned turbulent vortices with different axial wavelengths. We describe how the local flow rearranges for varying  $\tilde{s}$  and how these local effects are reflected in the global response of the system.

---

<sup>✉</sup>Based on: **Dennis Bakhuis**, Rodrigo Ezeta, Pieter Berghout, Pim A. Bullee, Dominic Tai, Daniel Chung, Sander G. Huisman, Roberto Verzicco, Detlef Lohse, and Chao Sun *Controlling the secondary flows in turbulent Taylor–Couette flow using spanwise varying roughness*, in preparation. Experiments are done by Bakhuis, Ezeta and Bullee. Numerical simulations are done by Berghout. Analysis of PIV and LDA is done by Ezeta. Analysis of the torque and LDA is done by Bakhuis. Writing is done by Bakhuis, Ezeta, Berghout, Bullee, and Huisman. Supervision by Huisman, Chung, Verzicco, Lohse and Sun. Proofread by everyone.

## 5.1 Introduction

Many turbulent flows are bounded by irregular, rough, boundaries. These flows are extensively studied, under the approximation that the roughness is homogeneous [174]. Homogeneously rough surfaces have a characteristic length scale  $k$  that is much smaller than the largest wall normal length scale  $\delta$ . The effects of the roughness in these flows is believed to be confined to the immediate vicinity of the wall (i.e. the roughness sublayer), whereas in the outer, inertial, layer, the flow only experiences the effective shear stress of the surface, i.e. Townsend's outer layer similarity [175]. As such, the focus of many studies was to find functional relationships between the parameters that describe both the roughness geometry and the skin friction coefficient  $C_f$  [176]. In practice, however, flows are bounded by rough boundaries that not only vary on the scale of  $k$ , but also on a much larger scale  $s$ , where  $s = O(\delta)$ . Whereas these variations can be either laterally (spanwise) or longitudinally (streamwise), we focus here on the former. Examples of these flows are found in shipping (i.e. the formation of patches of biofouling on ship hulls [177]) and geophysical flows (e.g. the atmospheric flows over spanwise-varying terrain [178]).

Hitherto, the research is focused on the effects of spanwise-varying rough surfaces on canonical systems of wall-bounded turbulence research, i.e. pipe flow [179], boundary layer flow [180] and channel flow [181]. The hallmark of flows over these surfaces is the presence of spanwise wall-normal secondary flows of the size  $O(\delta)$ , with mean streamwise vorticity. Examples of studies where this has been observed are the works of Ref. [179] on the effects of convergent and divergent grooves (reminiscent of shark skin) and the work by [182] on spanwise-varying riverbeds. We note that earlier research dates back to the works of Ref. [183, 184] on the field of surface stress variations in duct flows.

Following up on the work of [179], [185] set out to perform a parametric study of the converging-diverging riblets surface in a zero pressure gradient BL. They find a thickening of the BL height above the converging regions, and a thinning of the BL height above the diverging regions. Furthermore, the energy spectra shows an increased energy content of the larger scales. [186] performed stereo particle image velocimetry (PIV) in the spanwise wall-normal plane of the flow over a turbine blade replica and found spanwise variations of the order of  $\delta$  in the mean velocity field. With the

same configuration, Ref. [187] identified regions of low momentum pathways (LMPs) and high momentum pathways (HMPs) in the instantaneous fields. Here, LMPs coincide with regions of enhanced turbulent kinetic energy (TKE) and Reynolds shear stress (RSS), and rather remarkably, these regions do seem to occur at recessed roughness heights. [188] found very similar behavior of the secondary flows for a much more regular surface geometry. [189] found that only when  $s/\delta \gtrsim 0.5$ , where  $s$  is the spacing between the streamwise aligned Lego® blocks, secondary flow formation is observed. However, for  $s/\delta \lesssim 0.5$  the secondary flows are confined to the roughness sublayer. Interestingly, contrary to the findings of Ref. [187], they find LMPs on top of their elevated blocks, and HMPs in between the roughness strips. [190], however, found  $s/H \gtrsim 0.2$ , with  $H$  the channel half height, as the threshold for heterogeneous behavior of the streamwise aligned pyramid elements. By carefully assessing the terms in the transport equation of TKE, [180] found that spanwise variations of roughness leads to a local imbalance of production and dissipation of TKE, as already proposed by [183]. Since the secondary flows are driven by a spatial gradient in the RSS, they find that the mean secondary flows are Prandtl's secondary flow of the second kind [191]. [192] observed a breakdown of outer layer similarity in the local profiles of the mean flow, turbulent intensity, and the energy spectra, evidently induced by the presence of the secondary vortices. Finally, [181] studied the influence of the spacing of idealized (i.e. no geometric induced disturbances to the flow) regions of low shear stress and high shear stress. They find that for  $s/\delta \lesssim 0.39$  the notion of outer layer similarity is retained. Interestingly, for  $s/\delta \gtrsim 6.28$ , they find a sign reversal of the isolines (stream velocity contour lines), with respect to the orientation of the secondary flows, that remain upwelling over low shear stress regions.

The aforementioned studies were all carried out in systems that lack two characteristics which are intrinsic to many applications, namely the curvature in the streamwise direction (as in turbine blades), and the presence of strong secondary motions (as in the atmospheric boundary layer). A canonical system in which these two properties can be simultaneously observed is the Taylor–Couette (TC) flow. TC flow is the flow in between two coaxially, independently rotating cylinders. Its geometry is characterized by the inner cylinder radius  $r_i$ , outer cylinder radius  $r_o$ , and the height of the cylinders  $L$ , captured by two dimensionless parameters; the radius ratio  $\eta = r_i/r_o$  and the aspect ratio  $\Gamma = L/d$ , where  $d = r_o - r_i$  is the gap in between the cylinders. Since TC is a closed system, one can directly relate

global and local quantities through exact mathematical relations [12]. The driving in TC flow is expressed in dimensionless form by the Taylor number:

$$\text{Ta} = \frac{1}{4}\sigma d^2 \frac{(r_i + r_o)^2(\omega_i - \omega_o)^2}{\nu^2}, \quad (5.1)$$

where  $\omega_{i,o}$  are the inner and outer angular velocity of the cylinders respectively,  $\nu$  is the kinematic viscosity, and  $\sigma = ((1 + \eta) / (2\sqrt{\eta}))^4$  is the so-called geometric Prandtl number, in analogy to the Prandtl number in Rayleigh-Bé convection [12]. Alternatively, when the outer cylinder is at rest ( $\omega_o = 0$ ), the driving can also be expressed with a Reynolds number based on the outer scales  $\text{Re}_i = r_i \omega_i d / \nu$ . This Reynolds number and  $\text{Ta}$  (for  $\omega_o = 0$ ), are related by  $\text{Re}_i = (8\eta^2/(1 + \eta)^3)\sqrt{\text{Ta}}$ . In TC flow, the angular velocity flux  $J^\omega$  is radially conserved. Here,  $J^\omega = r^3(\langle u_r \omega \rangle_{A,t} - \nu \frac{\partial}{\partial r} \langle \omega \rangle_{A,t})$ , where the brackets  $\langle \cdot \rangle_{A,t}$  denote averaging over a cylindrical surface and time. The angular momentum flux for the case of laminar flow is  $J_{lam}^\omega = 2\nu r_i^2 r_o^2 (\omega_i - \omega_o) / (r_o^2 - r_i^2)$ . In this way the response of the flow is quantified with the dimensionless Nusselt number ( $\text{Nu}_\omega$ ), which is also directly related to the torque  $\mathcal{T}$  that is required to drive the cylinders at constant speed, i.e.

$$\text{Nu}_\omega = \frac{J^\omega}{J_{lam}^\omega} = \frac{\mathcal{T}}{2\pi L \rho J_{lam}^\omega}. \quad (5.2)$$

Alternatively, the torque of the system can be non-dimensionalized to form the friction coefficient  $C_f = \mathcal{T}/(\rho L \nu^2 \text{Re}_i^2)$ , which is directly related to the Nusselt number:

$$\text{Nu}_\omega = C_f \omega_i (r_o - r_i)^2 \left( r_o^2 - r_i^2 \right) / \left( 4\pi \nu r_o^2 \right). \quad (5.3)$$

The inner friction velocity  $u_{\tau,i}$  is also related to the torque by  $u_{\tau,i} = \sqrt{\mathcal{T}/(2\pi r_i^2 \rho L)}$ , which is used to non-dimensionalize quantities in the inner layer. Lastly, a frictional Reynolds number based on the inner scales can be defined as  $\text{Re}_\tau = u_{\tau,i} d / (2\nu)$ .

The scaling of the response of the flow with the driving has been extensively studied in the literature [60, 61, 137, 62, 64, 65, 9]. In the so-called ultimate regime of turbulence [193, 194], where the boundary layers are fully turbulent ( $\text{Ta} > \mathcal{O}(10^8)$ ), it was shown that effectively  $\text{Nu}_\omega \propto \text{Ta}^{0.4}$ , independently of both  $\eta$  and the rotation ratio of the cylinders  $a = -\omega_o/\omega_i$  [68, 138].

Secondary flows are featured in TC flow, in the form of large scale vortices with a mean streamwise vorticity component, the so-called turbulent Taylor Vortices (TTV). These structures are reminiscent of laminar Taylor vortices, which transition through a series of instabilities into turbulence once the flow becomes predominantly unstable after a critical value of the Reynolds number [195]. As noted by Ref. [196], the axial wavelength  $\lambda$  of the TTVs, *i.e.* the distance between two rolls, is primarily a function of  $\eta$  and  $Re$ . When  $Re$  is large ( $\mathcal{O}(10^6)$ ), the rolls are observed to persist in the system [69]. Here, multiple states for  $\eta = 0.716$  can be observed in a certain regime of counter-rotating cylinders, namely  $a \in [0.17, 0.51]$ , where  $a = -\omega_o/\omega_i$  is the rotation ratio of the cylinders. These multiple states are characterized by a change in the number of rolls present in the system, and as a consequence, in their averaged axial wavelength ( $\lambda/d = 1.46$  or  $\lambda/d = 1.96$ ). These states—being strongly hysteretic—result in different torques for the same rotation rates, which reflects the importance of the large scale structures (TTV) in transporting angular momentum. At pure inner cylinder rotation however ( $a = 0$ ), no multiple states are detected and the rolls are observed to be less coherent and stable. Finally, we note that the effect of the curvature of the cylinders is quantified with the radius ratio  $\eta$ , and it has a tremendous impact on the flow organization as it was thoroughly reported by Ref. [197, 103]. For a more detailed review we refer the reader to Ref. [198, 9].

It is not the first time that roughness is studied in a TC geometry. Ref. [199, 200] used obstacle roughness, in the form of axial riblets, to study the scaling of the angular momentum transport with the driving. Ref. [201] investigated the influence of grooves for large  $Ta$  ( $\mathcal{O}(10^{10})$ ), and find that at the tips of the grooves, plumes are preferentially ejected. In a more recent work, Ref. [202] find that by using a similar configuration of rough walls as Ref. [200], the scaling that corresponds to the ultimate regime, originally predicted by Kraichnan *i.e.*  $Nu_\omega \propto Ta^{1/2}$  [193], can be achieved. They attribute this to a dominance of the pressure drag over the viscous drag on the cylinders. Structure in the form of grooves in the streamwise direction were studied by Very recently, [203] studied the influence of sandgrain roughness in TC flow, and found similarity of the roughness function with the same type of roughness in pipe flow [204]. We highlight that none of the works described above, reported an influence of the roughness over the axial wavelength of the rolls.

In this chapter we study the effects of spanwise-varying roughness in highly turbulent TC flow  $\mathcal{O}(10^{12})$ , where the effect of curvature is present due to

the cylinders, and for the case of pure inner cylinder rotation  $a = 0$ , where secondary flows are present in the form of TTVs. In particular, we focus on the effect of spanwise-varying roughness on the TTVs and thus, on the global and local response of the flow. We introduce the roughness through a series of patches which extend along the entire circumference of the inner cylinder (IC). This gives rise to a spanwise (axial) arrangement of roughness which we characterize with the width of the rough patch  $s$ . We conduct both experiments and direct numerical simulations (DNS) for various  $\tilde{s} = s/d$ , i.e. the width of the rough patch normalized with the gap width.

The structure of the chapter is as follows. In section 5.2 we introduce the experimental and numerical methods. In section 5.3.1 we show the local response of the flow due to the varying roughness width. In section 5.3.2, we study its effect on the global quantities. In section 5.3.3 we link the global and local observations and provide the physical mechanism between the interaction of the rolls and the roughness. We finalize the chapter in section 5.4 with some conclusions and future work.

## 5.2 Methods

### 5.2.1 Experimental apparatus with spanwise roughness

The experiments were performed in the Twente Turbulent Taylor–Couette ( $T^3C$ ) facility as shown in figure 5.1a (details of the experimental facility can be found in Ref. [63]). The inner cylinder has a radius  $r_i = 200$  mm and the outer cylinder has a radius  $r_o = 279.4$  mm, such that the gap size is  $d = r_o - r_i = 79.4$  mm, and the radius ratio  $\eta = 0.7146$ . The length of the cylinders is  $L = 927$  mm, which leads to an aspect ratio  $\Gamma = L/d = 11.7$ . The outer cylinder (OC), is made from transparent acrylic which allows for optical access to the flow. The working fluid is demineralised water. We apply axially varying roughness to the inner cylinder (IC), which leads to patterns of uniformly rough and hydrodynamically smooth bands in the spanwise direction (see figure 5.1a). The rough patches are made of P36 ceramic industrial grade sandpaper and are fixed to the IC using double-sided adhesive tape. In figure 5.2, we show the height scan of a roughness element using confocal microscopy. The scan revealed that the

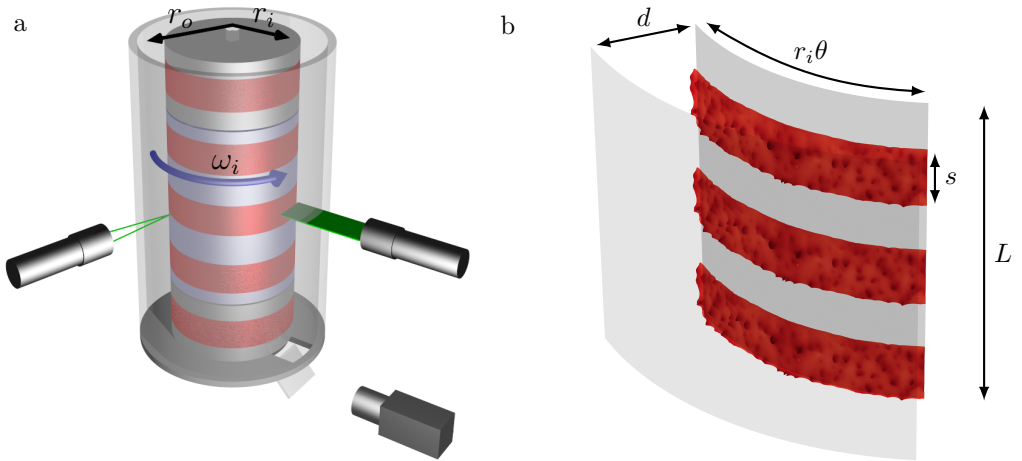


Figure 5.1: a) Schematic of the Twente Turbulent Taylor–Couette showing the sandpaper on the inner cylinder in red. PIV measurements in the  $r$ – $\theta$  plane are illuminated from the side using a high-power laser creating a horizontal sheet. The sheet is imaged through a window in the bottom. Using LDA the azimuthal velocity is measured along the axial direction. The torque is measured in the middle section of the IC, which has a length of  $L_{mid} = 536$  mm. b) Numerical domain for the case of  $\tilde{s} \equiv s/d = 0.47$ , sandpaper roughness taken from the scan of the material used in the experiment, see figure 5.2.

height ( $h_r$ ) of the roughness is mostly within  $\pm 2\sigma(h_r)$  of the mean, giving a characteristic length scale  $k \equiv 4\sigma(h_r) = 695 \mu\text{m}$ , see figure 5.2b. More statistics of the roughness is shown in table 5.1. We fix the roughness coverage at 56% such that  $0.56A_i$  of the cylinder is rough, where  $A_i = 2\pi r_i L$  is the area of the entire IC. In addition, the torque is measured only in the middle section of the IC with a coverage of also 56%.

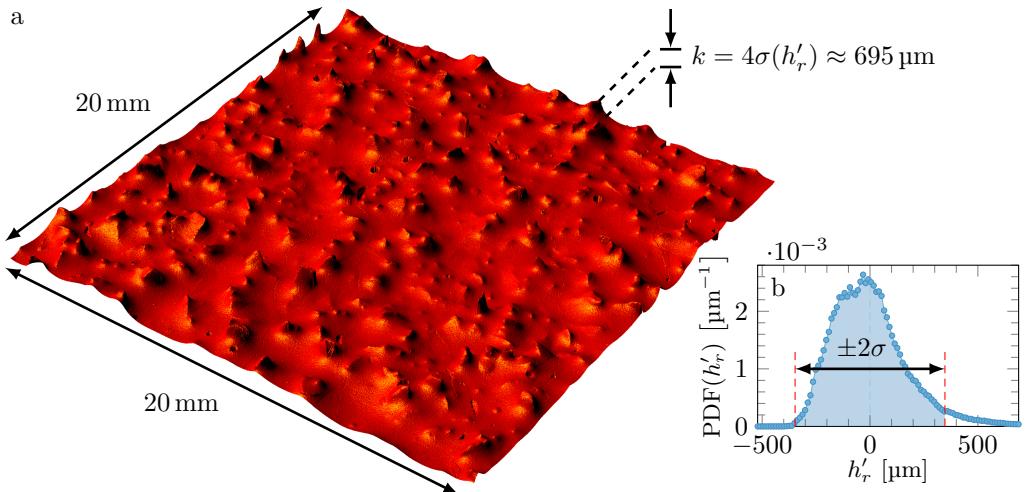


Figure 5.2: a) Height scan captured using confocal microscopy of a roughness patch of  $20 \text{ mm} \times 20 \text{ mm}$  with a resolution of  $2.5 \mu\text{m}$ . The typical size of the grains is given by  $k \equiv 4\sigma(h_r) = 695 \mu\text{m}$  where  $h_r$  is the height and  $\sigma$  the standard deviation. The normalized typical grain size is then  $k/d \approx 0.01$ . b) Probability density function (PDF) of the measured height of the roughness patch, with subtracted mean  $h'_r = h_r - \langle h_r \rangle$ .

Metric	Value
$\sigma(h_r) = \sqrt{\langle h_r'^2 \rangle}$	$174 \mu\text{m}$
$\langle  h'_r  \rangle$	$134 \mu\text{m}$
$\min(h'_r)$	$-527 \mu\text{m}$
$\max(h'_r)$	$738 \mu\text{m}$
$\text{median}(h'_r)$	$-19.6 \mu\text{m}$
$\text{mode}(h'_r)$	$-27 \mu\text{m}$
$\text{IQR} = Q3 - Q1 = \text{CDF}^{-1}(0.75) - \text{CDF}^{-1}(0.25)$	$215 \mu\text{m}$
$\langle h_r'^3 \rangle / \langle h_r'^2 \rangle^{3/2}$	$0.928$
$\langle h_r'^4 \rangle / \langle h_r'^2 \rangle^2$	$4.361$
wetted area/flat area	$\approx 1.6$

Table 5.1: Various statistics of the roughness  $h'_r = h_r - \langle h_r \rangle$  based on the data obtained from confocal microscopy, see also figure 5.2.

### Global measurements: Torque

We measured the torque,  $\mathcal{T}$ , that is required to drive the inner cylinder at constant angular velocity (the outer cylinder is kept at rest). For this we use a hollow flange reaction torque transducer connecting the driving shaft and the inner cylinder. We continuously measure the torque while quasi-statically ramping the frequency of the inner cylinder,  $f_i$ , from 5 Hz to 18 Hz. This corresponds to  $Ta \approx 4 \times 10^{11}$  and  $Ta \approx 6 \times 10^{12}$ . All the experiments are performed at  $21 \pm 1^\circ\text{C}$  and all quantities are calculated using the actual measured temperature. Table 5.2 shows additional experimental parameters.

### Local measurements: LDA and PIV

We performed an axial scan of the azimuthal velocity with laser Doppler anemometry (LDA). The scan was performed at the middle of the gap,  $\tilde{r} = (r - r_i)/d = 0.5$ , at a fixed  $Ta = 9.5 \times 10^{11}$ . The flow was seeded using  $5 \mu\text{m}$ -diameter polyamide particles with density of  $1030 \text{ kg m}^{-3}$  that act as tracers [205]. The laser beam goes through the outer cylinder and is focused in the middle of the gap. We correct for curvature effects by numerically ray tracing the LDA beams as it was shown in Ref. [68]. The axial extent of the LDA scans is  $0 \leq z/L \leq 0.5$ . Particle image velocimetry (PIV) measurements were performed at  $Ta = 9.5 \times 10^{11}$  (same as LDA) in the radial-azimuthal plane. The scan is done for different heights and for different  $\tilde{s}$ . The working fluid is seeded with PPMA fluorescent particles (**Dantec FPP-RhB-10**) with diameters of  $1\text{--}20 \mu\text{m}$  with a seeding density of  $\approx 0.01$  particles/pixel. These particles have an emission peak at  $\approx 565 \text{ nm}$ . We illuminate the particles with a **Quantel Evergreen 145** 532 nm, double pulsed laser. A cylindrical lens is used to create a light sheet of  $\approx 1 \text{ mm}$  thickness. The images are captured with an **Imager SCMS** ( $2560 \times 2160$  pixel) 16 bit camera with a **Carl Zeiss 2.0/100** lens. The camera is operated in double frame mode with a frame rate  $f$  which is always smaller than the interframe time  $1/\Delta t$ , i.e.  $\Delta t \ll 1/f$ . In order to enhance the particle contrast in the images, we add a **Edmund High-Performance Longpass 550 nm** filter to the camera lens. For every  $\tilde{s}$ , the axial extent of the experiments is different. This is done because—as will be shown later—the aspect ratio of the rolls change depending on  $\tilde{s}$ . For the smallest  $\tilde{s} = 0.63$  however, the axial resolution is  $\delta z/L \approx 0.011$  while for the largest value  $\tilde{s} = 3.74$ ,  $\delta z/L \approx 0.022$ . Since we scan in the axial direction, the focus of the camera is changed accordingly. The fields are resolved with a commercial PIV software (**Davis 8.0**) based

on a multi-step method. The initial window size is set to  $64 \times 64$  pixels and it decreases to  $32 \times 32$  pixels for the last iteration. The fields are calculated in cartesian coordinates, which we transform to polar coordinates. The final result is the fields in the form  $\vec{u} = u_r(r, \theta, t)\hat{e}_r + u_\theta(r, \theta, t)\hat{e}_\theta$ , where  $u_r$  and  $u_\theta$  are the radial and azimuthal velocity component which depend on the radius  $r$ , the azimuthal (streamwise) direction  $\theta$  and time  $t$ .

### 5.2.2 Numerical methods

The Navier-Stokes (NS) equations are spatially discretized by using a central second-order finite-difference scheme and solved in cylindrical coordinates by means of a semi-implicit procedure [167, 168]. The staggered grid is homogeneous in both the spanwise and streamwise directions (the axial and azimuthal directions, respectively). The wall-normal grid consists of double cosine (Chebychev-type) grid stretching. Below the maximum roughness height, we employ a cosine stretching such that the maximum grid spacing is always smaller than 0.5 times the viscous length scale  $\delta_\nu = \nu/u_\tau$ . In the bulk of the fluid, we employ a second stretching, such that the maximum radial grid spacing in the bulk is  $\approx 1.7\delta_\nu$ . The minimum radial grid spacing is  $\approx 0.33\delta_\nu$ , and thus is located at the position of the maximum roughness height, where we expect the highest shear stress. In table 5.2, we show a summary of the relevant parameters in the simulations. Time advancement is performed by using a fractional-step third-order Runge–Kutta scheme in combination with a Crank–Nicolson scheme for the implicit terms. The Courant–Friedrichs–Lowy (CFL)  $(u\Delta t)/(\Delta x) < 0.8$  time-step constraint for the non-linear terms is enforced to ensure stability. We scale the roughness patch such that the maximum roughness height, and thus the maximum blockage ratio, is  $\max(h_r) = 0.1d$ . Depending on  $\tilde{s}$ , we cut out a portion of roughness from the scanned surface. The roughness is then mirrored and pasted together to obtain a smooth, streamwise periodic, stripe. Note that we do not mirror the surface in the spanwise direction. The streamwise and spanwise lengths of the computational domain are set to match the minimum computational domain size as studied in [138]. A moving average over  $10 \times 10$  points is employed to smooth the scan from measurement noise. Finally, we set the resolution based on the demands  $(\Delta z^+, r_i \Delta \theta^+ < 3)$ , which is small enough to recover the smallest geometrical features of the surface. The sandpaper roughness is implemented in the code by an

immersed boundary method (IBM) [206]. In the IBM, the boundary conditions are enforced by adding a body force  $\mathbf{f}$  to the NS equations. A regular, non-body fitting, mesh can thus be used, even though the rough boundary has a very complex geometry. We perform interpolation in the spatial direction preferential to the normal surface vector to transfer the boundary conditions to the momentum equations. The IBM has been validated previously [206, 207, 208, 201, 141, 202].

$\tilde{s}$	$N_\theta \times N_z \times N_r$	$T_a \times 10^9$	$\Gamma$	$Re_\tau$	$C_f$	$N_{U_\omega}$	$\Delta(\omega)^+$	$\Delta r_{\min}^+$	$\Delta r_{\max}^+$
<b>Simulations</b>									
smooth	$758 \times 600 \times 840$	2.39	2.08	697	0.049	30.1	—	0.28	2.44
uniformly rough	$1324 \times 1012 \times 1200$	1.19	2.00	689	0.095	41.5	8.11	0.33	1.76
0.47	$1324 \times 1275 \times 1200$	1.33	2.52	686	0.084	38.9	6.36	0.33	1.76
0.62	$1324 \times 1121 \times 1200$	1.33	2.22	690	0.085	39.4	6.78	0.33	1.77
0.93	$1324 \times 1682 \times 1200$	1.45	3.32	692	0.079	38.1	6.21	0.33	1.77
1.24	$1324 \times 1121 \times 1200$	1.37	2.22	685	0.082	38.3	6.20	0.33	1.75
<b>Experiments</b>									
smooth		$\times 10^{12}$	$\times 10^3$						
0.61		1.00	11.7	10.1	0.024	307			
0.93		1.00	11.7	13.1	0.041	509			
1.23		1.00	11.7	13.5	0.043	534			
1.87		1.00	11.7	13.3	0.041	508			
3.74		1.00	11.7	12.9	0.039	491			
		1.00	11.7	14.4	0.049	517			

Table 5.2: List of parameters involved in both the simulations and the experiments.  $\tilde{s} = s/d$  is the normalized roughness width.  $N_\theta \times N_z \times N_r$  is the numerical resolution in the azimuthal, axial, and radial direction, respectively.  $\Delta(\omega)^+$  is the downward shift of the angular velocity profile  $\omega^+$ .  $\Delta r_{\min}^+$  is the minimum spacing in the wall normal direction at the location of the maximum roughness height.  $\Delta r_{\max}^+$  is the maximum spacing in the wall normal direction.  $r_i^+ \Delta \theta = \Delta z^+ \approx 2.7$  ( $r_o^+ \Delta \theta \approx 3.8$ ) is the grid spacing in the streamwise and spanwise directions. In the DNS, the roughness height  $k_+ = 4\sigma (h_r)_+ = 130 \pm 1$  for all rough cases. The roughness is glued to the surface and thus protruding, such that  $r_k > r_i$ , with  $r_k$  the radial coordinate of the rough surface patches and  $r_i$  the radial position of the smooth patches.

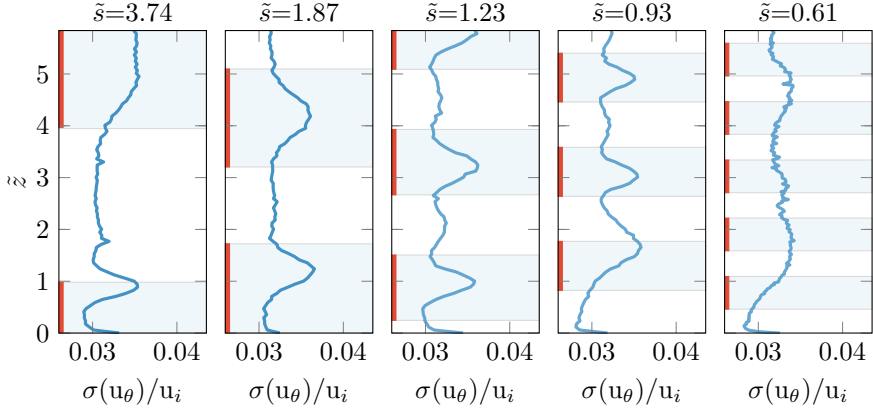


Figure 5.3: Standard deviation of the azimuthal velocity  $\sigma(u_\theta)$ , normalized by the inner cylinder azimuthal velocity  $u_i$ , as a function of  $\tilde{z} = z/d$  for various  $\tilde{s}$ .  $Ta = 1 \times 10^{12}$  for all experiments. The enforced roughness pattern is indicated in red and a light blue shade. The signature of the roughness pattern is clearly visible at mid-gap in the bulk flow. For  $\tilde{s} = 0.61$ , the roughness pattern does not leave a distinct imprint of its topology in the midgap flow statistics.

## 5.3 Results

### 5.3.1 Response of the Turbulent Taylor Vortices

In order to get a first insight on the effect of the roughness on the flow, we performed axial scans of the azimuthal flow velocity at midgap using LDA. Subsequently, we calculated the standard deviation of the azimuthal velocity. In figure 5.3, we show the standard deviation of the azimuthal velocity  $\sigma(u_\theta)$  normalized with the inner cylinder velocity  $u_i$ , as a function of the height, for various  $\tilde{s}$ . Here, the axial coordinate is normalized using the height of the cylinders such that  $\tilde{z} = z/d$ . The standard deviation is a measure of the magnitude of the velocity fluctuations and therefore, we can now quantify the effect of the applied roughness. Figure 5.3 reveals that for the case of the largest patch size ( $\tilde{s} = 3.74$ ), the smooth section has, on average, a value of  $\sigma(u_\theta)/u_i \approx 0.03$ , slightly larger than  $\sigma(u_\theta)/u_i \approx 0.023$  that is found for the smooth case (for  $Ta = 1.5 \times 10^{12}$ ) in the same apparatus [205]. Above the rough section, towards the center of the setup (i.e. for large  $\tilde{z}$ ),  $\sigma(u_\theta)$

gradually increases to a value of approximately  $\sigma(u_\theta)/u_i \approx 0.04$ . A similar, but not so clear trend can be seen at the lower roughness section ( $\tilde{z} \approx 0.93$ ) of this case. However, this might be influenced by the lower bottom plate of the system. When looking at the  $\tilde{s} = 1.87$  case, we see very similar, however more pronounced dynamics. Azimuthal velocity fluctuations are promoted in regions where the roughness is present, as suggested by the appearance of local peaks centered at the position of the rough patches. This effect is further seen for the cases of  $\tilde{s} = 1.23$  and  $\tilde{s} = 0.93$ , where we clearly observe similar profiles. At their smooth areas however, we observe plateaus for  $\sigma(u_\theta)$ , similar to the ones for the  $\tilde{s} = 3.74$  case, although with a slightly higher value. For the final case with  $\tilde{s} = 0.61$  this trend seems to fade away and we see that  $\sigma(u_\theta)$  becomes more axially independent, i.e. the peaks are less pronounced, and do not seem to follow the topology of the roughness patches. The results from figure 5.3 hints that the presence of the roughness might have an effect on the morphology of the flow, far away from the roughness sublayer region [203], on the order of the gap width  $d$ , and reminiscent to what is found in studies of pipe and channel flow [179, 181]. To gain more insight into how the roughness alters the flow, we set out to measure the velocity field in the meridional plane using PIV at multiple heights.

In figure 5.4, we show the temporal and azimuthally averaged radial velocity component  $u_r$ , normalized with  $u_i$ , in the spanwise wall-normal plane ( $\tilde{z}$ - $\tilde{r}$ ), where the radial coordinate is normalized such that  $\tilde{r} = (r - r_i)/d$ . Figure 5.4 shows that for the case of  $\tilde{s} = 3.74$ , a very large structure can be seen, which consists of a large outflow region (positive  $u_r$ ) around  $\tilde{z} = 5.84$ , while a large inflow region (negative  $u_r$ ) is detected around  $\tilde{z} = 2.10$ . The situation is more pronounced for the cases of  $\tilde{s} = 1.87$ ,  $\tilde{s} = 1.23$ , and  $\tilde{s} = 0.93$ , where a clear roll-like structure (i.e. the TTV) can be observed. Note that the radial component in the flow changes sign along the axial direction as it should in the presence of a TTV. What it is rather remarkable, is that the wavelength of the rolls  $\lambda$  changes for different values of  $\tilde{s}$ . For the large structure at  $\tilde{s} = 3.74$ , the normalized wavelength is  $\tilde{\lambda} = \lambda/d \approx 4.01$ . As  $\tilde{s}$  decreases to  $\tilde{s} = 1.87$ ,  $\tilde{\lambda} \approx 1.49$ . At  $\tilde{s} = 1.23$ , the wavelength decreases to a value of  $\tilde{\lambda} \approx 1.42$ . At  $\tilde{s} = 0.93$ ,  $\tilde{\lambda} \approx 0.94$ , and finally for the smallest value of  $s = 0.61$ , the wavelength increases slightly to  $\tilde{\lambda} = 1.09$ . We remind the reader that the work of Ref. [69], revealed that for counter-rotation ( $a \approx 0.4$ ), the average wavelength of the rolls could be either  $\tilde{\lambda} = 1.46$  or  $\tilde{\lambda} = 1.96$  depending on the *state* the system is in. The current work shows that by an appropriate choice of  $\tilde{s}$ , the wavelength of the rolls can firstly, abandon its natural state; and secondly, it

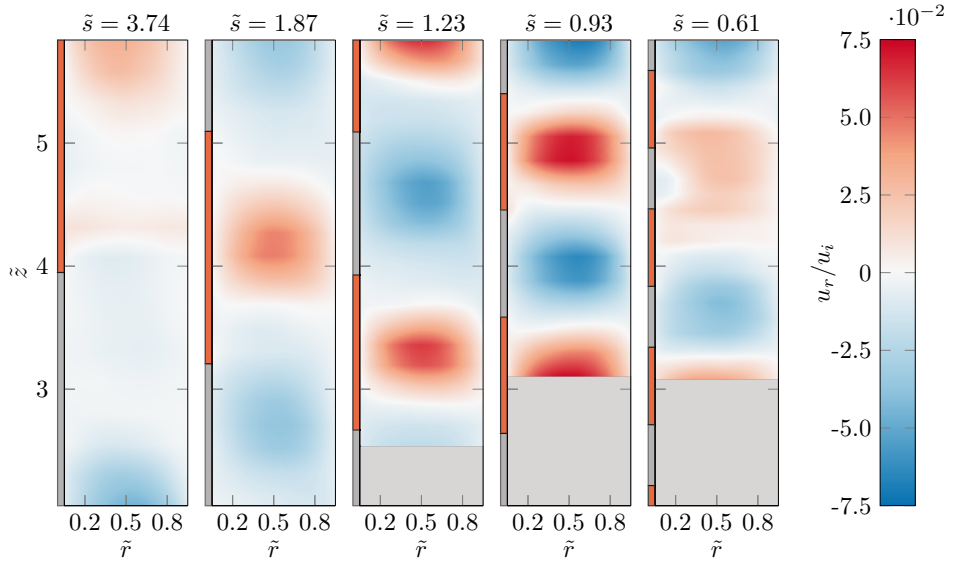


Figure 5.4: Temporal and azimuthal average of the radial velocity  $u_r$ , normalized with the inner cylinder azimuthal velocity  $u_i$ , obtained from PIV for varying roughness patch sizes  $\tilde{s}$ . A positive value of  $u_r$  denotes outflow, while a negative value denotes inflow, with respect to the inner cylinder. It can be seen that the rolls are pinned by the roughness and their wavelength changes with  $\tilde{s}$ . The red and gray areas at the left side of each plot indicate the positions of the rough and smooth areas, respectively. Note that the typical grain size is  $k/d \approx 0.01$ . The gray shaded areas in the gap represent unexplored heights.

can be tuned within the range  $\tilde{\lambda} \in [0.94, 4.01]$  by an appropriate choice of  $\tilde{s}$ . The wavelengths described above were calculated by measuring the locations of two consecutive maximum and minimum values of  $\langle u_r \rangle_{t,\theta,r_{bulk}}$  along  $z$  which are closest to midheight. Here, the symbol  $\langle \cdot \rangle_{t,\theta,r_{bulk}}$  denotes average over time, the streamwise direction and the bulk region, i.e.  $(r_{bulk} - r_i)/d \in [0.3, 0.7]$ .

In addition, we observe that outflow regions are created in axial regions where the roughness is located; and conversely, inflow regions are created in the smooth areas. Note that this orientation of the secondary flows is opposite to what is found in other canonical systems (e.g. pipe flow and channel flow [188, 190, 181]), where one finds inflow regions above the rough patches and outflow region above the smooth patches. Another interesting observation is that because the driving is now from the BL rather than the bulk, the strength of the rolls change depending on the value of  $\tilde{s}$ , as evidenced by the magnitude of  $|u_r|$ . In order to explore this feature in more detail, we quantify the strength of the rolls with  $\tilde{u}_r' \equiv \sqrt{\langle (u_r/u_i)^2 \rangle_{t,\theta,r_{bulk},z_\lambda}}$  as a function of  $\tilde{s}$ . Here, the symbol  $\langle \cdot \rangle_{t,\theta,r_{bulk},z_\lambda}$  denotes an average over time, the streamwise direction, the bulk region, and the axial region that defines the wavelength of a single roll  $z_\lambda$ . In figure 5.7(c), we show  $\tilde{u}_r'$  as a function of  $\tilde{s}$ , where we observe that the strength of the rolls increases with decreasing  $\tilde{s}$  for  $\tilde{s} \in [0.93, 3.74]$ . However at  $\tilde{s} = 0.61$  the trend is broken, where we observe that  $\tilde{u}_r'$  decreases with respect to the case of  $\tilde{s} = 0.93$ .

In order to obtain more insight into the mechanism(s) that lead to the varying  $\tilde{\lambda}$  for varying  $\tilde{s}$ , we turn to DNS, albeit at a much lower Ta ( $\approx 1.0 \times 10^9$ ), and much higher roughness height ( $k/d \approx 0.1$ ). Since very large  $\tilde{s}$  cases are not feasible for DNS, we focus on matching the exact  $\tilde{s}$  in the lower range. We will show that, despite the  $O(10^3)$  difference in Ta, the same observations found in the numerics are also found in the experiments.

First, we look at the azimuthal velocity component. In figure 5.5, we plot the difference of the temporal and azimuthal average of the angular velocity  $\langle \omega^+ \rangle_{t,\theta}$  with respect to the temporal, azimuthal and, axial average of the angular velocity  $\langle \omega^+ \rangle_{t,\theta,z}$  in wall units. This is done to emphasize the underlying organization of the TTVs. Here, we clearly observe that for all  $\tilde{s}$ , ejecting regions of angular velocity are originated in the rough patches, similar to the preferential plume ejection sides at the tips of grooves in Ref. [201]. These ejecting regions advect fluid from the roughness patch on or at the inner cylinder towards the outer cylinder. As a consequence, an array of plume-like structures are formed along the axial direction. In TC flow (without roughness), plume-like structures are clear signatures of the

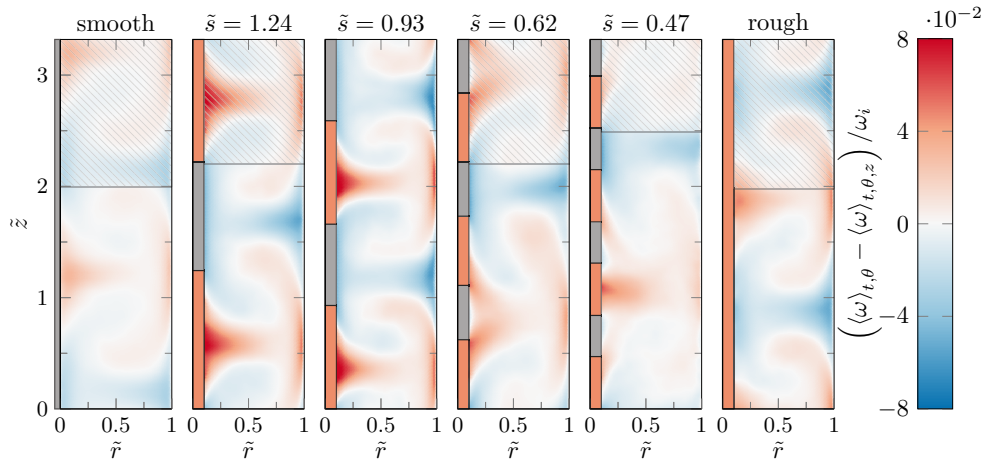


Figure 5.5: Deviation of the temporal and azimuthally averaged angular velocity  $\langle \omega \rangle_{t,\theta}$  with respect to the temporal, azimuthal, and axial averaged angular velocity  $\langle \omega \rangle_{t,\theta,z}$  obtained from DNS at  $Ta \approx 1.0 \times 10^9$ , and for all  $\tilde{s}$  explored in DNS. The fields are normalized with the inner angular velocity  $\omega_i = u_i/r_i$ . Positive values represent velocities that are closer to the IC velocity. The leftmost panel corresponds to the case of no roughness while the rightmost panel is the case where the entire IC is uniformly rough. Hatched regions are copied from the actual numerical domains—which are periodic in the axial direction—to allow for straightforward comparison. Ejecting regions can be seen in axial locations where the roughness is present. Notice the similarity of the structures with those found in the experiments shown in figure 6.

presence of TTVs [138, 103]. A closer inspection of figure 5.5 reveals that for the largest value of  $\tilde{s} = 1.24$ , the plumes have enough separation such as not to interact between them. When  $\tilde{s}$  is lowered to  $\tilde{s} = 0.93$ , we observe that the plumes come closer, and can, in fact, begin to interact with each other. At the lower  $\tilde{s} = 0.62$  however, the situation is rather different. Here, one rough patch does not create a single plume as for the previous cases; a plume is created from the interaction of two ejecting regions. For the  $\tilde{s} = 0.47$  case, we observe finally that a plume-like structure is originated from three different rough patches. The behavior of the plumes for  $\tilde{s} = 0.62$ , and  $\tilde{s} = 0.47$  is the result of the merging of the plumes that arise from the roughness patches. These observations help us to rationalize the change in the wavelength and strength of the rolls shown in figure 5.4. If  $\tilde{s}$  decreases, the plumes are effectively forced to come closer to each other; and as a result, the roll changes its wavelength and becomes stronger due to the added interaction of the plumes. In figure 5.6 we show  $(\langle \omega \rangle_{t,\theta} - \langle \omega \rangle_{t,\theta,z})/\omega_i$ , the same quantity discussed previously, albeit now for the experiments. Here, we can clearly see that a similar mechanism takes place. Plume-like structures are originated at the centers of the roughness elements and interact with each other if the spacing (small  $\tilde{s}$ ) is reduced.

The LDA, PIV and DNS explored in this section reveal that there is a mean effect of the spanwise-varying roughness on the large scale secondary flows that exist in turbulent TC flow. We have seen thus far that the roughness pins the rolls, and that their wavelength and strength can be tuned depending of the choice of  $\tilde{s}$  over a wide range of  $Ta$ , and a wide range of roughness heights  $h$ . However, how does the flow respond globally, i.e. the angular momentum transport, to this change in morphology? This will be addressed in the following section.

### 5.3.2 Global response

The global response of the TC system can be expressed with the  $Nu_\omega$  (5.2). In figure 5.7(a), we show the compensated Nusselt number as a function of the driving, where a scaling of  $Nu_\omega \propto Ta^\alpha$ , with  $\alpha = 0.45$  is revealed for all the  $\tilde{s}$  explored; except for  $\tilde{s} = 1.87$ , where the scaling is closer to  $\alpha = 0.44$ . In the absence of roughness and within the same range of  $Ta$ , the scaling is found to be effectively  $Nu_\omega \propto Ta^{0.40}$  [62, 63, 69]. In contrast, when both of the solid walls are made uniformly rough (i.e. pressure drag dominates),

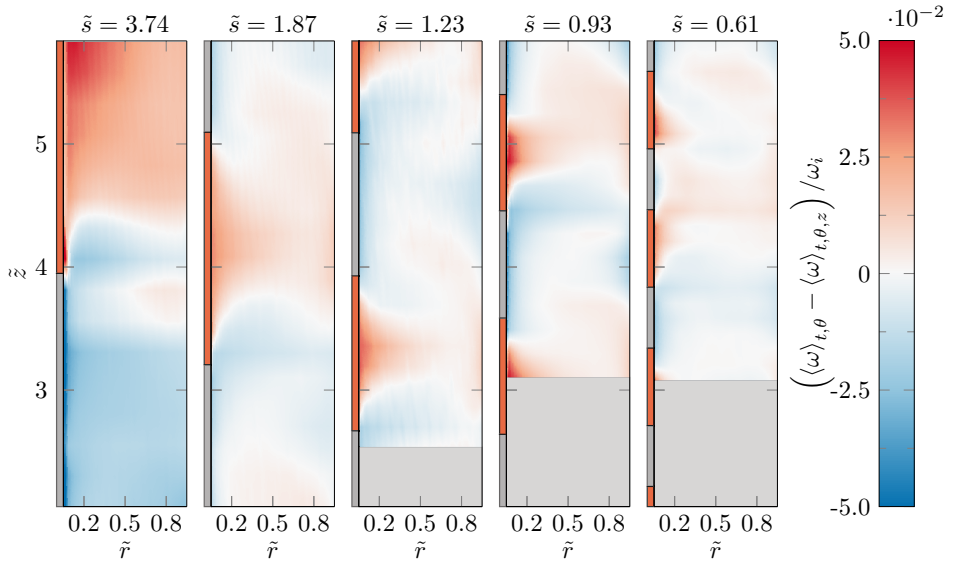


Figure 5.6: Deviation of the temporal, and azimuthal averaged angular velocity  $\langle \omega \rangle_{t,\theta}$  with respect to the temporal, azimuthal, and axial averaged angular velocity  $\langle \omega \rangle_{t,\theta,z}$  obtained from the experiments at  $Ta = 9.5 \times 10^{11}$ , and for all  $\tilde{s}$  explored in experiments. The fields are normalized with the inner angular velocity  $\omega_i = u_i/r_i$ . Ejecting regions can be seen in axial locations where the roughness is present. Notice the similarity of the structures with those found in the numerics shown in figure 5.

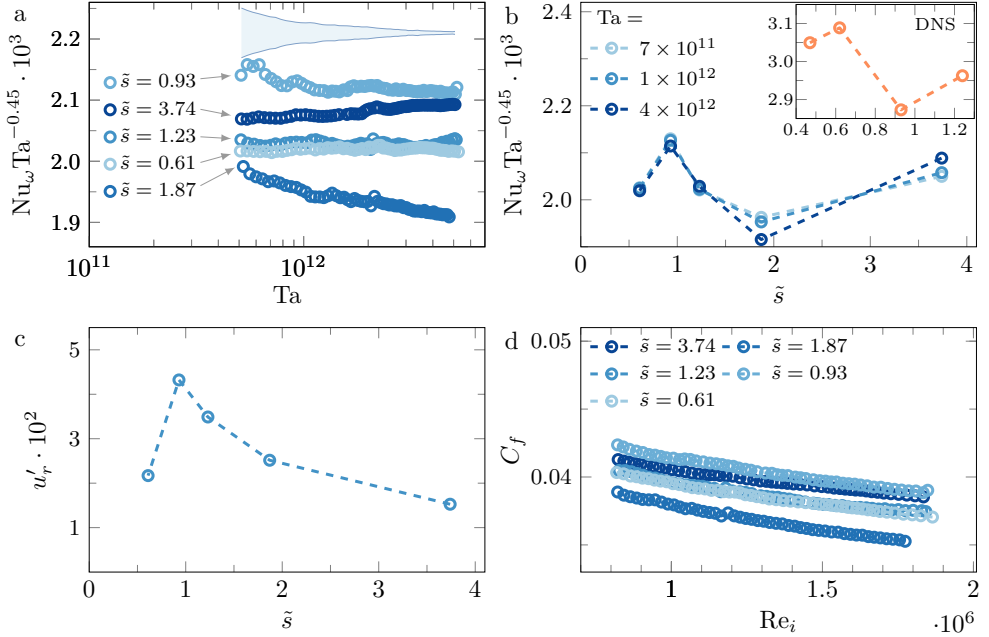


Figure 5.7: (a) Compensated Nusselt number  $\text{Nu}_\omega \text{Ta}^{-0.45}$  as a function of  $\text{Ta}$  for varying  $\tilde{s}$ . The shaded area indicates the error of the measurements, which can be seen to decrease with increasing driving. (b) Compensated Nusselt number  $\text{Nu}_\omega \text{Ta}^{-0.45}$  as a function of  $\tilde{s}$  for 3 selected  $\text{Ta}$ . Here, an optimum value in the transport of angular momentum is observed close to  $s/d \approx 1$ . The inset in (b) shows the results obtained with the DNS, where the maximum can be observed at a lower  $\tilde{s}$ , namely  $\tilde{s} \approx 0.6$ . (c) Normalized RMS of the radial velocity  $u'_r$  as a function of  $\tilde{s}$ , obtained from the PIV experiments. (d) Friction coefficient  $C_f$  as a function of the driving, expressed with the Reynolds number  $\text{Re}_i$ , for various  $\tilde{s}$ .

the scaling asymptotes to the ultimate regime scaling famously predicted by Kraichnan, *i.e.*  $\text{Nu}_\omega \propto \text{Ta}^{0.5}$  [193, 202]. In [202], the closest configuration to our study is the case of rough IC and smooth OC, for which the exponent  $\alpha = 0.43$  is found. We note that this exponent is somewhat smaller than the ones observed in the current study. The reason behind this, is currently unknown. We notice, however, that the roughness type in our study is rather different. In this study we use spanwise-varying sandgrain roughness, while the roughness in Ref. [202] is made of rib obstacles and is oriented along the streamwise direction.

In order to connect the observed dynamics of the TTVs with the global response, we plot in figure 5.7(b), the compensated Nusselt number  $\text{Nu}_\omega \text{Ta}^{-0.45}$  as a function of  $\tilde{s}$  for both the experiments and the numerics. We note that that the exponent found for  $\tilde{s} = 1.87$  ( $\alpha = 0.44$ ) is nearly the same as  $\alpha = 0.45$ . We see rather remarkably, the appearance of a maximum around  $\tilde{s} \approx 0.93$  for the experiments, and  $\tilde{s} = 0.61$  for the DNS. We attribute the appearance of this peak to the strengthening of the TTVs, which is caused by the variation of  $\tilde{s}$ , and thus of  $\tilde{\lambda}$ . Explicitly, by lowering  $\tilde{s}$ , we can lower the wavelength of the rolls and bring them closer together (see section 5.3.1). As a consequence, the rolls are strengthened which leads to an enhancement of the angular momentum transport; and thus, the peak around  $\tilde{s} = 0.93$ . This occurrence is also observed by Ref. [69], although the mechanism observed there is quite different. While the rolls in their study are enhanced by counter-rotating the OC; in our case, the rolls are strengthened by forcing  $\tilde{s}$  below their natural wavelength due to the right choice of the spanwise varying roughness. This is also supported by the observation that the magnitude of the radial velocity shows a maximum around  $\tilde{s} = 0.93$ , as shown in figure 5.7(c). We note, however, that the torque is not measured throughout the entire axial length of the cylinders  $L = 927$  mm, but in a smaller section of length  $L_{\text{mid}} = 536$  mm. As a result, the large structure identified previously for the case of  $\tilde{s} = 3.74$  ( $\tilde{\lambda} = 4.01$ ), does not fit entirely in the measurement section (see the first panel of figure 5.4). As a result, the Nusselt number that corresponds to this case, could be under or overestimated.

We also note that in the case of the numerics, the position of the maximum is different than in the experiments. We attribute this to a combination of two effects. On the one hand the DNS is performed at a lower  $\text{Ta}$ , which has an effect on the natural wavelength of the rolls as it was shown by Ref. [196], who show that for similar values of  $\eta$ , the wavelength of

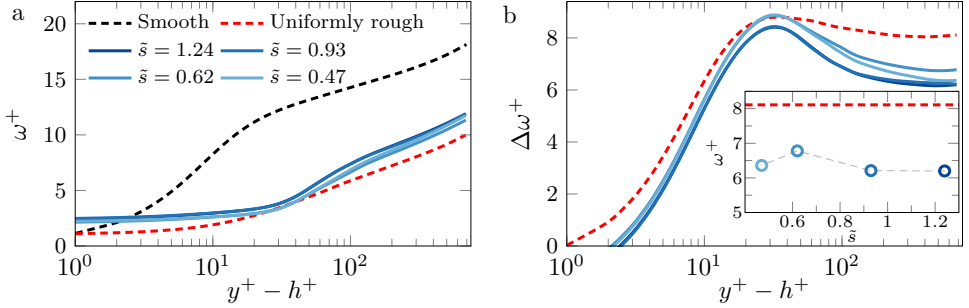


Figure 5.8: (a) Angular velocity  $\omega^+$  profiles versus the wall normal distance  $y^+ - h_m^+$  for various  $\tilde{s}$ , where  $h_m^+$  is the virtual origin and equals the melt-down (i.e. mean) height of the rough surface. The solid black line represents the uniformly rough case. (b) Angular velocity shift  $\Delta\omega^+$  as a function of  $y^+ - h^+$  for varying  $\tilde{s}$ . In the inset of (b), we show the angular velocity shift  $\Delta\omega^+$  versus the wall normal distance  $y^+ - h_m^+$ . Here, we observe a maximum downwards shift of the angular velocity profile for the simulation where we cover the entire inner cylinder with sandpaper roughness (i.e. uniformly rough).

the rolls can decrease with decreasing  $Ta$ . On the other hand, the axial domain of the DNS is bounded by  $\Gamma \in [2.08, 3.32]$ , which gives rise to limited box-sizes. Thus, when  $\tilde{s}$  is varied, the rolls could suffer from an additional *constraint* due to the limited axial domain. In addition to this discrepancy, we also note that the scaling in the range of  $Ta$  at which the DNS is done ( $\approx 1.0 \times 10^9$ ), is not known a priori. Since no other exponent is presently available to us, we chose to compensate the numerical data with the same exponent found in the experiments (figure 5.7(b)). However, we note that this exponent might be different due to the 2 decades of separation in  $Ta$  between the numerics and experiments, as was also shown by Ref. [202]. We would like to emphasize, however, that in spite of these discrepancies, a maximum in angular momentum transport is observed for a given  $\tilde{s}$  in both the experiments and the numerics, which is solely a consequence of the varying axial wavelength of the TTV, dictated by the spanwise-varying roughness.

### 5.3.3 Velocity profiles

Having discussed the dynamics of the TTVs and the corresponding global response, in terms of the dimensionless torque, we now set out to study the

streamwise, angular, velocity profiles (rather than the azimuthal profiles, as discussed in [209] and [203]). To allow for straightforward comparison between the respective velocity profiles, we run the DNS at constant friction Reynolds number  $Re_\tau = 690 \pm 10$ . The profiles are then temporally, azimuthally, and axially averaged  $\omega^+ = \langle \omega \rangle_{t,\theta,z} / \omega_\tau$ . The profiles still exhibit a logarithmic region when averaged over the entire axial coordinate. figure 5.5 shows however that the TTVs in the flow, following the spanwise-varying roughness, do not exhibit any outer similarity. Deviations of the azimuthal and temporal averages from the mean logarithmic profiles are found up to  $\Delta\omega^+ \approx 2$ .

For turbulent flows over rough walls, the streamwise velocity profiles retains its logarithmic form. However, the hallmark effect of rough walls is a downwards shift of this region (for any drag increasing surface), which can also be understood as an increase of the skin friction factor  $C_f$  [210]. Figure 5.8(a) shows the angular velocity profiles  $\omega^+$  as a function of  $(y^+ - h_m^+)$ , where  $h_m^+$  is the virtual origin and equals the melt-down (i.e. mean) height of the rough surface. We choose the melt-down height of the roughness over the full inner cylinder as the virtual origin. In figure 5.8(b) we show the velocity shift versus the wall normal distance. The inset gives a vertical cut at  $y^+ = Re_\tau$ . It is evident that also in this representation, an optimum in the velocity shift, and thus in  $C_f$  can be observed. The position of this maximum ( $\tilde{s} = 0.61$ ) is the same as the one obtained from the angular momentum transport (see section 5.3.2).

## 5.4 Conclusions and outlook

In this study, we investigate, both numerically and experimentally, large Taylor number Taylor–Couette flow in the presence of spanwise-varying roughness, which consists of an arrangement of patches of width  $\tilde{s} = s/d$ , with  $d$  the gap width, that covers the entire circumference of the inner cylinder. In the experiments, the patches are made from sandpaper, while in the numerics a confocal microscopy scan of the surface is implemented by means of the immersed boundary method (IBM).

Remarkably, we find that by varying  $\tilde{s}$  in the domain  $\tilde{s} = [0.61, 3.74]$  we can alter the axial wavelength of the turbulent Taylor vortices within the range  $\tilde{\lambda} \in [0.94, 4.01]$ , even if the roughness height is very low ( $k/d \approx 0.01$ ). This manipulation is observed to hold in a range of 3 decades in Ta ( $\mathcal{O}(10^9)$ ) –

$\mathcal{O}(10^{12})$ .

In the experiments, the scaling of the Nusselt number with the driving is found to be effectively  $\text{Nu}_\omega \propto \text{Ta}^{0.45}$  for  $\text{Ta} \in [5 \times 10^{11}, 5 \times 10^{12}]$ ; except for  $\tilde{s} = 1.87$ , where a very similar exponent is found ( $\alpha = 0.44$ ). The experiments also revealed that inflow regions ( $u_r < 0$ ) originate between the rough patches, where the inner cylinder is hydrodynamically smooth (in contrast to secondary flows induced by spanwise-varying roughness in channel flow, where the orientation of the vortices is reversed [181]. Conversely, at the center of the rough patches, we observe the creation of outflow regions ( $u_r > 0$ ) which are accompanied by the promotion of azimuthal velocity fluctuations  $\sigma(u_\theta)$  at midgap. At these axial locations (center of rough patches), we observe, in both the numerics and experiments, the emission of plume-like structures, which are responsible for the creation and pinning of the rolls. Since the coverage of the roughness is fixed, we show that by reducing  $\tilde{s}$ , we can effectively bring these structures closer, and enhance the interaction of the rolls, as evidenced by the increment in  $|u_r|$ . As a consequence of this interaction, the flow responds globally by inducing a maximum of angular momentum transport at  $\tilde{s} = 0.93$  in the experiments, and  $\tilde{s} = 0.62$  in the numerics.

We highlight that in this study, the change in the morphology of the large-scale structures is only due to the spanwise-varying roughness (of very low height) and not by a change of  $\Gamma$  or  $\eta$ , which opens the possibility of exploring different configurations in which the rolls can be tuned at such large turbulence levels.

Many questions arise from the aforementioned observations. Understanding the mechanisms leading to the merging of plume ejection regions, and accompanied parameter boundaries at which this occurs, would lead to a further insight into the dynamics of the TTVs. Furthermore, it would be intriguing, in the spirit of Ref. [211], to study the influence of spanwise-varying regions of idealized high and low wall shear stress, without geometrical induced disturbances. It is an open question whether one could also alter  $\lambda$ , without the interaction of the plumes.

## Conclusions

In this thesis we investigated turbulent flows with inclusions, *i.e.* a flow with bubbles, droplets, or solids dispersed in the continuous phase, and the influence of inhomogeneous boundaries on a turbulent flow. This was done experimentally using a Taylor–Couette apparatus (chapters 1–3 and 5) and using direct numerical simulations of Taylor–Couette flow and Rayleigh–Bénard convection (chapters 4 and 5). The findings of each chapter are discussed below.

In chapter 1 we have performed torque measurements for flows containing rigid spherical neutrally buoyant particles. Using particles of various sizes and quantities, we isolated the effect of size and volume fraction on the drag of a rotating cylinder. We showed that, unlike bubbles, rigid particles barely alter the drag of the system, even for cases where their size was comparable to that of the bubbles. For the sizes 1.5–8 mm, tested in this thesis, the size effect was marginal, with a slightly larger effect for the smallest particles. When increasing the volume fraction of the particles, there is a modest change in drag, but smaller than can be explained with the apparent viscosity of the suspension. The particles cannot be perfectly matched with the density of fluid and therefore, density effects might apply. By marginal variations in density of the working fluid, we found that there was a small but noticeable trend towards drag reduction for lower values of the particle to fluid density ratio  $\phi$ . This suggests that a low density of the particle could be a necessary ingredient for drag reduction. The local flow was probed using laser Doppler anemometry at the center of the gap. With addition of the particles, the fluctuations of the fluid flow were enhanced, with wider tails of the velocity probability distributions. This is generally seen when the relative velocity of the fluid and the particle is large, which is plausible due to the inertia of the particle. These fluctuations increase with decreasing particle size or increasing volume fraction, especially when we measure closer to the inner cylinder.

In the first chapter the size of the particles changed while the shape was fixed to a sphere. To investigate the shape effect of particles, in chapter 2 we

used fiber-like particles. Due to the anisotropic shape, the underlying flow is influenced by the orientation of the fiber, and vice versa, the orientation and translation of the fiber is also affected by the flow. By using high-speed imaging, we captured both, the orientation and position of the particle, as function of time. These fibers, despite their large size, follow the flow almost like faithful tracers. We explain this by comparing the turbulent dynamic time at the scale of the fiber length to the non-linear drag at the finite Reynolds number of the fiber, which can be expressed as a Stokes number. The Stokes number is only marginally above unity and therefore, these fibers show limited inertial effects. It was often hypothesized that a systematic alignment is not possible in highly turbulent systems. Surprisingly, we found a preferential alignment of  $-0.38\pi \pm 0.05\pi$  with respect to the inner cylinder wall. The least probable orientation has a probability which is approximately 40 % lower as compared to the most probable one. This alignment is persistent for all Reynolds numbers and volume fractions tested in this chapter. Measurements at various heights validated that this effect is not due to the secondary flows generally present in Taylor–Couette flow. We model the fiber orientation statistics using Jeffery’s equations, which provides a fair estimate of the shape of the alignment PDFs. The high-speed imaging also gave access to the rotation rates of the fibers, which was on average in the opposite direction as the IC. The fibers showed extreme intermittent rotation rates that are an order of magnitude larger than the inner cylinder rotation. In a number of ways, these finite-sized fibers behave remarkable similar to tiny particles in turbulence.

In chapter 3 we combined two immiscible fluids, in our case water and silicone oil, in our highly turbulent apparatus using volume fractions between 0–100 %. Due to the tremendous amount of shear, especially close to the boundaries, these immiscible fluids transform into a meta-stable emulsion. We did not use an emulsifier or surfactant and therefore, the energy-input from the turbulence provides the energy to continuously break up droplets. Removing this energy-input by turning off the system, will make this mixture separate in an instant. By exploiting the known scaling of the ultimate regime of Taylor–Couette flow, we calculated an effective viscosity,  $\nu_{\text{eff}}$  for the emulsion, which is generally not possible in conventional rheometers as the mixture would separate in an instant. Starting from pure water,  $\nu_{\text{eff}}$  increases with increasing oil volume fraction until the critical volume fraction for phase inversion has reached. Here, the rheological properties of the mixture change in an instant as we observe *catastrophic*

phase inversion. Before the inversion, we have oil droplets in water and  $\nu_{\text{eff}}$  is about three times the viscosity of water. The morphology changes to water droplets in oil after the inversion, where  $\nu_{\text{eff}}$  drops to half the viscosity of water (lower viscosity than each of the two phases), resulting in drag reduction. When performing dynamic measurements and therefore, change the oil volume fraction quasi-statically during the experiment, we observe an ambivalence region. In this ambivalence region, both morphologies are possible, depending on the history and the amount of shear applied. Using an in-situ microscopy setup, we were able to measure the droplet size in the ambivalence region for each morphology, which revealed that water droplets in oil are  $14\times$  larger in equivalent diameter than oil droplets in water. Larger droplets can deform easier and therefore, we expect a similar drag reduction mechanism as with bubbly drag reduction.

In chapter 4 we use direct numerical simulations to investigate the effect of inhomogeneous boundary conditions on Rayleigh-Bénard convection. We first applied a striped pattern of insulating and conducting areas on the top boundary. The area of the insulating and conducting areas are kept constant. Only the arrangement of the areas is varied by alternating conducting and insulating areas in stripes using various spatial frequencies. In the extreme case, where we only have one conducting and one insulating stripe, the top plate was practically half as effective, reducing the total heat transport to two third of the fully conducting case. Now changing the arrangement by increasing the amount of stripe pairs, the transport of heat also increase. At the largest stripe frequency, the heat transfer is very similar to the fully conducting case, even if half of the top plate is insulating. Extending the pattern two both sides results in similar results, however with the lowest frequency, the system transfers heat only half as effective as a fully conducting case. Using a two-dimensional Fourier analysis in the horizontal plane, we are able to see the imprint of the boundary condition pattern in the flow close to the boundary wall. The strength of this imprint does however decrease when we repeat this analysis further away from the wall. Outside of the thermal boundary layer, the imprint is indistinguishable and the bulk flow is only exposed to an effective boundary. Remarkably, even for the most extreme case with one large conducting and insulating region, the imprint is not visible outside the thermal boundary layer. The results from this chapter demonstrate that small and even larger imperfections in the temperature boundary conditions are barely felt in the system dynamics.

In chapter 5, we create an inhomogeneous boundary at the inner cylinder wall of the Taylor–Couette apparatus using p36 industrial-grade ceramic sandpaper. In the same spirit as chapter 4, we created bands of rough and smooth areas in the axial direction, and defined a roughness width  $\tilde{s}$ . When varying the size of the roughness bands, we found that we can control the positions of the secondary flows, *i.e.* the vortical structures, and force to have *more* or *less* rolls in the flow. Reducing the size of  $\tilde{s}$  below a critical value, shows that the individual patches do not induce single secondary flow, but create a collective outflow, resulting in less rolls. While the rough areas enhance the mixing and outflow, if the pattern becomes too small (small  $\tilde{s}$ ), the bulk flow only feels a boundary with an effective average roughness. From the torque measurements, we have revealed that there is an optimal value for  $\tilde{s}$  such that the angular momentum transport is enhanced. These findings are confirmed not only for experiments, but also for simulations at lower Taylor numbers. This is, to our knowledge, the first time that the secondary flows could be actively controlled in a Taylor–Couette flow.

## Bibliography

- [1] P. K. Kundu, I. M. Cohen, and D. Dowling, *Fluid Mechanics* (Elsevier) (2008).
- [2] V. Spandan, R. Verzicco, and D. Lohse, “Physical mechanisms governing drag reduction in turbulent Taylor–Couette flow with finite-size deformable bubbles”, *J. Fluid Mech.* **849**, R3 (2018).
- [3] United States Environmental Protection Agency, “Global trade and fuels assessment — additional eca modeling scenarios”, Technical Report, United States Environmental Protection Agency (2012).
- [4] M. P. Schultz, J. A. Bendick, E. R. Holm, and W. M. Hertel, “Economic impact of biofouling on a naval surface ship”, *Biofouling* **27**, 87–98 (2010).
- [5] R. A. Verschoof, D. Bakhuis, P. A. Bullee, S. G. Huisman, C. Sun, and D. Lohse, “Air cavities at the inner cylinder of turbulent Taylor–Couette flow”, *Int. J. Multiph. Flow* **105**, 264–273 (2018).
- [6] M. E. McCormick and R. Bhattacharyya, “Drag reduction of a submersible hull by electrolysis”, *Nav. Eng. J.* **85**, 11–16 (1973).
- [7] Y. Murai, “Frictional drag reduction by bubble injection”, *Exp. Fluids* **55**, 1773 (2014).
- [8] F. H. Busse, “The twins of turbulence research”, *Physics* **5** (2012).
- [9] S. Grossmann, D. Lohse, and C. Sun, “[High–Reynolds Number Taylor–Couette Turbulence]”, *Annu. Rev. Fluid Mech.* **48**, 53–80 (2016).
- [10] D. Lohse and K.-Q. Xia, “Small-Scale Properties of Turbulent Rayleigh–Bénard Convection”, *Annu. Rev. Fluid Mech.* **42**, 335–364 (2010).

- [11] B. Eckhardt, S. Grossmann, and D. Lohse, “What Rayleigh-Benard, Taylor-Couette and Pipe Flows Have in Common”, *Nonl. Phen. Compl. Sys.* **9**, 109–114 (2006).
- [12] B. Eckhardt, S. Grossmann, and D. Lohse, “Torque scaling in turbulent Taylor–Couette flow between independently rotating cylinders”, *J. Fluid Mech.* **581**, 221–250 (2007).
- [13] F. Toschi and E. Bodenschatz, “Lagrangian Properties of Particles in Turbulence”, *Annu. Rev. Fluid Mech.* **41**, 375–404 (2009).
- [14] S. Elghobashi, “On predicting particle-laden turbulent flows”, *Appl. Sci. Res.* **52**, 309–329 (1994).
- [15] I. M. Mazzitelli, D. Lohse, and F. Toschi, “The effect of microbubbles on developed turbulence”, *Phys. Fluids* **15**, L5 (2003).
- [16] V. Mathai, E. Calzavarini, J. Brons, C. Sun, and D. Lohse, “Microbubbles and Microparticles are Not Faithful Tracers of Turbulent Acceleration”, *Phys. Rev. Lett.* **117**, 024501 (2016).
- [17] M. Uhlmann, “Interface-resolved direct numerical simulation of vertical particulate channel flow in the turbulent regime”, *Phys. Fluids* **20**, 053305 (2008).
- [18] C. S. Peskin, “The immersed boundary method”, *Acta numer.* **11**, 479–517 (2002).
- [19] M. Cisse, H. Homann, and J. Bec, “Slipping motion of large neutrally buoyant particles in turbulence”, *J. Fluid Mech.* **735**, R1 (2013).
- [20] A. Naso and A. Prosperetti, “The interaction between a solid particle and a turbulent flow”, *New J. Phys.* **12**, 033040 (2010).
- [21] Y. Wang, A. J. Sierakowski, and A. Prosperetti, “Fully-resolved simulation of particulate flows with particles–fluid heat transfer”, *J. Comput. Phys.* **350**, 638–656 (2017).
- [22] S. O. Unverdi and G. Tryggvason, “A front-tracking method for viscous, incompressible, multi-fluid flows”, *J. Comput. Phys.* **100**, 25–37 (1992).
- [23] I. Roghair, J. Martínez Mercado, M. van Sint Annaland, H. Kuipers, C. Sun, and D. Lohse, “Energy spectra and bubble velocity distributions

- in pseudo-turbulence: Numerical simulations vs. experiments”, Int. J. Multiph. Flow **37**, 1093–1098 (2011).
- [24] Y. Tagawa, I. Roghair, V. N. Prakash, M. van Sint Annaland, H. Kuipers, C. Sun, and D. Lohse, “The clustering morphology of freely rising deformable bubbles”, J. Fluid Mech. **721**, R2 (2013).
  - [25] Y. Pan and S. Banerjee, “Numerical simulation of particle interactions with wall turbulence”, Phys. Fluids **8**, 2733 (1996).
  - [26] J. Lu, A. Fernández, and G. Tryggvason, “The effect of bubbles on the wall drag in a turbulent channel flow”, Phys. Fluids **17**, 095102 (2005).
  - [27] S. Dabiri, J. Lu, and G. Tryggvason, “Transition between regimes of a vertical channel bubbly upflow due to bubble deformability”, Phys. Fluids **25**, 102110 (2013).
  - [28] A. G. Kidanemariam, C. Chan-Braun, T. Doychev, and M. Uhlmann, “Direct numerical simulation of horizontal open channel flow with finite-size, heavy particles at low solid volume fraction”, New J. Phys. **15**, 025031 (2013).
  - [29] I. Lashgari, F. Picano, W.-P. Breugem, and L. Brandt, “Laminar, turbulent, and inertial shear-thickening regimes in channel flow of neutrally buoyant particle suspensions”, Phys. Rev. Lett. **113**, 254502 (2014).
  - [30] F. Picano, W.-P. Breugem, and L. Brandt, “Turbulent channel flow of dense suspensions of neutrally buoyant spheres”, J. Fluid Mech. **764**, 463–487 (2015).
  - [31] P. Costa, F. Picano, L. Brandt, and W.-P. Breugem, “Universal Scaling Laws for Dense Particle Suspensions in Turbulent Wall-Bounded Flows”, Phys. Rev. Lett. **117**, 134501 (2016).
  - [32] C. M. White and M. G. Mungal, “Mechanics and Prediction of Turbulent Drag Reduction with Polymer Additives”, Annu. Rev. Fluid Mech. **40**, 235–256 (2008).
  - [33] I. Procaccia, V. S. L’vov, and R. Benzi, “Colloquium: Theory of drag reduction by polymers in wall-bounded turbulence”, Rev. Mod. Phys. **80**, 225–247 (2008).

- [34] S. L. Ceccio, “Friction Drag Reduction of External Flows with Bubble and Gas Injection”, *Annu. Rev. Fluid Mech.* **42**, 183–203 (2010).
- [35] L. H. Zhao, H. I. Andersson, and J. J. J. Gillissen, “Turbulence modulation and drag reduction by spherical particles”, *Phys. Fluids* **22**, 081702 (2010).
- [36] M. Cisse, E.-W. Saw, M. Gibert, E. Bodenschatz, and J. Bec, “Turbulence attenuation by large neutrally buoyant particles”, *Phys. Fluids* **27**, 061702 (2015).
- [37] G. Bellani, M. L. Byron, A. G. Collignon, C. R. Meyer, and E. A. Variano, “Shape effects on turbulent modulation by large nearly neutrally buoyant particles”, *J. Fluid Mech.* **712**, 41–60 (2012).
- [38] N. Machicoane and R. Volk, “Lagrangian velocity and acceleration correlations of large inertial particles in a closed turbulent flow”, *Phys. Fluids* **28**, 035113 (2016).
- [39] C. Poelma, J. Westerweel, and G. Ooms, “Particle–fluid interactions in grid-generated turbulence”, *J. Fluid Mech.* **589**, 315–351 (2007).
- [40] A. Einstein, “Eine neue Bestimmung der Moleküldimensionen”, *Ann. d. Phys.* **324**, 289–306 (1906).
- [41] J. J. Stickel and R. L. Powell, “Fluid Mechanics and Rheology of Dense Suspensions”, *Annu. Rev. Fluid Mech.* **37**, 129–149 (2005).
- [42] T. J. Liu and S. G. Bankoff, “Structure of air-water bubbly flow in a vertical pipe—I. Liquid mean velocity and turbulence measurements”, *Int. J. Heat Mass Tran.* **36**, 1049–1060 (1993).
- [43] J. D. Kulick, J. R. Fessler, and J. K. Eaton, “Particle response and turbulence modification in fully developed channel flow”, *J. Fluid Mech.* **277**, 109–134 (1994).
- [44] M. Muste and V. C. Patel, “Velocity profiles for particles and liquid in open-channel flow with suspended sediment”, *J. Hydraul. Eng.* **123**, 742–751 (1997).
- [45] S. So, H. Morikita, S. Takagi, and Y. Matsumoto, “Laser Doppler velocimetry measurement of turbulent bubbly channel flow”, *Exp. Fluids* **33**, 135–142 (2002).

- [46] A. Fujiwara, D. Minato, and K. Hishida, “Effect of bubble diameter on modification of turbulence in an upward pipe flow”, *Int. J. Heat Fluid Fl.* **25**, 481–488 (2004).
- [47] T. H. van den Berg, S. Luther, D. P. Lathrop, and D. Lohse, “Drag Reduction in Bubbly Taylor-Couette Turbulence”, *Phys. Rev. Lett.* **94**, 044501 (2005).
- [48] T. H. van den Berg, D. P. M. van Gils, D. P. Lathrop, and D. Lohse, “Bubbly Turbulent Drag Reduction Is a Boundary Layer Effect”, *Phys. Rev. Lett.* **98**, 084501 (2007).
- [49] M. E. Shawkat, C. Y. Ching, and M. Shoukri, “Bubble and liquid turbulence characteristics of bubbly flow in a large diameter vertical pipe”, *Int. J. Multiph. Flow* **34**, 767–785 (2008).
- [50] E. Calzavarini, M. Cencini, D. Lohse, and F. Toschi, “Quantifying Turbulence-Induced Segregation of Inertial Particles”, *Phys. Rev. Lett.* **101**, 084504 (2008).
- [51] C. Colin, J. Fabre, and A. Kamp, “Turbulent bubbly flow in pipe under gravity and microgravity conditions”, *J. Fluid Mech.* **711**, 469–515 (2012).
- [52] D. P. van Gils, D. Narezo Guzman, C. Sun, and D. Lohse, “The importance of bubble deformability for strong drag reduction in bubbly turbulent Taylor–Couette flow”, *J. Fluid Mech.* **722**, 317–347 (2013).
- [53] R. Maryami, S. Farahat, M. Javad poor, and M. H. Shafiei Mayam, “Bubbly drag reduction in a vertical Couette–Taylor system with superimposed axial flow”, *Fluid Dyn. Res.* **46**, 055504 (2014).
- [54] V. Mathai, V. N. Prakash, J. Brons, C. Sun, and D. Lohse, “Wake-Driven Dynamics of Finite-Sized Buoyant Spheres in Turbulence”, *Phys. Rev. Lett.* **115**, 124501 (2015).
- [55] E. Almérás, V. Mathai, D. Lohse, and C. Sun, “Experimental investigation of the turbulence induced by a bubble swarm rising within incident turbulence”, *J. Fluid Mech.* **825**, 1091–1112 (2017).
- [56] V. Mathai, S. G. Huisman, C. Sun, D. Lohse, and M. Bourgoin, “Dispersion of Air Bubbles in Isotropic Turbulence”, *Phys. Rev. Lett.* **121**, 054501 (2018).

- [57] A. D. Bragg, P. J. Ireland, and L. R. Collins, “Mechanisms for the clustering of inertial particles in the inertial range of isotropic turbulence”, Phys. Rev. E **92**, 023029 (2015).
- [58] L. Fiabane, R. Zimmermann, R. Volk, J.-F. Pinton, and M. Bourgoin, “Clustering of finite-size particles in turbulence”, Phys. Rev. E **86**, 035301 (2012).
- [59] H. T. Kazerooni, W. Fornari, J. Hussong, and L. Brandt, “Inertial migration in dilute and semidilute suspensions of rigid particles in laminar square duct flow”, Phys. Fluids **2**, 084301 (2017).
- [60] D. P. Lathrop, J. Fineberg, and H. L. Swinney, “Turbulent flow between concentric rotating cylinders at large Reynolds number”, Phys. Rev. Lett. **68**, 1515 (1992).
- [61] G. S. Lewis and H. L. Swinney, “Velocity structure functions, scaling, and transitions in high-Reynolds-number Couette-Taylor flow”, Phys. Rev. E **59**, 5457 (1999).
- [62] M. S. Paoletti and D. P. Lathrop, “Angular Momentum Transport in Turbulent Flow between Independently Rotating Cylinders”, Phys. Rev. Lett. **106**, 024501 (2011).
- [63] D. P. van Gils, G.-W. Bruggert, D. P. Lathrop, C. Sun, and D. Lohse, “The Twente turbulent Taylor-Couette ( $t^3 c$ ) facility: strongly turbulent (multiphase) flow between independently rotating cylinders”, Rev. Sci. Instr. **82**, 025105 (2011).
- [64] R. Ostilla-Mónico, R. J. A. M. Stevens, S. Grossmann, R. Verzicco, and D. Lohse, “Optimal Taylor–Couette flow: direct numerical simulations”, J. Fluid Mech. **719**, 14–46 (2013).
- [65] M. A. Fardin, C. Perge, and N. Taberlet, ““The hydrogen atom of fluid dynamics“ - introduction to the Taylor–Couette flow for soft matter scientists”, Soft Matter **10**, 3523–3535 (2014).
- [66] R. A. Verschoof, R. C. van der Veen, C. Sun, and D. Lohse, “Bubble Drag Reduction Requires Large Bubbles”, Phys. Rev. Lett. **117**, 104502 (2016).
- [67] Glycerine Producers’ Association, *Physical properties of glycerine and its solutions* (Glycerine Producers’ Association) (1963).

- [68] S. G. Huisman, D. P. van Gils, and C. Sun, “Applying laser Doppler anemometry inside a Taylor–Couette geometry using a ray-tracer to correct for curvature effects”, *Eur. J. Mech. B-Fluids* **36**, 115–119 (2012).
- [69] S. G. Huisman, R. C. A. van der Veen, C. Sun, and D. Lohse, “Multiple states in highly turbulent Taylor–Couette flow”, *Nat. Comm.* **5**, 3820 (2014).
- [70] Y. Tsuji, Y. Morikawa, and H. Shiomi, “LDV measurements of an air–solid two-phase flow in a vertical pipe”, *J. Fluid Mech.* **139**, 417–434 (1984).
- [71] R. A. Gore and C. T. Crowe, “Effect of particle size on modulating turbulent intensity”, *Int. J. Multiph. Flow* **15**, 279–285 (1989).
- [72] A. W. Vreman, “Turbulence attenuation in particle-laden flow in smooth and rough channels”, *J. Fluid Mech.* **773**, 103–136 (2015).
- [73] S. G. Huisman, S. Scharnowski, C. Cierpka, C. J. Kähler, D. Lohse, and C. Sun, “Logarithmic Boundary Layers in Strong Taylor–Couette Turbulence”, *Phys. Rev. Lett.* **110**, 264501 (2013).
- [74] F. Lundell, L. D. Söderberg, and P. H. Alfredsson, “Fluid Mechanics of Papermaking”, *Annu. Rev. Fluid Mech.* **43**, 195–217 (2011).
- [75] L. Sabban, A. Cohen, and R. van Hout, “Temporally resolved measurements of heavy, rigid fibre translation and rotation in nearly homogeneous isotropic turbulence”, *J. Fluid Mech.* **814**, 42–68 (2017).
- [76] K. Vercruyse, R. C. Grabowski, and R. Rickson, “Suspended sediment transport dynamics in rivers: Multi-scale drivers of temporal variation”, *Earth-Sci. Rev.* **166**, 38–52 (2017).
- [77] J. E. Butler and B. Snook, “Microstructural Dynamics and Rheology of Suspensions of Rigid Fibers”, *Annu. Rev. Fluid Mech.* **50**, 299–318 (2018).
- [78] M. Daghooghi and I. Borazjani, “The influence of inertia on the rheology of a periodic suspension of neutrally buoyant rigid ellipsoids”, *J. Fluid Mech.* **781**, 506–549 (2015).
- [79] M. Wilkinson, V. Bezuglyy, and B. Mehlig, “Fingerprints of random flows?”, *Phys. Fluids* **21**, 043304 (2009).

- [80] S. Parsa, J. S. Guasto, M. Kishore, N. T. Ouellette, J. P. Gollub, and G. A. Voth, “Rotation and alignment of rods in two-dimensional chaotic flow”, *Phys. Fluids* **23**, 043302 (2011).
- [81] A. Pumir and M. Wilkinson, “Orientation statistics of small particles in turbulence”, *New. J. Phys.* **13**, 093030 (2011).
- [82] S. Parsa, E. Calzavarini, F. Toschi, and G. A. Voth, “Rotation Rate of Rods in Turbulent Fluid Flow”, *Phys. Rev. Lett.* **109**, 134501 (2012).
- [83] G. A. Voth and A. Soldati, “Anisotropic Particles in Turbulence”, *Annu. Rev. Fluid Mech.* **49**, 249–276 (2017).
- [84] D. Vincenzi, “Orientation of non-spherical particles in an axisymmetric random flow”, *J. Fluid Mech.* **719**, 465–487 (2013).
- [85] G. B. Jeffery, “The motion of ellipsoidal particles immersed in a viscous fluid”, *Proc. Royal Soc. A* **102**, 161–179 (1922).
- [86] P. Butler, “Shear induced structures and transformations in complex fluids”, *Curr. Opin. Colloid In.* **4**, 214–221 (1999).
- [87] H. Zhang, G. Ahmadi, F. Fan, and J. B. McLaughlin, “Ellipsoidal particles transport and deposition in turbulent channel flows”, *Int. J. Multiph. Flow* **27**, 971–1009 (2001).
- [88] P. H. Mortensen, H. I. Andersson, J. J. J. Gillissen, and B. J. Boersma, “Dynamics of prolate ellipsoidal particles in a turbulent channel flow”, *Phys. Fluids* **20**, 093302 (2008).
- [89] C. Marchioli, M. Fantoni, and A. Soldati, “Orientation, distribution, and deposition of elongated, inertial fibers in turbulent channel flow”, *Phys. Fluids* **22**, 033301 (2010).
- [90] C. Marchioli and A. Soldati, “Rotation statistics of fibers in wall shear turbulence”, *Acta Mech.* **224**, 2311–2329 (2013).
- [91] N. R. Challabotla, L. Zhao, and H. I. Andersson, “Orientation and rotation of inertial disk particles in wall turbulence”, *J. Fluid Mech.* **766**, R2 (2015).
- [92] F. Zhao, W. K. George, and B. G. M. van Wachem, “Four-way coupled simulations of small particles in turbulent channel flow: The effects of particle shape and Stokes number”, *Phys. Fluids* **27**, 083301 (2015).

- [93] L. Zhao, N. R. Challabotla, H. I. Andersson, and E. A. Variano, “Rotation of Nonspherical Particles in Turbulent Channel Flow”, *Phys. Rev. Lett.* **115**, 244501 (2015).
- [94] A. N. Kolmogorov, “The local structure of turbulence in incompressible viscous fluid for very large reynolds numbers”, *Dokl. Akad. Nauk. SSSR* **30**, 299–303 (1941).
- [95] A. N. Kolmogorov, “On degeneration of isotropic turbulence in an incompressible viscous liquid”, *Dokl. Akad. Nauk. SSSR* **31**, 538–540 (1941).
- [96] M. R. Maxey and J. J. Riley, “Equation of motion for a small rigid sphere in a nonuniform flow”, *Phys. Fluids* **26**, 883 (1983).
- [97] M. Do-Quang, G. Amberg, G. Brethouwer, and A. V. Johansson, “Simulation of finite-size fibers in turbulent channel flows”, *Phys. Rev. E* **89**, 013006 (2014).
- [98] E. Calzavarini, R. Volk, M. Bourgoin, E. Lévéque, J.-F. Pinton, and F. Toschi, “Acceleration statistics of finite-sized particles in turbulent flow: the role of Faxén forces”, *J. Fluid Mech.* **630**, 179–189 (2009).
- [99] J. Bec, L. Biferale, A. Lanotte, A. Scagliarini, and F. Toschi, “Turbulent pair dispersion of inertial particles”, *J. Fluid Mech.* **645**, 497–528 (2010).
- [100] G. Bellani and E. A. Variano, “Slip velocity of large neutrally buoyant particles in turbulent flows”, *new. J. Phys.* **14**, 125009 (2012).
- [101] D. Bakhuis, R. A. Verschoof, V. Mathai, S. G. Huisman, D. Lohse, and C. Sun, “Finite-sized rigid spheres in turbulent Taylor–Couette flow: effect on the overall drag”, *J. Fluid Mech.* **850**, 246–261 (2018).
- [102] S. G. Huisman, D. P. M. van Gils, S. Grossmann, C. Sun, and D. Lohse, “Ultimate turbulent Taylor–Couette flow”, *Phys. Rev. Lett.* **108**, 024501 (2012).
- [103] R. Ostilla-Mónico, E. P. van der Poel, R. Verzicco, S. Grossmann, and D. Lohse, “Exploring the phase diagram of fully turbulent Taylor–Couette flow”, *J. Fluid Mech.* **761**, 1–26 (2014).

- [104] N. M. Qureshi, M. Bourgoin, C. Baudet, A. Cartellier, and Y. Gagne, “Turbulent Transport of Material Particles: An Experimental Study of Finite Size Effects”, *Phys. Rev. Lett.* **99**, 184502 (2007).
- [105] H. Xu and E. Bodenschatz, “Motion of inertial particles with size larger than Kolmogorov scale in turbulent flows”, *Physica D* **237**, 2095–2100 (2008).
- [106] R. Clift, J. Grace, M. Weber, and M. Weber, *Bubbles, Drops, and Particles* (Academic Press) (1978).
- [107] R. C. A. van der Veen, S. G. Huisman, O.-Y. Dung, H. L. Tang, C. Sun, and D. Lohse, “Exploring the phase space of multiple states in highly turbulent taylor-couette flow”, *Phys. Rev. Fluids* **1**, 024401 (2016).
- [108] N. R. Challabotla, C. Nilsen, and H. I. Andersson, “On rotational dynamics of inertial disks in creeping shear flow”, *Phys. Lett. A* **379**, 157–162 (2015).
- [109] R. Zimmermann, Y. Gasteuil, M. Bourgoin, R. Volk, A. Pumir, and J.-F. Pinton, “Rotational Intermittency and Turbulence Induced Lift Experienced by Large Particles in a Turbulent Flow”, *Phys. Rev. Lett.* **106**, 154501 (2011).
- [110] V. Mathai, M. W. M. Neut, E. P. van der Poel, and C. Sun, “Translational and rotational dynamics of a large buoyant sphere in turbulence”, *Exp. Fluids* **57**, 51 (2016).
- [111] V. Mathai, X. Zhu, C. Sun, and D. Lohse, “Flutter to tumble transition of buoyant spheres triggered by rotational inertia changes”, *Nat. Commun.* **9**, 1792 (2018).
- [112] D. J. McClements, *Food emulsions: principles, practices, and techniques*, 2nd edition (CRC press) (2004).
- [113] P. Becher, *Emulsions: Theory and Practice* (Oxford University Press) (2001).
- [114] J.-L. Salager, L. Márquez, A. A. Peña, M. Rondón, F. Silva, and E. Tyrode, “Current Phenomenological Know-How and Modeling of Emulsion Inversion”, *Ind. Eng. Chem. Res.* **39**, 2665–2676 (2000).

- [115] A. Perazzo, V. Preziosi, and S. Guido, “Phase inversion emulsification: Current understanding and applications”, *Adv. Colloid Interface Sci.* **222**, 581–599 (2015).
- [116] R. Pal, “Pipeline flow of unstable and surfactant-stabilized emulsions”, *AIChE J.* **39**, 1754–1764 (1993).
- [117] F. Jahanzad, G. Crombie, R. Innes, and S. Sajjadi, “Catastrophic phase inversion via formation of multiple emulsions: A prerequisite for formation of fine emulsions”, *Chem. Eng. Res. Des.* **87**, 492–498 (2009).
- [118] P. Poesio and G. Beretta, “Minimal dissipation rate approach to correlate phase inversion data”, *Int. J. Multiph. Flow* **34**, 684–689 (2008).
- [119] K. H. Ngan, K. Ioannou, L. D. Rhyne, W. Wang, and P. Angeli, “A methodology for predicting phase inversion during liquid–liquid dispersed pipeline flow”, *Chem. Eng. Res. Des.* **87**, 318–324 (2009).
- [120] K. Piela, G. Ooms, and J. V. Sengers, “Phenomenological description of phase inversion”, *Phys. Rev. E* **79**, 021403 (2009).
- [121] N. Brauner and A. Ullmann, “Modeling of phase inversion phenomenon in two-phase pipe flows”, *Int. J. Multiph. Flow* **28**, 1177–1204 (2002).
- [122] L. Y. Yeo, O. K. Matar, E. Susana Perez de Ortiz, and G. F. Hewitt, “A description of phase inversion behaviour in agitated liquid–liquid dispersions under the influence of the Marangoni effect”, *Chem. Eng. Sci.* **57**, 3505–3520 (2002).
- [123] E. Dickinson, “Interpretation of emulsion phase inversion as a cusp catastrophe”, *J. Colloid Interface Sci.* **84**, 284–287 (1981).
- [124] G. E. J. Vaessen, M. Visschers, and H. N. Stein, “Predicting Catastrophic Phase Inversion on the Basis of Droplet Coalescence Kinetics”, *Langmuir* **12**, 875–882 (1996).
- [125] E. Tyrode, J. Allouche, L. Choplin, and J.-L. Salager, “Emulsion Catastrophic Inversion from Abnormal to Normal Morphology. 4. Following the Emulsion Viscosity during Three Inversion Protocols and Extending the Critical Dispersed-Phase Concept”, *Ind. Eng. Chem. Res.* **44**, 67–74 (2005).

- [126] K. Piela, R. Delfos, G. Ooms, J. Westerweel, R. Oliemans, and R. Mudde, “Experimental investigation of phase inversion in an oil–water flow through a horizontal pipe loop”, *Int. J. Multiph. Flow* **32**, 1087–1099 (2006).
- [127] H. Moradpour, A. Chapoy, and B. Tohidi, “Phase Inversion in Water–Oil Emulsions with and without Gas Hydrates”, *Energy Fuels* **25**, 5736–5745 (2011).
- [128] A. N. Kolmogorov, “On the breakage of drops in a turbulent flow”, *Dokl. Akad. Nauk. SSSR* **66**, 825–828 (1949).
- [129] J. O. Hinze, “Fundamentals of the hydrodynamic mechanism of splitting in dispersion processes”, *AIChE J.* **1**, 289–295 (1955).
- [130] R. Andersson and B. Andersson, “On the breakup of fluid particles in turbulent flows”, *AIChE J.* **52**, 2020–2030 (2006).
- [131] G. Zhou and S. M. Kresta, “Correlation of mean drop size and minimum drop size with the turbulence energy dissipation and the flow in an agitated tank”, *Chem. Eng. Sci.* **53**, 2063–2079 (1998).
- [132] R. Shinnar, “On the behaviour of liquid dispersions in mixing vessels”, *J. Fluid Mech.* **10**, 259–275 (1961).
- [133] J. A. Boxall, C. A. Koh, E. D. Sloan, A. K. Sum, and D. T. Wu, “Droplet Size Scaling of Water-in-Oil Emulsions under Turbulent Flow”, *Langmuir* **28**, 104–110 (2011).
- [134] S. R. Derkach, “Rheology of emulsions”, *Adv. Colloid Interface Sci.* **151**, 1–23 (2009).
- [135] *Shin-Etsu Silicone Oil KF-96-1cSt*.
- [136] A. G. Kanellopoulos and M. J. Owen, “Adsorption of sodium dodecyl sulphate at the silicone fluid/water interface”, *T. Faraday Soc.* **67**, 3127 (1971).
- [137] D. P. M. van Gils, S. G. Huisman, G.-W. Bruggert, C. Sun, and D. Lohse, “Torque Scaling in Turbulent Taylor-Couette Flow with Co- and Counterrotating Cylinders”, *Phys. Rev. Lett.* **106**, 024502 (2011).

- [138] R. Ostilla-Mónico, E. P. van der Poel, R. Verzicco, S. Grossmann, and D. Lohse, “Boundary layer dynamics at the transition between the classical and the ultimate regime of Taylor–Couette flow”, *Physics of Fluids* **26**, 015114 (2014).
- [139] R. Pal, “Effect of droplet size on the rheology of emulsions”, *AIChE J.* **42**, 3181–3190 (1996).
- [140] K. Piela, R. Delfos, G. Ooms, J. Westerweel, and R. Oliemans, “On the phase inversion process in an oil–water pipe flow”, *Int. J. Multiph. Flow* **34**, 665–677 (2008).
- [141] X. Zhu, R. Verzicco, and D. Lohse, “Disentangling the origins of torque enhancement through wall roughness in Taylor–Couette turbulence”, *J. Fluid Mech.* **812**, 279–293 (2017).
- [142] Y. Gu and D. Li, “The  $\zeta$ -Potential of Silicone Oil Droplets Dispersed in Aqueous Solutions”, *J. Colloid Interface Sci.* **206**, 346–349 (1998).
- [143] J. Eastoe and C. Ellis, “De-gassed water and surfactant-free emulsions: History, controversy, and possible applications”, *Adv. Colloid Interface Sci.* **134–135**, 89–95 (2007).
- [144] J. Marshall and F. Schott, “Open-ocean convection: Observations, theory, and models”, *Rev. Geophys.* **37**, 1–64 (1999).
- [145] A. Wirth and B. Barnier, “Tilted convective plumes in numerical experiments”, *Ocean Model.* **12**, 101–111 (2006).
- [146] D. P. McKenzie, J. M. Roberts, and N. O. Weiss, “Convection in the Earth’s mantle: towards a numerical simulation”, *J. Fluid Mech.* **62**, 465–538 (1974).
- [147] G. A. Glatzmaier and P. H. Roberts, “A 3-dimensional self-consistent computer simulation of a geomagnetic field reversal”, *Nature* **377**, 203–209 (1995).
- [148] E. A. Spiegel, “Convection in stars”, *Ann. Rev. Astron. Astrophys.* **9**, 323–352 (1971).
- [149] F. Cattaneo, T. Emonet, and N. Weiss, “On the interaction between convection and magnetic fields”, *Astrophys. J.* **588**, 1183–1198 (2003).

- [150] C. Normand, Y. Pomeau, and M. H. Velarde, “Convective instability: a physicist’s approach”, *Rev. Mod. Phy.* **49**, 465–538 (1977).
- [151] G. Ahlers, S. Grossmann, and D. Lohse, “Heat transfer and large scale dynamics in turbulent Rayleigh-Bénard convection”, *Rev. Mod. Phys.* **81**, 503–537 (2009).
- [152] F. Chillà and J. Schumacher, “New perspectives in turbulent Rayleigh-Bénard convection”, *Eur. Phys. J. E* **35**, 58 (2012).
- [153] S. Marcq and J. Weiss, “Influence of sea ice lead-width distribution on turbulent heat transfer between the ocean and the atmosphere”, *Cryosphere* **6**, 143–156 (2012).
- [154] A. Lenardic, L. N. Moresi, M. A. Jellinek, and M. Manga, “Continental insulation, mantle cooling and the surface area of oceans and continents”, *Earth Planet. Sci. Lett.* **234**, 317–333 (2005).
- [155] L. Zhao, X. Lee, R. B. Smith, and K. Oleson, “Strong contributions of local background climate to urban heat islands”, *Nature* **511**, 216–219 (2014).
- [156] H. Johnston and C. R. Doering, “Rayleigh-Bénard convection with imposed heat flux”, *Chaos* **17**, 041103 (2007).
- [157] H. Johnston and C. R. Doering, “Comparison of Turbulent Thermal Convection between Conditions of Constant Temperature and Constant Flux”, *Phys. Rev. Lett.* **102**, 064501 (2009).
- [158] R. J. A. M. Stevens, D. Lohse, and R. Verzicco, “Prandtl and Rayleigh number dependence of heat transport in high Rayleigh number thermal convection”, *J. Fluid Mech.* **688**, 31–43 (2011).
- [159] S.-D. Huang, F. Wang, H.-D. Xi, and K.-Q. Xia, “Comparative Experimental Study of Fixed Temperature and Fixed Heat Flux Boundary Conditions in Turbulent Thermal Convection”, *Phys. Rev. Lett.* **115**, 154502 (2015).
- [160] R. Verzicco, “Effect of non-perfect thermal sources in turbulent thermal convection”, *Phys. Fluids* **16**, 1965–1979 (2004).

- [161] R. E. Kelly and D. Pal, “Thermal convection with spatially periodic boundary conditions:resonant wavelength excitation”, *J. Fluid Mech.* **86**, 433–456 (1978).
- [162] J. S. Yoo and U. Moon, “Two-dimensional convection in a horizontal fluid layer with spatially periodic boundary temperatures”, *Fluid Dyn. Res.* **7**, 181–200 (1991).
- [163] X.-L. Jin and K.-Q. Xia, “An experimental study of kicked thermal turbulence”, *J. Fluid Mech.* **606**, 131–151 (2008).
- [164] F. Wang, S.-D. Huang, and K.-Q. Xia, “Thermal convection with mixed thermal boundary conditions: Effects of insulating lids at the top”, *J. Fluid Mech.* **817**, R1 (2017).
- [165] C. M. Cooper, L. N. Moresi, and A. Lenardic, “Effects of continental configuration on mantle heat loss”, *Geoph. Res. Lett.* **40**, 2647–2651 (2013).
- [166] P. Ripesi, L. Bigerale, M. Sbragaglia, and A. Wirth, “Natural convection with mixed insulating and conducting boundary conditions: low- and high-Rayleigh-number regimes”, *J. Fluid Mech.* **742**, 636–663 (2014).
- [167] R. Verzicco and P. Orlandi, “A finite-difference scheme for three-dimensional incompressible flow in cylindrical coordinates”, *J. Comput. Phys.* **123**, 402–413 (1996).
- [168] E. P. van der Poel, R. Ostilla-Mónico, J. Donners, and R. Verzicco, “A pencil distributed finite difference code for strongly turbulent wall-bounded flows”, *Comp. Fluids* **116**, 10–16 (2015).
- [169] R. J. A. M. Stevens, R. Verzicco, and D. Lohse, “Radial boundary layer structure and Nusselt number in Rayleigh-Bénard convection”, *J. Fluid Mech.* **643**, 495–507 (2010).
- [170] B. I. Shraiman and E. D. Siggia, “Heat transport in high-Rayleigh number convection”, *Phys. Rev. A* **42**, 3650–3653 (1990).
- [171] E. P. van der Poel, R. Ostilla-Mónico, R. Verzicco, and D. Lohse, “Effect of velocity boundary conditions on the heat transfer and flow topology in two-dimensional Rayleigh-Bénard convection”, *Phys. Rev. E* **90**, 013017 (2014).

- [172] J. C. Tisserand, M. Creyssels, Y. Gasteuil, H. Pabiou, M. Gibert, B. Castating, and F. Chilla, “Comparison between rough and smooth plates within the same Rayleigh-Bénard cell”, *Phys. Fluids* **23**, 015105 (2011).
- [173] J. A. Whitehead and M. D. Behn, “The continental drift convection cell”, *Geoph. Res. Lett.* **42**, 2015GL064480 (2015).
- [174] J. Jimenez, “Turbulent flows over rough walls”, *Annu. Rev. Fluid Mech.* **36**, 173–196 (2004).
- [175] A. A. R. Townsend, *The structure of turbulent shear flow* (Cambridge University Press) (1976).
- [176] K. A. Flack and M. P. Schultz, “Review of Hydraulic Roughness Scales in the Fully Rough Regime”, *J. Fluids Eng.* **132**, 041203 (2010).
- [177] M. P. Schultz, “Effects of coating roughness and biofouling on ship resistance and powering”, *Biofouling* **23**, 331–341 (2007).
- [178] H. Ren and Y. Wu, “Turbulent boundary layers over smooth and rough forward-facing steps”, *Phys. Fluids* **23**, 045102 (2011).
- [179] K. Koeltzsch, A. Dinkelacker, and R. Grundmann, “Flow over convergent and divergent wall ripples”, *Exp. Fluids* **33**, 346–350 (2002).
- [180] W. Anderson, J. M. Barros, K. T. Christensen, and A. Awasthi, “Numerical and experimental study of mechanisms responsible for turbulent secondary flows in boundary layer flows over spanwise heterogeneous roughness”, *J. Fluid Mech.* **768**, 316–347 (2015).
- [181] D. Chung, J. P. Monty, and N. Hutchins, “Similarity and structure of wall turbulence with lateral wall shear stress variations”, *J. Fluid Mech.* **847**, 591–613 (2018).
- [182] Z.-Q. Wang and N.-S. Cheng, “Time-mean structure of secondary flows in open channel with longitudinal bedforms”, *Adv. Water Resour.* **29**, 1634–1649 (2006).
- [183] J. O. Hinze, “Secondary Currents in Wall Turbulence”, *Phys. Fluids* **10**, S122 (1967).

- [184] J. O. Hinze, “Experimental investigation on secondary currents in the turbulent flow through a straight conduit”, *Appl. Sci. Res.* **28**, 453–465 (1973).
- [185] B. Nugroho, N. Hutchins, and J. Monty, “Large-scale spanwise periodicity in a turbulent boundary layer induced by highly ordered and directional surface roughness”, *Int. J. Heat Fluid Fl.* **41**, 90–102 (2013).
- [186] J. M. Barros and K. T. Christensen, “Observations of turbulent secondary flows in a rough-wall boundary layer”, *J. Fluid Mech.* **748**, R1 (2014).
- [187] R. Mejia-Alvarez and K. T. Christensen, “Wall-parallel stereo particle-image velocimetry measurements in the roughness sublayer of turbulent flow overlying highly irregular roughness”, *Phys. Fluids* **25**, 115109 (2013).
- [188] D. Willingham, W. Anderson, K. T. Christensen, and J. M. Barros, “Turbulent boundary layer flow over transverse aerodynamic roughness transitions: Induced mixing and flow characterization”, *Phys. Fluids* **26**, 025111 (2014).
- [189] C. Vanderwel and B. Ganapathisubramani, “Effects of spanwise spacing on large-scale secondary flows in rough-wall turbulent boundary layers”, *J. Fluid Mech.* **774**, R2 (2015).
- [190] J. Yang and W. Anderson, “Numerical Study of Turbulent Channel Flow over Surfaces with Variable Spanwise Heterogeneities: Topographically-driven Secondary Flows Affect Outer-layer Similarity of Turbulent Length Scales”, *Flow Turbul. Combust.* **100**, 1–17 (2017).
- [191] P. Bradshaw, “Turbulent Secondary Flows”, *Annu. Rev. Fluid Mech.* **19**, 53–74 (1987).
- [192] T. Medjnoun, C. Vanderwel, and B. Ganapathisubramani, “Characteristics of turbulent boundary layers over smooth surfaces with spanwise heterogeneities”, *J. Fluid Mech.* **838**, 516–543 (2018).
- [193] R. H. Kraichnan, “Turbulent thermal convection at arbitrary Prandtl number”, *Phys. Fluids* **5**, 1374 (1962).
- [194] S. Grossmann and D. Lohse, “Multiple scaling in the ultimate regime of thermal convection”, *Phys. Fluids* **23**, 045108 (2011).

- [195] G. I. Taylor, “Stability of a Viscous Liquid Contained between Two Rotating Cylinders”, *Proc. Royal Soc. Lond. A* **102**, 541–542 (1923).
- [196] A. Chouippe, E. Climent, D. Legendre, and C. Gabillet, “Numerical simulation of bubble dispersion in turbulent Taylor–Couette flow”, *Phys. Fluids* **26**, 043304 (2014).
- [197] R. Ostilla-Mónico, S. G. Huisman, T. J. G. Jannink, D. P. M. van Gils, R. Verzicco, S. Grossmann, C. Sun, and D. Lohse, “Optimal Taylor–Couette flow: radius ratio dependence”, *J. Fluid Mech.* **747**, 1–29 (2014).
- [198] C. D. Andereck, S. S. Liu, and H. L. Swinney, “Flow regimes in a circular Couette system with independently rotating cylinders”, *J. Fluid Mech.* **164**, 155–183 (1986).
- [199] O. Cadot, Y. Couder, A. Daerr, S. Douady, and A. Tsinober, “Energy injection in closed turbulent flows: Stirring through boundary layers versus inertial stirring”, *Phys. Rev. E* **56**, 427–433 (1997).
- [200] T. H. van den Berg, C. R. Doering, D. Lohse, and D. P. Lathrop, “Smooth and rough boundaries in turbulent Taylor-Couette flow”, *Phys. Rev. E* **68**, 036307 (2003).
- [201] X. Zhu, R. Ostilla-Mónico, R. Verzicco, and D. Lohse, “Direct numerical simulation of Taylor–Couette flow with grooved walls: torque scaling and flow structure”, *J. Fluid Mech.* **794**, 746–774 (2016).
- [202] X. Zhu, R. A. Verschoof, D. Bakhuys, S. G. Huisman, R. Verzicco, C. Sun, and D. Lohse, “Wall roughness induces asymptotic ultimate turbulence”, *Nat. Phys.* **14**, 417–423 (2018).
- [203] P. Berghout, X. Zhu, R. Verzicco, R. J. A. M. Stevens, and D. Lohse, “Direct numerical simulations of taylor–couete turbulence: the effect of sand grain roughness”, Desk drawer ME–247, meander building, University of Twente, the Netherlands (2018).
- [204] J. Nikuradse, “Laws of flow in rough pipes”, *NACA Tech. Mem.* **1292** (1933).
- [205] D. P. M. van Gils, S. G. Huisman, S. Grossmann, C. Sun, and D. Lohse, “Optimal Taylor–Couette turbulence”, *J. Fluid Mech.* **706**, 118–149 (2012).

- [206] E. Fadlun, R. Verzicco, P. Orlandi, and J. Mohd-Yusof, “Combined Immersed-Boundary Finite-Difference Methods for Three-Dimensional Complex Flow Simulations”, *J. Comput. Phys.* **161**, 35–60 (2000).
- [207] G. Iaccarino and R. Verzicco, “Immersed boundary technique for turbulent flow simulations”, *Appl. Mech. Rev.* **56**, 331–347 (2003).
- [208] G. Stringano, G. Pascazio, and R. Verzicco, “Turbulent thermal convection over grooved plates”, *J. Fluid Mech.* **557**, 307–336 (2006).
- [209] S. Grossmann, D. Lohse, and C. Sun, “Velocity profiles in strongly turbulent Taylor–Couette flow”, *Phys. Fluids* **26**, 025114 (2014).
- [210] F. R. Hama, “Boundary-layer characteristics for smooth and rough surfaces.”, *Trans. Soc. Nav. Archit. Mar. Engrs* **62**, 333–358 (1954).
- [211] D. Bakhuis, R. Ostilla-Mónico, E. P. van der Poel, R. Verzicco, and D. Lohse, “Mixed insulating and conducting thermal boundary conditions in Rayleigh–Bénard convection”, *J. Fluid Mech.* **835**, 491–511 (2018).



## Summary

In many geophysical situations and in all industrial applications, turbulent flows are wall-bounded. Many of these flows are multi-phase, *i.e.* flows consisting of one or multiple inclusions. The current understanding of these flows is still limited and this makes it important to study them. In this thesis we study these wall-bounded multi-phase flows in two canonical systems: Taylor-Couette flow and Rayleigh-Bénard convection.

First, we used rigid spherical neutrally-buoyant particles to investigate if we have reduced skin friction similar to bubbly drag reduction. The global torque measurements showed that these particles barely alter the drag, even at very large particle volume fractions. One would expect that adding particles increases the apparent viscosity and therefore, expect an increase in drag. This is however not found and we hypothesize that the drag reducing effect is competing with the drag increase from the increased apparent viscosity.

In real life, actual bubbles can have any shape, and this might be a key element in the drag reducing effect. To test this hypothesis we introduced cylindrical neutrally-buoyant particles into the system. While the drag response of the system was very similar to the spherical particles, we found that these rods show a preferential alignment with respect to the inner cylinder wall. This is very surprising as it was often hypothesized that a systematic alignment in such highly turbulent flows is not possible. We model the orientation of the fibers using the Jeffery equations which give a fair estimate of the shape of the alignment probability density distributions.

Using an immiscible fluid we are able to create deformable inclusions. We selected silicon oil with a viscosity similar to that of water and varied the oil volume fraction between 0 and 100 %. We found two regimes: first we have oil droplets in water, that gradually increase the apparent viscosity until the inversion point. The second regime starts after the inversion where we have water droplets in oil. In this regime we find drag reduction and we think that this is due to much larger water droplets. Using an in-situ microscope we were able to confirm this hypothesis as the water droplets are more than

14× larger than their oil droplet counterparts.

To investigate the effect of non-perfect boundaries, we used another canonical system: Rayleigh Bénard Convection (RBC). Using direct numerical simulations, the boundaries were divided into equal stripes of conducting and insulating regions. While keeping the area identical and varying the amount of divisions we were able to get almost the same heat transfer as a fully conducting system. This means that small temperature imperfections are not visible by the bulk flow.

In the same spirit, we applied sand grain roughness onto the inner cylinder of the Taylor-Couette apparatus, thereby also creating inhomogeneous boundary conditions. By varying the periodicity of the rough/smooth patches, we were able to control the secondary flows. When the width of the roughness patches are similar to the gap size, we find an optimum in angular momentum transport. For the largest patches, we can reduce the secondary flows to only two individual rolls. This shows that different configurations of roughness can alter the flow structure tremendously.

## Summary (Dutch)

In vele geofysische systemen en in bijna alle industriële toepassingen zijn turbulente stromingen begrensd door wanden. Deze stromingen bestaan vaak uit meerdere fasen, dat wil zeggen stromingen met één of meer insluitsels zoals bellen, druppels, of deeltjes. Het huidige begrip over de fysica van dit soort stromingen is nog steeds beperkt en dit maakt het belangrijk om deze te bestuderen. In dit proefschrift worden deze wandbegrensde meerfasenstromingen bestudeerd in twee canonieke systemen: Taylor-Couette-stroming en Rayleigh-Bénard-convectie.

Door het toevoegen van stijve neutrale bolvormige deeltjes aan de stroming, wilden wij onderzoeken of deze een vergelijkbare weerstandsvermindering geven als luchtbellen. Onze globale torsiemetingen toonden aan dat deze deeltjes de weerstand nauwelijks veranderden, zelfs bij gebruik van zeer grote volumefracties. Wij hadden verwacht dat het toevoegen van deze deeltjes de effectieve viscositeit verhoogt, met als gevolg een stijging van de weerstand. Deze toename werd echter niet gevonden. Wij vermoedden dat het weerstandvermindende effect het effect van de verhoogde viscositeit min of meer opheft.

In werkelijkheid kunnen luchtbellen bijna elke vorm aannemen, een eigenschap die mogelijk uiterst belangrijk is voor het weerstandsvermindende effect. Om deze hypothese te testen, hebben we cilindrische neutrale deeltjes geïntroduceerd in ons systeem. Hoewel wij nauwelijks verschil in weerstand zagen tussen de bolvormige en de cilindrische deeltjes, hebben wij ontdekt dat deze deeltjes een voorkeursoriëntatie hebben ten opzichte van de binnencilinder. Dit was zeer onverwacht, omdat vaak wordt verondersteld dat een systematische oriëntatie in uiterst turbulente stromingen onmogelijk is. Door de oriëntatie van de deeltjes te modelleren met behulp van de Jeffery-vergelijkingen kunnen we de distributie van de oriëntatie redelijkerwijs voorspellen.

Door gebruik van niet-mengbare vloeistoffen zijn we in staat om insluitsels te creëren die elke vorm kunnen aannemen. Hiervoor gebruikten wij water en siliconenolie, waarbij de siliconenolie een viscositeit heeft die

vergelijkbaar is met die van het water. We hebben de verhouding tussen deze twee vloeistoffen gevarieerd tussen 0 en 100 %. De gecreëerde emulsies kunnen twee verschillende vormen hebben. Door olie toe te voegen aan water ontstaan oiledrappels in water. De effectieve viscositeit van het mengel wordt hoger dan de viscositeiten van de individuele fasen. Bij overschrijden van een kritische hoeveelheid olie, vindt een inversie plaats en ontstaat een situatie van waterdrappels in olie. Voor deze vorm treedt ook weerstandsvermindering op en we denken dat dit in gang wordt gezet doordat de waterdrappels zeer groot zijn, in vergelijking met de oiledrappels. Door een microscoop op het systeem te bouwen konden we deze hypothese bevestigen en zagen wij dat de waterdrappels 14 keer groter zijn dan de oiledrappels.

Om te onderzoeken wat het effect is van niet-ideale grenscondities maakten wij gebruik van een ander canoniek systeem: Rayleigh-Bénardconvectie. Dit deden we door middel van directe numerieke simulaties, waarbij we de bovenmuur hebben verdeeld in banen van geleidend en isolerend materiaal. De breedte en hoeveelheid van deze banen werden gevarieerd, terwijl de oppervlakte van het isolerende en geleidende gedeelte aan elkaar gelijk bleven. Voor een bovenmuur met de grootste hoeveelheid banen is het warmtetransport bijna identiek aan een systeem met een volledig geleidende bovenmuur. Dit betekent dat kleine imperfecties van de temperatuurgrenscondities niet cruciaal zijn voor de algemene stroming in het systeem.

We kunnen ook niet-ideale grenscondities creëren in het Taylor-Couettesysteem, door de binnencilinder gedeeltelijk ruw te maken met schuurpapier. Door de periodiciteit van ruwe en gladde vlakken te variëren, waren we in staat om de secundaire stromingen te besturen. Bij gebruik van de grootste ruwe vlakken zijn er slechts twee individuele rollen, in tegenstelling tot de optimale breedte waarbij 12 rollen zichtbaar zijn. Het draaimomenttransport heeft een optimum als de breedte van de ruwheid gelijk is aan de afstand tussen beide cilinders. Hiermee hebben wij aangetoond dat een klein verschil in configuratie van de ruwheidselementen de structuur van de stroming enorm kan wijzigen.

## Acknowledgements

In the years I have read many acknowledgements from other theses, however, writing your own acknowledgements for your own thesis is a strange sensation. It makes you realize that a four year period that seemed so long in the beginning is now ending and what an unbelievable journey it has been. The Physics of Fluids group is an unique environment which has the property to cluster and attract amazing people. It always felt as a privilege to be part of this group, from which I have benefited tremendously. I am thankful to the many people I met or worked with over the years, and I will do my best to mention them all.



Dear Chao, I still remember the day that we first met. I was doing my internship together with Julian and Vivek and you entered the water tunnel lab in your black *Nike Air Max* shoes. A few years later, you asked me for this project and I think this was one of the best choices of my life. I was able to learn from one of the best experimentalists and your enthusiastic guidance helped me to get where I am now. What I really appreciated was that you never hesitated to call from Beijing when I was in need of a pep talk. Also the peking duck we had together in Beijing showed your generous hospitality. 您是一个才华横溢的导师，同时也是一个非常好的朋友，非常感谢这一点。



Dear Detlef, I always enjoyed our collaboration over the years. During one of my first conferences, I felt a bit insecure as I did not get some of the talks I attended. You told me that I should not be so harsh on myself and that even you do not always get some talks. Now I know that at APS there is a broad spectrum of quality. During my first pre-APS practice session in you office I remember that only my last slide was untouched. That slide only said: “questions?”. Clearly you must animate Dennis! This is how I, and I guess many others in amPoF, learned to give good talks. Thank you Detlef for all your time, suggestions, ideas, and insights during my PhD.



Beste Sander, ik hoorde van jouw bestaan door een schaterend gelach door de gangen van Meander. Een aantal maanden later zaten we samen hoog volumineus te lachen terwijl jij mij de fijne kneepjes van de Taylor-Couette liet zien. Ons gevoel voor humor ligt duidelijk op één lijn en er zijn alvast

twee eersterangs plaatsen op een specifieke plek gereserveerd. Jouw bijdrage aan mijn onderzoek was onmisbaar en ik heb het gevoel dat sinds jij terug bent in de groep, alles in een stroomversnelling is geraakt. Bijna dagelijks kwam ik bij jou op kantoor met kleine vragen of om gewoon de snoeplade te plunderen. Bedankt voor al je tijd, raad, en snoep door de jaren heen en ik kijk uit naar de komende projecten die wij nog samen gaan doen.

Beste Tom, Bert, Peter, Leo, en René, dit project is in samenwerking met verschillende industriële partners en hiervoor hadden wij jaarlijks een gezamenlijke bijeenkomst. Deze heb ik altijd als zeer prettig en nuttig ervaren.

Joanita, jij bent onmisbaar in de groep en je doet zoveel voor iedereen. Ik vond het altijd fijn om samen met jou de groepsuitjes te organiseren want dan wist ik zeker dat het wel goed zou komen. Als bonus haalden we soms een ijsje bij de ijssalon waar je dochter werkte.

Beste Gert-Wim, Bas, en Martin, jullie kantoor was een toevluchtsoord voor als ik raad nodig had voor de opstelling, software, of bouwprojecten aan mijn eigen huis. Ook gewoon buurten met een bak koffie vond ik altijd fijn en hopelijk kostte dat jullie niet te veel tijd. Hartelijk dank voor al jullie hulp!



Dear Jacco, dear Laura, during my pre-master program I followed the course *physics of fluids*, which was amazingly lectured by Jacco and ta'ed by Laura. This made me actually choose for the fluids track.

Dear Rodolfo, it was always fun to work with you and now, after having multiple students myself, I admire your patience. The numerous “how is the manuscript going” are still haunting me in my sleep. In the end we got the manuscript published and the whole process helped me a lot with all the articles I wrote later. I have good memories of my first and only thanksgiving in Boston. We still need to go diving together!

Dear Roberto, thank you for all your help and advice during the writing of my first manuscript, together with Rodolfo.



Erwin en Matthijs, onze vaste plek was altijd bij de koffieautomaat met discussies over airsoft, crossfit, duiken, en soms zelfs over werk. Ik mis nog regelmatig deze kwartiertjes die ruim 30 minuten kunnen duren.

Beste Ruben, ik heb altijd graag met jou samen gewerkt. Tijdens het sleutelen hadden we altijd uitgebreide maatschappelijke discussies, en wat moesten we toch vaak sleutelen. Ook leerde je mij om soms iets eenvoudiger te denken, hierdoor gingen de projecten later ook een stuk vlotter. Weet jij trouwens waar de imbus-acht is gebleven?

Dear Rodrigo, first I would like to apologize for all the Mexican stereotypical jokes. Next, I want to thank you for all your effort as the lab has never been so clean in years. Jokes aside, it was always a great pleasure to work with you. You are always very careful and precise, which is a valuable addition to my sometimes blunt approaches. We shared the night shift during our MSc., later the night shift at the end of our PhD, and finally we will also share the night shift of our graduation.



Beste Pim, wij hebben heel wat lagen op de TC geplakt en weer verwijderd. Tijdens meerdere bijeenkomsten hebben wij gediscussieerd over onze uitkomsten, tenminste als je niet naar de kapper moest. Bedankt voor alle hulp en waarschijnlijk werken we nog even samen.



To the students in ME101: Valentin, Charles, Michah, Arne, Sander, Raymond, and Dominic, I had big fun working with you guys on the various projects. We have achieved great things, including two publications.



Alvaro (der große), vielen Dank für deine Hilfe. Dein Beitrag zum Ölproject war unverzichtbar. Auch dein unerschöpfliches Interesse an der Wissenschaft hat mich immer inspiriert. Wir sehen uns bestimmt noch bei der Crossfitbox.



Varghese, thanks for all your help with the manuscripts. I really like your style of writing and I was always amazed how easily you can write. Sometimes I joined your discussions with Shantanu on how things work in India, which I really enjoyed.



亲爱的晓珏，感谢你这些年来对我的帮助。抱歉曾经叫你“胖子”，因为这是我所知道的为数不多的汉语之一。



Dominik, with an office exactly between me and the coffee machine, it was a regular visit. I really liked our scientific discussions and these brought up many new ideas.



Dear Vamsi, my Pythonista brother, together we preached the path of enlightenment and many souls we converted. You taught me about the core of Indian cuisine and together with Biljana showed me how to make delicious dishes. Partying with locals in Stockholm, or in Lederhosen with “ein Maß” in Gronau. Together with you it was always fun!

Dear Biljana, almost the full four years we were colleagues. In my first year we went to Udine for the Bubbly flows course (of course mainly for the ice cream) and the cool trip to Croatia afterwards. On parties, I remember the plastic bottles filled with strong Serbian liquor, of course homemade. But the best things are always the simple things: our daily fist bumps! 🤝



Liebe Carola, ich wollte dich nie dazu zwingen, bei der Organisation des Gruppenausflugs mitzuhelfen. Es war wirklich Detlefs Idee, aber auf jeden Fall eine gute Idee. Ich freue mich auf jeden fall auf den 7. Februar 2019.



Dear Mazi, you are a great guy and one of the few non-Dutchies that likes electronic music. I always enjoyed the laughters in our office. You still owe me a joke though.

Dear Elise, I never thought that I would miss your complaining in the office. The weather, the food, actually all non-French gets a slap from you. Rodrigo tried to take over, but it is just not the same. The baguette hanging on the wall of our office is like a shrine to remember the good old times.

你好安儒, you learned me some basic Cantonese and technically all my swearing in Mandarin so you can be proud! Thanks for your help.

Dear Enrique, you are a master chef and the star of the Mexican cooking night. You were always great company!

Ivan, while your midi-chlorian count is just 2500 per cell, I always found you to be strong with the force. I am glad that it is settled for life: I was faster than you at the bata. Thanks for the many laughs!

Dear Maxime, armed with *bretelles* and *papillon* you marched through Meander. You are as French as it gets! There is still a bottle of Klevener with your name on it in our wine rack.

Pieter, samenwerken met iemand uit Roffa is altijd dolle pret. Lekkere platte humor en flauwe grappen. Thanks!

Martin, wij hebben veel samengewerkt tijdens de master. Van jou heb ik veel perfectionele trekjes aangeleerd, want jij was alleen tevreden met het beste. Ons meesterwerk was dan ook de “Physical Review Litter” voor Experimental techniques. Jij gaat het ook halen, daar ben ik van overtuigd! Tot straks bij de wod?

Guillaume en Fenna, bij jullie zijn het altijd gezellige etentjes met een bijzondere wijn uit de klimaatkast. Het goede leven kunnen we zeker bij jullie vinden! En Guillaume, dat ik laatst een “good” kreeg van jou is helemaal bijzonder. Ik dacht namelijk dat “not bad” het hoogst haalbare was bij Fransen.

Michiel, jij bent voor mij nog steeds een echte bierbrouwmeester. Door pastasaus met bier te combineren, hoef je alleen nog maar spaghetti te koken. Geniaal!

Mathijs, Evelyn, Jeroen, Thomas W., Thomas A., Vincent, Philip, en Jan-Willem, samen hebben we een start gemaakt met technische natuurkunde op het Saxion. Ik vond dit een toffe tijd, erg leerzaam maar

ook veel lol. Daarom is het ook extra leuk dat we elkaar af en toe nog spreken. Bedenkt vor elles! (das engels voor bedankt voor alles)!

Fellow adventurers Molag Ba'al, Alan Longfingers and Aurora Eather, often have we fought together, slaying hounds and demons, and saving the day. Mylana Quickblade salutes you!

Squatting, push-ups, and wall balls, nothing can stop pof'ers during the *wod*. Thanks Alvaro, Alvaro, Martin, and Mikhail for the many cheers. José, too bad you exchanged barbells for boats.

Some pof'ers could be convinced to run through mud. Adeline, Rémi , and Kim joined before it was cool. The year after Maaike, Kim, Pieter, Pim, Pallav, Angi, Alvaro, Dennis v.G., Martin, Sander, Ricardo, Myrthe, Guillaume, and Jessica joined and we were unstoppable!

延深, 鵬宇, 延涛, 亚星感谢在 PoF 与你们一起度过的无数美好时光。

The PoF group has many amazing people who I shared many memories with. I'd like to thank Devaraj, Michel, Andrea, Leen, Richard, Alexander B., Alexander K., Anaïs, Anja, Anupam, Arjan, Claas-Willem, Diana, Huanshu, Lijun, Liz, Loreto, Marie-Jean, Marise, Martin, Mathijs, Michiel, Nakul, Pascal, Riëlle, Rianne, Roeland, Sander, Srinath, Srinidi, Steven, Utkarsh, Vatsal, Yogesh, and the many people I forgot to mention here.

Evelien, Rob, Patrick, Clair, Daan, Matthijs, en Sebastiaan, bedankt voor de nodige ontspanning de afgelopen jaren met duiken, barbeques, duikweekenden, en grotduikcursussen.

Beste Roy en Michelle, bedankt voor de leuke dineetjes samen. Daar gaan er vast nog vele van volgen!

Beste Richard en Ellen, wat heb ik gelachen in de afgelopen jaren met jullie. Ja echt! Het kan soms niet gek genoeg. Proost!

Beste Jeroen en Eline, we kennen elkaar van de crossfit maar ontdekten snel dat we allemaal ook wel een borrel lusten. Het liefst kopen we in beschonken toestand dozen Oosterijkse wijn. Tot de volgende borrel!

Beste Erik en Saskia, met jullie op pad is altijd gegarandeerd avontuur en gezelligheid. In de bossen op zoek naar een gat in de grond of bepakt met meerdere cilinders en droogpak. Ik kijk uit naar de nieuwe avonturen.

Beste René en Mariëlle, vroeger was het altijd samen feesten, maar ja, ik ben ook geen 26 meer hè. Dank je wel voor de gezelligheid de afgelopen jaren!

Beste Rachel, Robin, Arnoud, Elise, Sabrine en Wouter, samen hebben wij gekookt, gedanst op de mainstage (uiteraard links vooraan), en meer dan eens te diep in het glasje gekeken. Bedankt voor alle gezelligheid en katers!

Beste Gijsbert en Anneke, het is geen onbekend fenomeen dat de Knakkies bier zitten te brouwen in jullie tuin. Al snel komen bier, wijn, en hapjes op tafel. Bedankt voor alle lekkernijen!

Beste Floris, Petra, en Suze, ik vind het altijd fijn om bij jullie op bezoek te zijn. Vrienden door dik en dun en waar ik altijd van op aan kan. Het is gezellig om dingen met jullie te ondernemen of om gewoon een bak koffie te halen. Bedankt voor alle steun en hulp!

Lieve tante Ingrid en ome Gerard, jullie hebben altijd met mij meegeleefd de afgelopen jaren. We hebben altijd lekker bij jullie gegeten en altijd interessante en leerzame discussies over politiek en geschiedenis, uiteraard met een goed glas wijn. Bedankt voor jullie gezelligheid.

Lieve oma Hanny, aan het begin van mijn studerend leven, kwam ik regelmatig bij jou eten. Nu hebben wij dit omgedraaid en kom je gezellig bij je kleinzoon eten. Het is altijd leuk om je verhalen te horen en ik waardeer deze avonden enorm.

Lieve Dick en Leni, ik voel mij altijd thuis bij jullie. Gezellig een pilsje tijdens een barbecue in de tuin, of een lekker bord van de befaamde bonensoep. Graag denk ik ook even mee met de puzzels. Bedankt voor jullie warme gastvrijheid.

Lieve Tom, ik vind het fijn dat het goed met jou gaat en dat je weer actief deel uitmaakt van ons leven. Het is een stuk gezelliger met jou erbij. Hopelijk kunnen we nog veel meer dingen samen vieren!

 Lieber Andreas, Nina, Mika, Stina, Hans-Wilhelm und Erika, vielen Dank für die gemütlichkeit der letzten Jahre. Gemeinsam genießen von Nudelsalat, Kartoffelsalt, und Würstchen und danach jede menge Playmobil aufbauen. Danke für die schöne Zeit zusammen.

 Lieve Mamma en Pappa, ik heb het erg getroffen met jullie als ouders. Altijd bereid om mij helpen, ongeacht wat ik weer eens heb bedacht. Bedankt voor jullie onvoorwaardelijke steun en liefde. Ik hou van jullie.

Liefste Kim, jij hebt mij al deze jaren bijgestaan, ongeacht de keuzes die ik heb gemaakt. Zat ik er even doorheen kan ik altijd bij jou terecht voor een glimlach, knuffel, of een zoen. Ik denk dat dit zonder jou nooit was gelukt. Dit avontuur is ten einde maar ik kijk al uit naar ons volgende avontuur, wat het ook mag zijn. Ik heb je lief, mijn lieve Kim!

# Scientific output

## Publications

- *Mixed insulating and conducting thermal boundary conditions in Rayleigh–Bénard convection*  
**Dennis Bakhuis**, Rodolfo Ostilla-Mónico, Erwin P. van der Poel, Roberto Verzicco, and Detlef Lohse  
J. Fluid Mech. **835**, 491–511 (2018)
- *Finite-sized rigid spheres in turbulent Taylor–Couette flow: effect on the overall drag*  
**Dennis Bakhuis**, Ruben A. Verschoof, Varghese Mathai, Sander G. Huisman, Detlef Lohse, and Chao Sun  
J. Fluid Mech. **850**, 246–261 (2018)
- *Statistics of rigid fibers in strongly sheared turbulence*  
**Dennis Bakhuis**, Varghese Mathai, Ruben A. Verschoof, Rodrigo Ezeta, Sander G. Huisman, Detlef Lohse, and Chao Sun  
Under review
- *Controlling the secondary flow in turbulent Taylor–Couette turbulence through spanwise-varying roughness*  
**Dennis Bakhuis**, Rodrigo Ezeta, Pieter Berghout, Pim A. Bullee, Dominic Tai, Daniel Chung, Roberto Verzicco, Detlef Lohse, Sander G. Huisman, and Chao Sun  
Under review
- *Catastrophic Phase Inversion in Turbulent Taylor–Couette flow*  
**Dennis Bakhuis**, Rodrigo Ezeta, Pim A. Bullee, Alvaro Marin, Detlef Lohse, Sander G. Huisman, and Chao Sun  
In preparation

- *Wall roughness induces asymptotic ultimate turbulence*  
Xiaojue Zhu, Ruben A. Verschoof, **Dennis Bakhuis**, Sander G. Huisman, Roberto Verzicco, Chao Sun, and Detlef Lohse  
*Nature Phys.* **14**, 417–423 (2018)
- *Air cavities at the inner cylinder of turbulent Taylor–Couette flow*  
Ruben A. Verschoof, **Dennis Bakhuis**, Pim A. Bullee, Sander G. Huisman, Chao Sun, and Detlef Lohse  
*Int. J. Multiphase Flow* **105**, 264–273 (2018)
- *The influence of wall roughness on bubble drag reduction in Taylor–Couette turbulence*  
Ruben A. Verschoof, **Dennis Bakhuis**, Pim A. Bullee, Sander G. Huisman, Chao Sun, and Detlef Lohse  
*J. Fluid Mech.* **851**, 436–446 (2018)
- *Rough-wall turbulent Taylor–Couette flow: The effect of the rib height*  
Ruben A. Verschoof, Xiaojue Zhu, **Dennis Bakhuis**, Sander G. Huisman, Roberto Verzicco, Chao Sun, and Detlef Lohse  
*Eur. Phys. J. E* (2018) **41**: 125
- *Drag reduction in boiling Taylor–Couette turbulence*  
Rodrigo Ezeta, Sander G. Huisman, **Dennis Bakhuis**, Chao Sun, and Detlef Lohse  
Under review
- *Local maxima for angular momentum transport in small gap  $\eta = 0.909$  ultimate Taylor–Couette turbulence*  
Rodrigo Ezeta, **Dennis Bakhuis**, Francesco Sacco, Sander G. Huisman, Rodolfo Ostilla-Mónico, Roberto Verzicco, Chao Sun, and Detlef Lohse  
Under review
- *Ultimate Taylor–Couette turbulence using a superhydrophobic inner cylinder*  
Pim A. Bullee, Ruben A. Verschoof, **Dennis Bakhuis**, Sander G. Huisman, Chao Sun, Rob G. H. Lammertink and Detlef Lohse  
In preparation
- *Bubbly drag reduction with sandgrain roughness boundaries*  
Pim A. Bullee, **Dennis Bakhuis**, Rodrigo Ezeta, Sander G. Huisman, Chao Sun, Rob G. H. Lammertink and Detlef Lohse  
In preparation

## Organizing activities

- Organized the 8<sup>th</sup> International Conference on Rayleigh-Bénard turbulence (2018)  
*University of Twente, the Netherlands* (100+ attendees)
- Organized the Physics of Fluids group 4 days workshop (2018)  
*Eifel, Germany* (60+ attendees)

## Outreach

- Peer-review: Refereeing multiple times for the International Journal of Multiphase flow
- Outreach: Numerous lab demonstrations for a wide variety of audiences.
- Outreach: Numerous lab demonstrations for a wide variety of audiences.

## Teaching activities

- Teaching assistant for the graduate course “Experimental techniques in physics of fluids” in years 2016, 2017, and 2018.
- Lectured a crash course in scientific Python programming to graduate- and PhD students in years 2016, 2017, and 2018.
- Bachelor student supervision: Raymond Kip.
- Intern student supervision: Dominic Tai, Michah Holband.
- Master student supervision: Valentin Badin, and Charles Cail.

## Attended workshops

- *Dynamics of bubbly flows*  
International centre of mechanical sciences, Udine, Italy (2015)
- *Particle image velocimetry*  
LaVision, Göttingen, Germany (2015)

- *Turbulence*  
J. M. Burgerscentrum, Delft, the Netherlands (2016)
- *School on turbulence*  
Invited talk: “Twente Turbulence Facilities”  
EUhit, Warsaw, Poland (2016)

## Peer review conference talks / posters

- *Spatial distribution of finite-sized particles in turbulent Taylor–Couette flow* (poster)  
19<sup>th</sup> International Couette–Taylor workshop (ICTW), 2015  
Cottbus, Germany
- *Spherical and anisotropic particles in turbulent Taylor–Couette flow* (talk)  
16<sup>th</sup> European Turbulence Conference (ETC), 2017  
Stockholm, Sweden
- *Mayonnaise Taylor–Couette Turbulence* (talk)  
20<sup>th</sup> International Couette–Taylor workshop (ICTW), 2018  
Marseille, France
- *Catastrophic Phase Inversion in Turbulent Taylor–Couette Flow* (talk)  
Physics@veldhoven, 2019  
Veldhoven, the Netherlands

## Contributed conference talks

- *Mixed insulating and conducting boundary conditions in Rayleigh–Bénard convection*  
68<sup>th</sup> Annual Meeting of the APS Division of Fluid Dynamics, 2015  
Boston, Massachusetts, United States of America
- *Rigid spherical particles in highly turbulent Taylor–Couette flow*  
69<sup>th</sup> Annual Meeting of the APS Division of Fluid Dynamics, 2016  
Portland, Oregon, United States of America

- *Anisotropic particles in highly turbulent Taylor–Couette flow*  
70<sup>th</sup> Annual Meeting of the APS Division of Fluid Dynamics, 2017  
Denver, Colorado, United States of America
- *Statistics of anisotropic particles in intensely sheared turbulence*  
Burgers symposium, 2018  
Lunteren, the Netherlands
- *Catastrophic phase inversion in mayonnaise Taylor-Couette turbulence*  
71<sup>th</sup> Annual Meeting of the APS Division of Fluid Dynamics, 2018  
Atlanta, Georgia, United States of America

